REPUBLIC OF TURKEY
ADANA ALPARSLAN TÜRKEŞ SCIENCE AND TECHNOLOGY UNIVERSITY

GRADUATE SCHOOL OF NATURAL AND APPLIED SCIENCES
DEPARTMENT OF AEROSPACE ENGINEERING

THE EFFECT OF THE RIBLETS ON FLOW CONTROL OF NACA0018 AT LOW REYNOLDS NUMBER

EMRE GÜLER

MASTER OF SCIENCE

ADANA 2021

REPUBLIC OF TURKEY

ADANA ALPARSLAN TÜRKEŞ SCIENCE AND TECHNOLOGY UNIVERSITY

GRADUATE SCHOOL OF NATURAL AND APPLIED SCIENCES

DEPARTMENT OF AEROSPACE ENGINEERING

THE EFFECT OF THE RIBLETS ON FLOW CONTROL OF NACA0018 AT LOW REYNOLDS NUMBER

EMRE GÜLER

MASTER OF SCIENCE

SUPERVISOR

ASSOC. PROF. DR. TAHİR DURHASAN

ADANA 2021

I hereby declare that all information in this thesis has been obtained and presented in accordance with academic rules and ethical conduct. I also declare that, as required by these rules and conduct, I have fully cited and referenced all information that is not original to this work.

[Signature]

Emre GÜLER

ABSTRACT

THE EFFECT OF THE RIBLETS ON FLOW CONTROL OF NACA0018 AT LOW REYNOLDS NUMBER

Emre GÜLER

Department of Aerospace Engineering

Supervisor: Assoc. Prof. Dr. Tahir DURHASAN

December 2021, 97 pages

In recent years, numerical and experimental aerodynamic studies have been focused on low Reynolds number flows in order to control turbulence transition and laminar separation bubble of unmanned aerial vehicles and wind turbines. In this thesis, numerical analysis was performed to control of flow over NACA 0018 airfoil using riblet surface at Reynolds number of $Re=1x10^5$ in order to increase aerodynamics coefficients such as lift and lift to drag ratio. The riblets were located on the suction surface of airfoil. The main parameters were selected as the height of riblet, location, gap ratio between riblets, the size of riblet region and angle of attack. The numerical analyzes were carried out using $k\text{-}k_L\text{-}\omega$ transition model. The obtained results indicate that the height of riblet remarkably affects the formation of laminar separation bubble and increase the lift coefficient in comparison with clean airfoil.

Keywords: Aerodynamics, passive control method, CFD, low Reynolds number, laminar separation bubble

ÖZET

RİBLETLERİN DÜŞÜK REYNOLDS SAYISINDA NACA 0018'İN AKIŞ KONTROLÜ ÜZERİNE ETKİSİ

Emre GÜLER

Havacılık ve Uzay Mühendisliği Anabilim Dalı

Danışman: Doç.Dr. Tahir DURHASAN

Aralık 2021, 97 sayfa

Son yıllarda, insansız hava araçlarında ve rüzgar türbinlerinde, türbülansa geçişi ve laminer ayrılma kabarcığını kontrol etmek için düşük Reynolds sayılı akışlarda sayısal ve deneysel aerodinamik çalışmalar yoğunlaşmıştır. Bu tez çalışmasında, kaldırma ve kaldırma/sürükleme oranı gibi aerodinamik katsayıları artırmak için Re=1x10^5 Reynolds sayısında riblet yüzeyi kullanılarak NACA 0018 kanat profili üzerindeki akışın kontrolü için sayısal analiz yapılmıştır. Ribletler kanat profilinin emme yüzeyine yerleştirilmiştir. Riblet yüksekliği, lokasyon, ribletler arası boşluk oranı, riblet bölgesinin büyüklüğü, riblet şekli ve hücum açısı temel parametreler olarak seçilmiştir. Nümerik analizler k-kl-w geçiş modeli kullanılarak yürütülmüştür. Elde edilen sonuçlar riblet yüksekliğinin laminar ayrılma kabarcığı oluşumunu önemli ölçüde etkilediğini ve temel kanat profiline kıyasla kaldırma katsayısını artırdığını göstermektedir.

Anahtar Kelimeler: Aerodinamik, pasif kontrol metodu, HAD, düşük Reynolds sayılı akış, laminer ayrılma kabarcığı

Dedicated to All Researchers…

ACKNOWLEDGEMENTS

I would like to thank my dear supervisor Assoc. Prof. Dr. Tahir DURHASAN, who contributed from the planning of this thesis to its conclusion, who was a perfect guide to me with numerous help and advice, and Assoc. Prof. Dr. İlyas KARASU, who was with me at every moment and shared his experience and knowledge all the time, who believed in me and helped me get this far. I also thank to Asst. Prof. Dr. Hürrem AKBIYIK for his knowledge and helps on experimental processes and for answering my all question. No matter how much I thank them, it will not be enough.

I would like to thank the Rector of Tarsus University Prof. Dr. Orhan AYDIN, Dean of Faculty of Aeronautics and Astronautics Prof. Dr. Kasım OCAKOĞLU and Head of Aerospace Engineering Assoc. Prof. Dr. Muharrem KUNDURACI for their support on academic life and to all member of Tarsus University family.

I would like to thank General Manager of ARES PHE Arben YABALI for his motivation and providing financial support on experimental equipment of this research. Thanks to all member of ARES PHE Company family.

I would like to thank my colleague Re. Asst. Mehmet ERDEM and Re.Asst. Burak DEMİRTAŞ for their support during this difficult journey. I am so glad to my college friend Re. Asst. Selahattin KARAÇAY and Tugay ÇELİK for powering me. And my friends, Cengiz Ziya HAMEŞ, Berk ÇELİKSU, Mustafa Oruç ATALAY, İsmail DUYMUŞ and Perihan Kübra DEMİRCİOĞLU, who were with me at this strenuous experience. I am grateful to all my friends for always supporting me.

Finally, I would like to thank my dear family, who never condemned me to despair and brought me out of the darkest night into the brightest morning, my dear father Hüseyin GÜLER, my dear mother Zühre GÜLER, my sisters Ebru GÜLER and Funda DURHASAN, my brother Yasin DURHASAN and my dear nephew Poyraz DURHASAN.

TABLE OF CONTENTS

LIST OF FIGURES

LIST OF TABLES

NOMENCLATURE

Re	: Reynolds number
α	: Angle of Attack
δ	: Boundary Layer Thickness
C_L	: Lift Coefficient
C_D	: Drag Coefficient
C_L/C_D	: Lift-to-Drag Ratio
C_P	: Pressure Coefficient
C_M	: Moment Coefficient
c	: Chord Length
P	: Pressure
ρ	: Density
V_∞	: Free-Stream Velocity
C_{Lmax}	: Maximum Lift Coefficient
ω	: Specific Dissipation Rate
k_T	: Turbulent Kinetic Energy
k_L	: Laminar Kinetic Energy
μ	: Molecular Viscosity
θ	: Momentum Thickness
Tu	: Turbulence Intensity
y^+	: Dimensionless Wall Length
h	: Riblet Height
s	: Riblet Spacing
w	: Riblet Width

1. INTRODUCTION

After the World War I, the studies on flow over airfoil gained great importance have being continued attraction since airfoils have been used commonly in design of unmanned aerial vehicles (UAV) and micro aerial vehicles (MAV). In the studies on the flow over airfoil may be classified depends on the Reynolds number. If Reynolds number is less than 500 000, flow condition is called as low Reynolds number flow. Low Reynolds number flow condition is encouraged in many engineering applications (such as wind turbine blades, unmanned aerial vehicles (UAV) and micro aerial vehicles (MAV)) and nature (such as birds and insect). These smale-scale bodies are susceptible to laminar boundary layer separation. The main flow characteristics of low Reynolds number flow is formation of laminar separation bubble, which occurs between separation point and reattachment point due to viscous effects or strong adverse pressure gradients.
The laminar separation bubble can be adversely affect on aerodynamic of airfoil such as decrease in lift, increase in drag, mechanical vibration, acoustic noise and also it maybe causes stall. To avoid these effects, flow control around airfoil is main issue for engineer and researcher.

1.1. Flow Around an Airfoil

Many studies have been carried out on the flow over airfoil to reveal the flow characteristic of airfoil. Understanding the flow mechanism over an airfoil is an important subject to decide airfoil profile on design stages. The airfoil profiles depend on the flight regime can be categorized into three groups; general purpose, high lift and high speed airfoils. In addition, they can be classified depend on geometry which are symmetrical and asymmetrical.

The optimization of the airfoil is necessary because the flow over the airfoil behaves differently in different flight regimes such as subsonic, sonic, and supersonic, as shown in Figure 1.1. Airfoil design has increased as technology has enabled higher speeds, and refinements have been made to airfoils for various flight regimes. Even though it is excellent for an airfoil to be completely streamlined and generate lower drag, it may not be able to generate the necessary lift force for an airfoil. Therefore, airfoil preferences are made for different flow regimes depending on the application area. A high lift airfoil is used in a sailboat to provide a higher lift force, while the use of a supersonic airfoil in a fighter aircraft in the supersonic flight regime to achieve high speeds prevents the formation of a detached shock in front of the airfoil due to the high airspeed.

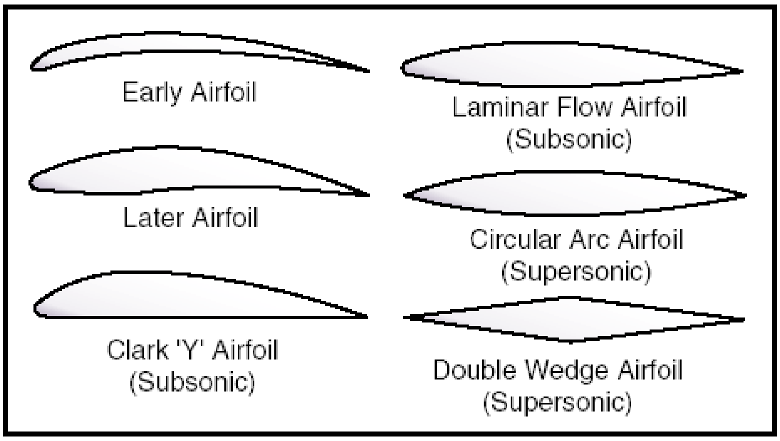

Figure 1.1. Airfoil Shapes for Different Flow Type (Airplane Aerodynamics, 2021)

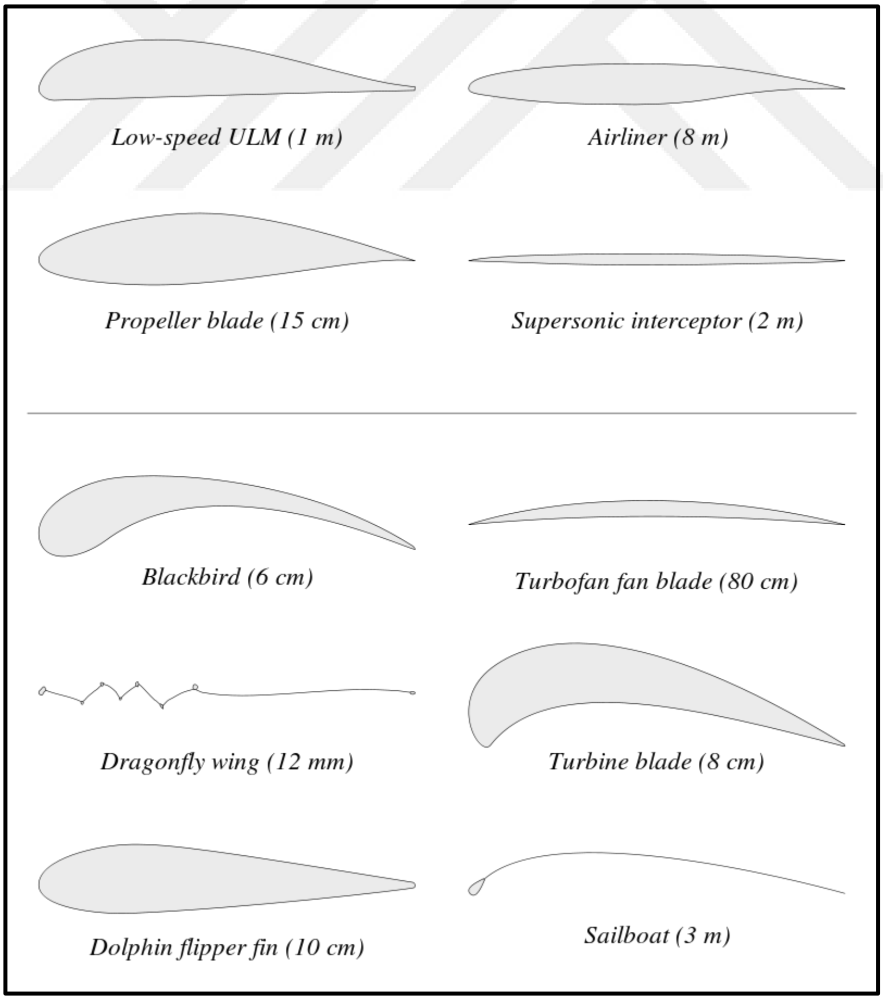

Figure 1.2. Various Type of Airfoils (Wikipedia, 2021)

Low Reynolds number flow is significantly different from high Reynolds number flow. In low Reynolds number flow, viscous forces are more dominant than inertial forces. Therefore, the upper surface of the airfoil is more susceptible to separation. On the other hand, at higher Reynolds numbers, the momentum of flow increases, therefore, the separation of flow is delayed.

Figure 1.2 shows the different types of airfoil encountered in nature and in engineering applications. These airfoils have different geometry depending on the application area and flow conditions such as leading edge radius, maximum camber, maximum thickness, and chord length of airfoil.

As aforementioned in above, airfoils can be categorized into two groups depend on the geometry which are symmetrical and asymmetrical. Symmetrical airfoils have same geometry on the upper and bottom surface while asymmetrical airfoils have different geometry on upper and bottom surface. Upper and bottom surfaces of airfoil are also named as suction and pressure surface, respectively. Figure 1.3 depicts formation of lift force on airfoil surface. Since upper and lower streamlines travel different distance on the airfoil surface, they both reach the exit point at the same time to ensure the conservation of mass, so velocity difference occurs. This velocity difference causes pressure difference between upper and lower surfaces by Bernoulli principle. Therefore, this pressure difference creates lift force.

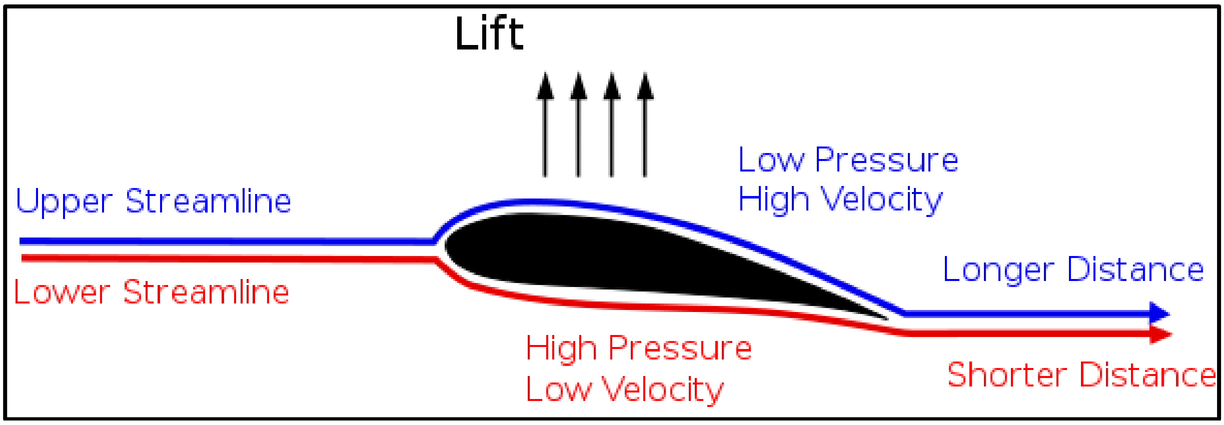

Figure 1.3. Explanation of Lift Force (Lift Theory, 2021)

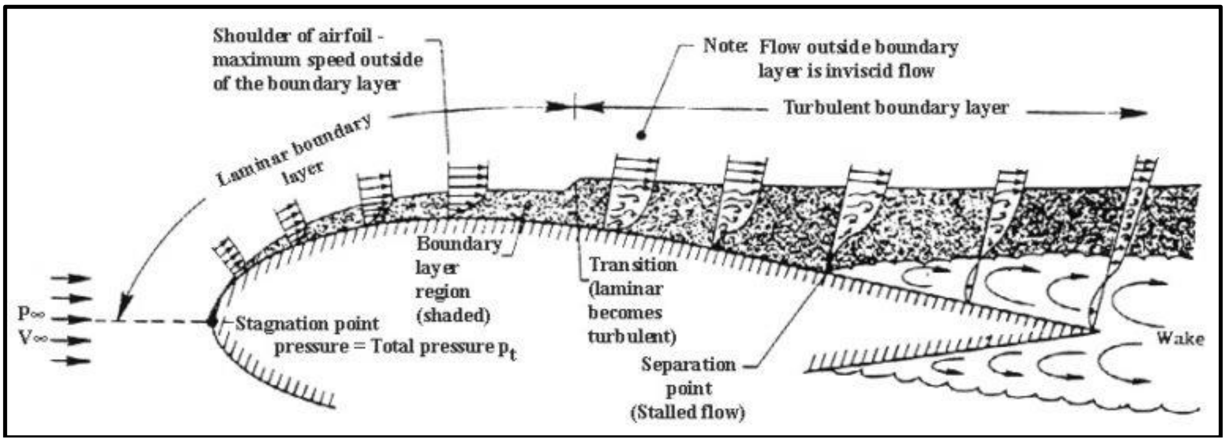

Figure 1.4. Boundary Layer Formation over Airfoil (U.S. Centennial, 2021)

The boundary layer is the region where the outcomes of viscous shear stress caused by the viscosity of the fluid. The boundary layer is composed of three regions in accordance with local Reynolds number as seen from Figure 1.4; laminar boundary layer, laminar-to-turbulent transition region and turbulent boundary layer. In the laminar boundary layer, flow is a thin layer, which is stable and the flow is regular. The flow gradually becomes unstable with increase in the Reynolds number, and this instability forces the flow regime to transition from laminar to turbulent regime. This region is called transition region. It is possible to classify the transition to turbulence as natural transition, bypass transition and separated flow transition. The natural transition given in Figure 1.5.a occurs because of the boundary layer. This type of transition is seen in flows where the free flow turbulence is low. The flow on the flat plate continues laminarly over a certain distance. With the Reynolds number reaching the critical level, TS waves are formed in the flow. With the destabilization of the flow, longitudinal 3D vortices form behind the TS waves. The eddies that disperse in the downstream direction form turbulent droplets. Fully turbulent flow occurs when these droplets coalesce. The natural transition is seen in flows with high Reynolds number. In Figure 1.5.b, the bypass transition is shown. In this transition type, since the flow has high turbulence, it immediately changes to turbulent droplets and then to fully turbulent flow. The separated-flow transition seen mostly in low Reynolds number flows is showed in Figure 1.5.c. With the reverse pressure gradients caused by viscous effects separates the flow from the surface, the flow turns into turbulent flow due to the eddies formed in the flow.-.In the turbulent boundary layer, flow is highly irregular and unstable, and eddy vortices are formed . Boundary layer thickness as a function of Re number, δ can be defined as the free-flow velocity of the velocity u parallel to the plate divided by the geometric location of the points where U velocity reaches 99%.

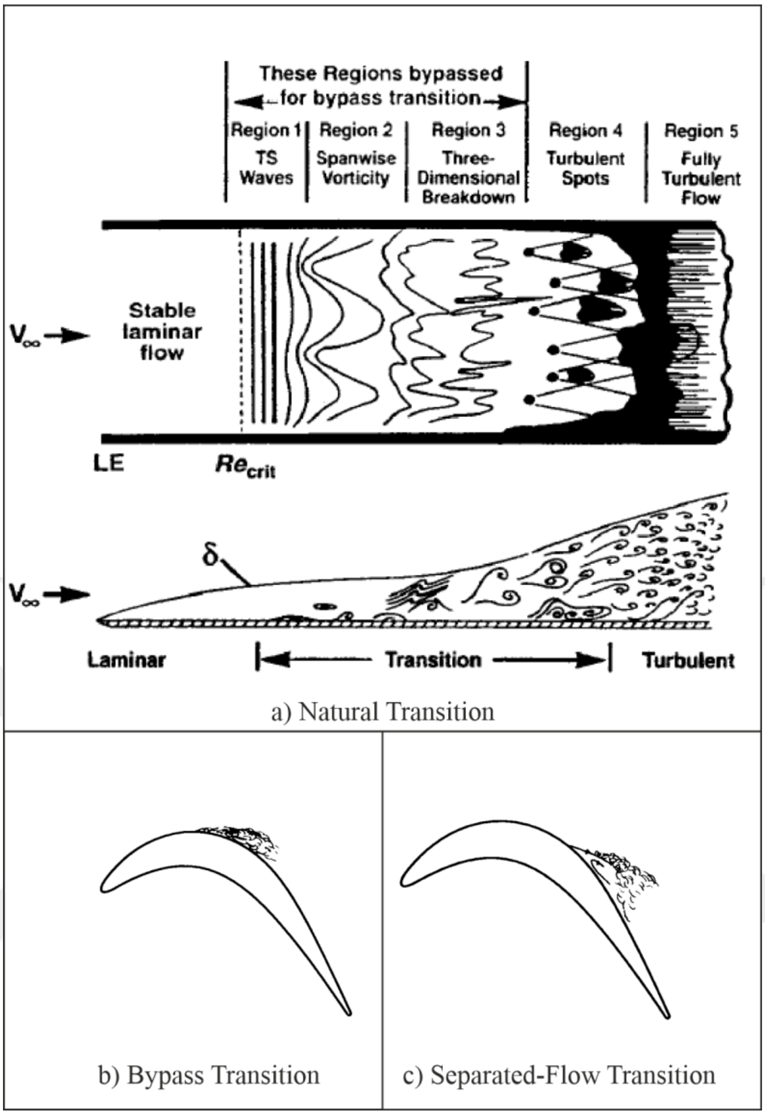

Figure 1.5. Types of Transition

1.2. Low Reynolds Number Flow

External flows with a Reynolds number between Re=5x10^4 and 5x10^5 are called low Reynolds number flows. While today's classic high-speed passenger planes travel at Re=10^7~10^9, smaller aerial vehicles travel at Re=10^5~10^6. If flow regimes classified aerodynamically, in the range of Reynolds number from Re=50 000 to Re=1 000 000 is called low Reynolds number aerodynamics. There are many examples of low and very low Reynolds number flows below in engineering application and nature. Some of these are depicted in the Figure 1.6 by comparing mass versus Reynolds number, such as; micro aerial vehicles, unmanned aerial vehicles, birds and insects.

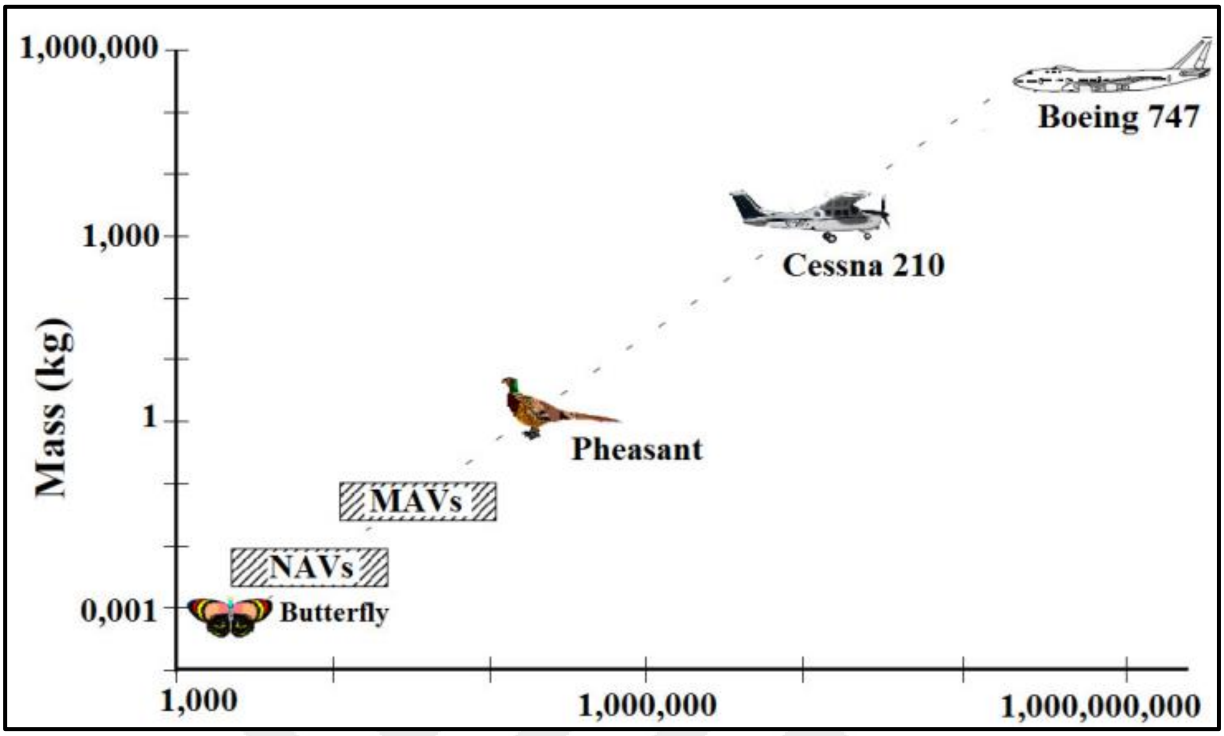

Figure 1.6. Classification of Flying Objects over a Relation of Mass and Reynolds Number (Barata et al., 2015)

The main difference between flying objects arise from the reduction of the wing chord length. The detailed studies are presented on the change of laminar separations and laminar to turbulence transition points, which occur at low speed, unlike the flow structure of today's passengers aircrafts. Due to the change of laminar separation and transition points, the aerodynamic structure changes, so aerodynamic performance may be adversely affected. When the Reynolds number is low, the viscous forces are more dominant than inertial forces. Compared to the higher Reynolds number flows, the flow separation occurs early.

Figure 1.7 depicts the flow structures for two different low Reynolds number flows. In the Figure 1.7.a, the separated shear layer cannot attach to the airfoil surface and laminar separation occurs. In higher Reynolds numbers (Fig.1.7.b), the flow can reattach to the surface due to the turbulent separated shear layer and the area in between separation and reattachment points creates the laminar separation bubble (Yarusevych et al., 2009).

The low Reynolds number may be due to the small chord length or the low flow velocity or both. In addition, on unmanned aerial vehicles flying at high altitude, the Reynolds number decreases due to low air density and high kinematic viscosity, and the physics of low Reynolds number flows emerge. Since the pioneering research into airfoil operates at low Reynolds numbers, summarized and expanded by Tani (1964) and Gaster (1967), many relevant studies have been conducted over the past few decades.

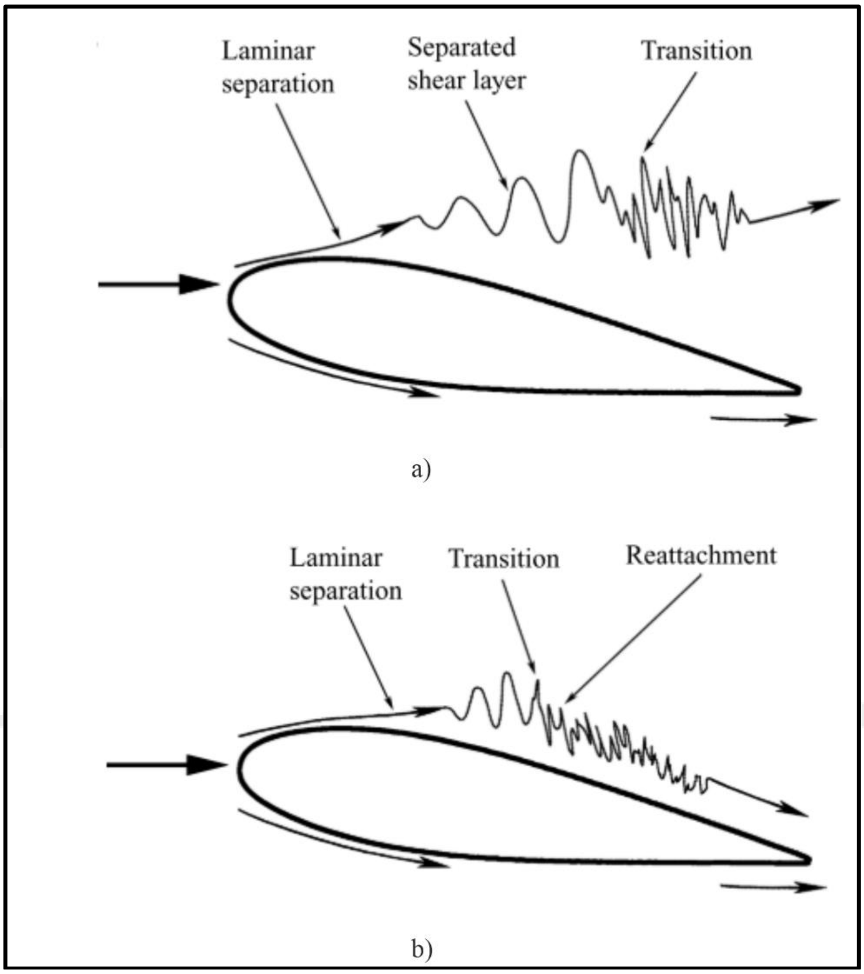

Figure 1.7. Flow over Airfoil at Low Reynolds Number with and without Reattachment

1.3. Laminar Separation Bubble

When the laminar and turbulent boundary layer regions are examined in detail at low Reynolds numbers, it is seen that many flow phenomena are interconnected. As shown in Figure 1.8, the flow that follows the surface regularly until the point of laminar flow cannot hold onto the surface, separates due to velocity gradient, and changes from laminar flow to turbulent flow regime. After flow structure changed from laminar to turbulent flow, flow re-attaches to the surface and laminar separation bubble occurs. There are backflow and reverse velocity profiles in the inner region of the bubble. The humped structure formed in the graph of the pressure coefficient gives information about the formation, location and width of the laminar separation bubble. There is reverse velocity profiles in the inner region of the bubble.

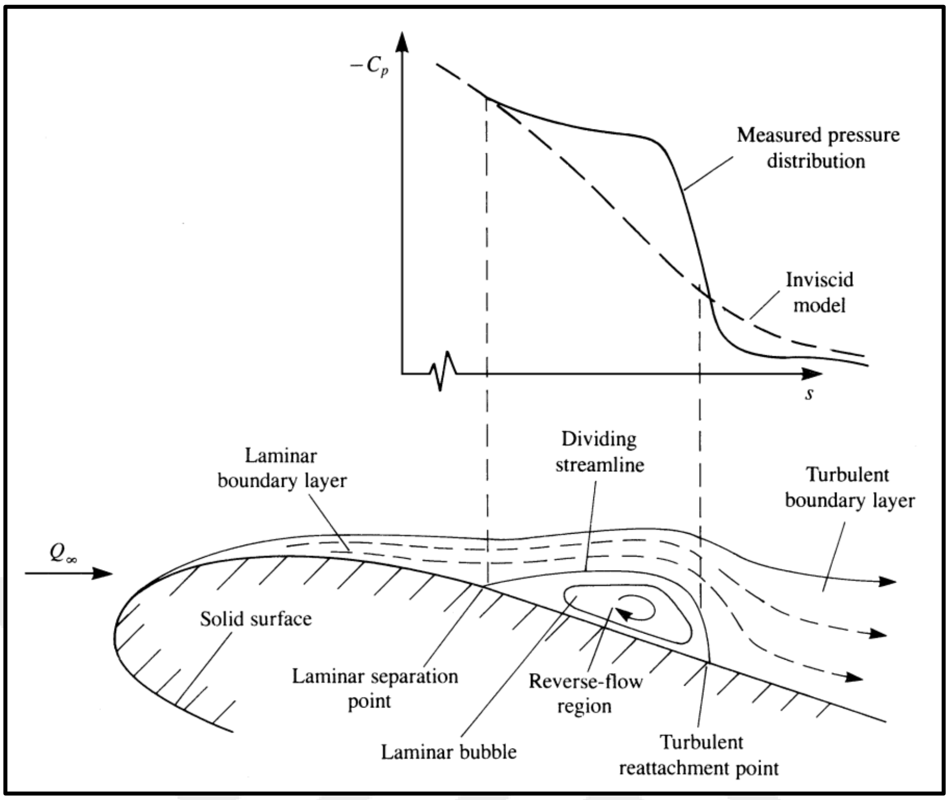

Figure 1.8. Formation of Laminar Separation Bubble with Representation of Pressure Coefficient (Katz and Plotkin, 1991)

If the laminar separation bubble is investigated in detail, it is observed that the flow turns into turbulence just before the flow begins to re-attach to the surface. The size of the laminar separation bubble can increase or decrease with the early or later transition of the flow to turbulence on the airfoil. Figure 1.9a and 1.9b depict short and long LSB caused by early or later re-attachment. If the flow separates close to trailing edge without reattachment, aerodynamic stall occurs (Fig.1.9 c).

The formation of a laminar separation bubble affects the aerodynamic performance as well as many undesirable effects. Some of them are vibration, noise, control (stability), decrease in the lift, and increase in drag, these are caused by the increase in the size of the LSB.

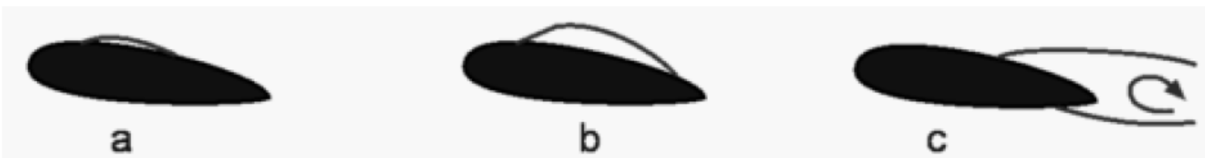

Figure 1.9. Types and Location of Laminar Separation Bubble Formed over Airfoil (Separation Bubble, 2021)

1.4. Flow Control Methods

In bubble area where the flow interacts with the body, some undesirable effects occur. Some of these are vibration, noise, flow separations, performance fall, etc. can be counted like. Control methods are used in many industry applications, and different types of control methods can be used depending on desired effect. Some of these are wind turbines, aircraft wings, car spoilers, compressor blades etc.

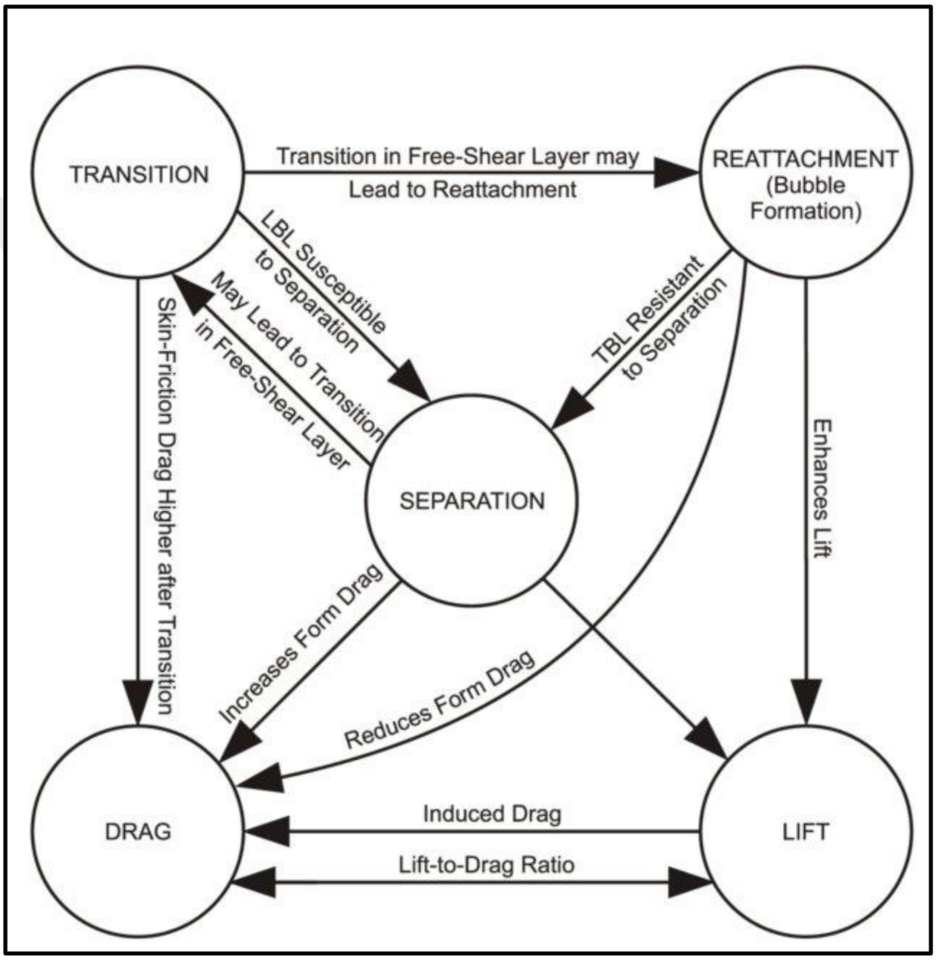

Figure 1.10. Flow Control Goals (Jahanmiri, 2010)

Figure 1.10 presents schematically different goals of flow control and their reciprocations. Some changes in flow can result in multiple benefits. Skin friction drag and noise output can be decreased by delaying laminar-turbulent transition keeping laminar flow over the suction side of the airfoil. On the other hand, some effects caused by flow control mechanisms may improve some performances while worsening others. The progression of the transition from laminar to turbulent delays the flow separation, increasing the maximum lift and decreasing the takeoff and approach field length. In contrast, an increase in skin friction drag degrades cruise performance.

As shown in Figure 1.11, flow control is divided into two categories and these are called active and passive control methods.

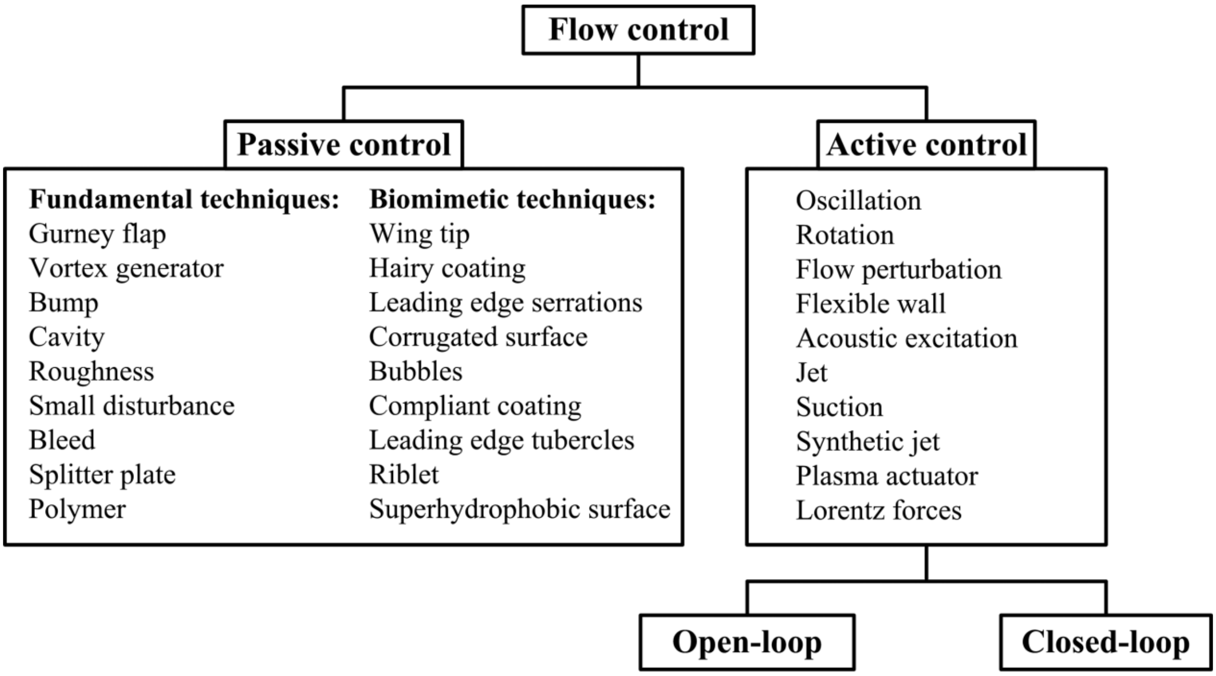

Figure 1.11. Flow Control Methods (Moghaddam and Neishabouri, 2017)

1.4.1. Active Flow Control

Active flow control mechanisms are a flow control method in which the flow around the object is controlled by providing energy input to the system without any change in the body structure. There are many type of active flow control techniques such as; rotating circular cylinders [Muddada (2010); Wong (2017)], suction and blowing [Junxuan and Xun (2015); Kamari et al., (2018)], jet flows [Zha (2007); Amitay (2001)], actuators and feedback control (Brunton (2014). The goal is to increase lift or reduce drag and suppress the vortex shedding. Some phenomena that can be controlled by active control method are given in the Figure 1.12. The main advantage of active control methods is allowing control in the required area and at desired time. However, the use of energy in the active control method is considered one of the disadvantages of this control method.

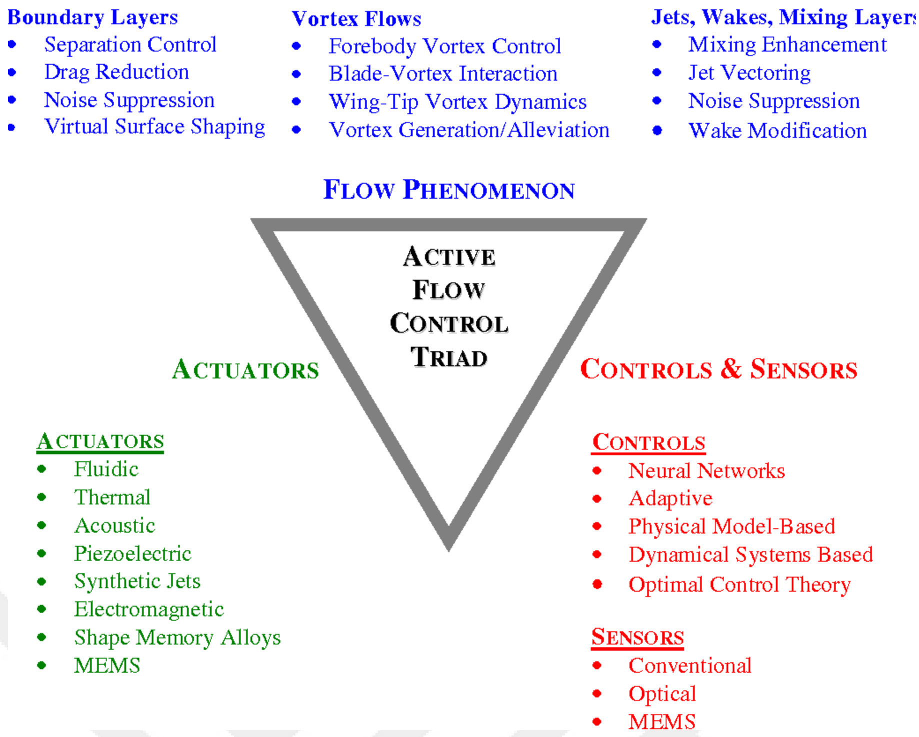

Figure 1.12. Active Flow Control Triad (Kral, 2000)

Some examples of active flow control methods are given in Figure 1.13 such as dielectric barrier discharge plasma actuator, acoustic excitation and synthetic jet actuator.

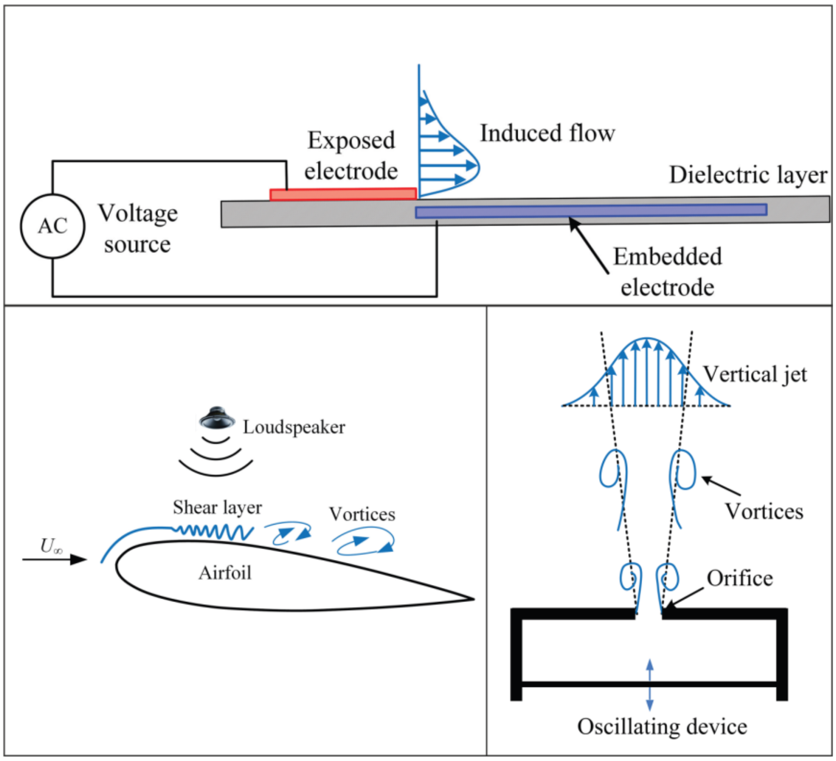

Figure 1.13. Examples of Active Flow Control (Wang and Feng, 2019)

1.4.2. Passive Flow Control

Passive flow controls are used as a geometric structure installed over body or related control location. This control method does not require energy inputs while active flow control methods require an energy input to control flow. There are many passive control methods such as; roughness surface [Zhang et al. (2018); Wu et al. (2019)], gurney flap [Storms and Jang (1994); Yee et al. (2007)], vortex generators [Kerho et al. (1993); Lin et al. (1994)], bump and cavity [Fatehi et al. (2019); Raj Mohamed et al. (2019)] etc. and these are widely used in many designs.

Some of these are winglets and vortex generators in aircraft wings, spoilers in cars, surface roughness, cavity surfaces, gurney flaps and leading edge slats in wing structures etc.

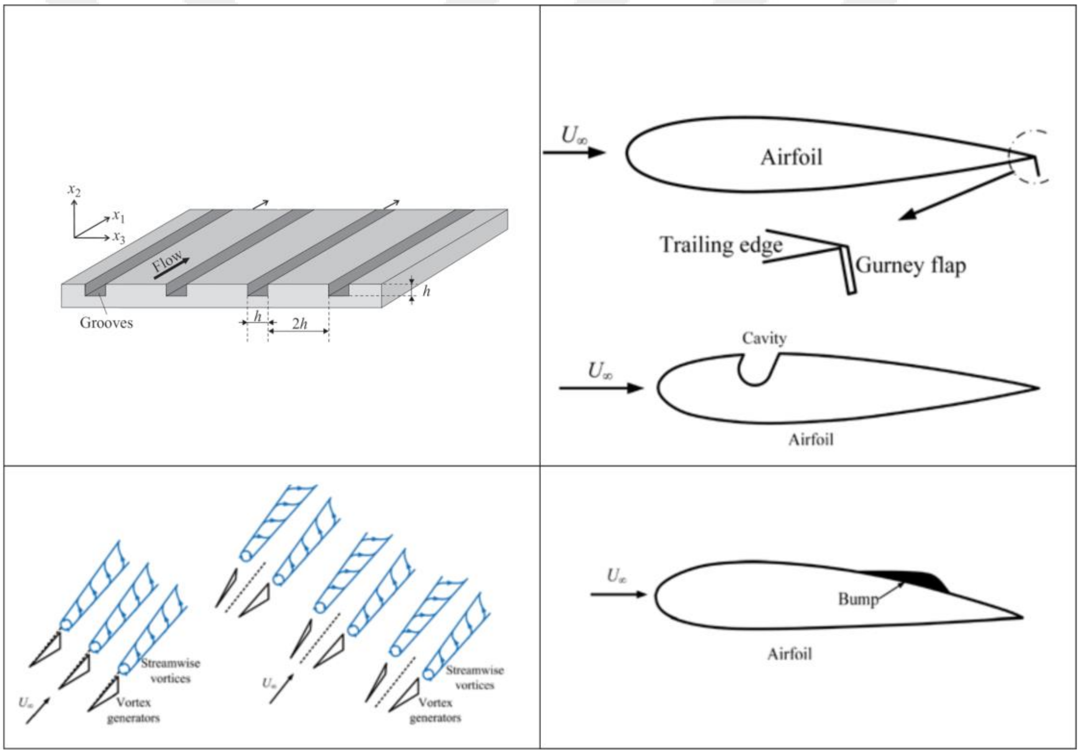

Figure 1.14. Various Passive Flow Control Methods (Wang and Feng, 2019)

In this study, NACA 0018 airfoil with riblet surface was analyzed numerically at Reynolds number of Re=1x10^5 at the angles of attack of 0°≤α≤19°. The obtained results were compared with clean airfoil results to reveal the effect of riblet surface. Fifteen model will be discussed to find optimum performance models. By using riblet control surface, it is aimed to control size, location, combination of laminar separation bubble (LSB) and trailing edge separation (TES). Increase in lift coefficient, stall delay are aimed. On the other sections, previous studies, methods of numerical study, and results of this study will be discussed.

2. LITERATURE REVIEW

2.1. Active Flow Control

2.1.1. Plasma Actuators

One of the active flow control method is using of DBD plasma actuators. DBD plasma actuators are made up an immersed electrode and a revealed electrode in spanwise and streamwise direction, separated by a dielectric sheet. Ionized air is formed when high voltage and frequency are applied to electrodes and thus a wall jet occurs. The induced flow and the free stream flow are perpendicular and it cause generation of vorticities. As a result of this, aerodynamic performance can be increased.

Jolibois et al. (2008) investigated the effect of plasma actuator on aerodynamic performance of NACA 0015 airfoil profile. Seven actuator were separately located from x/c=0.3 to x/c=0.78 and Reynolds number was set to $Re=4x10^4$. Actuator parameters were 23 kV and 1 000 Hz. Results of their study showed that flow can fully reattach to the surface up to angle of attack of $\alpha=17°$.

He et al. (2009) performed weakly ionized plasma actuator experiment. Plasma actuators were mounted on flaps and slats on NACA 0015 airfoil at Reynolds numbers of $Re=217x10^3$ and $307x10^3$. Power of actuator in these cases was set to 2W and trailing edge actuator was located at x/c=0.9 of airfoil while leading edge was covered with actuator at x/c=0. Their study showed that the leading edge separation was controlled and lift-to-drag ratio was increased by 340%. Furthermore, maximum lift coefficient and stall angle were also increased.

Moreau et al. (2016) experimentally studied DBD plasma actuator in order to delay of flow separation on NACA 0015 airfoil. Three DBD plasma actuators were separately installed on the upper side of airfoil at x/c=0.18, 0.27 and 0.37. Experiments were carried out at Reynolds number of $Re=3.3x10^6$. They compared that flow separation was occurred at x/c=0.5 on the baseline airfoil. With the implementation of DBD plasma actuator at x/c=0.18, separation point was delayed to x/c=0.65. Moreover, increase in high voltage caused shifting of separation point to x/c=0.76.

Akbıyık et al. (2017) experimentally compared linear and spanwise-segmented DBD plasma actuators on NACA 0015 airfoil. Experiment was performed at Reynolds number of $Re=36x10^3$ in a range of angle of attack $0° \leq \alpha \leq 20°$, and DBD plasma was installed on leading edge at x/c=0.1. Applied voltage and excitation frequency were 6 kV and 3.5 kHz, respectively. They observed that the lift was increased by 35% at the angle of attack of $\alpha = 10°$.

Abdollahzadeh et al. (2018) studied dielectric barrier discharge plasma actuators for stalled NACA 0012 airfoil at Reynolds number of $Re=3x10^6$. A single DBD plasma was located on the suction side of the airfoil. The applied voltage was set at 15 kV with a wide range of burst frequencies such as 5, 25, 50, 100, 250, 500, and 1000 Hz. Their study showed that the DBD plasma actuator controlled the flow structure when optimum frequency was 250 Hz.

2.1.2. Co-Flow Jet

Co-flow jet methods consist of an injection slot located on the leading edge and a suction slot installed on the trailing edge of an airfoil. The basic principle of this method is sucking air from suction slot and injecting from injection slot with a related jet momentum coefficient. By using co-flow jet, flow separations can be suppressed and aerodynamic performances increase as a result of controlling separations and boundary layer.

Zhi et al. (2021) numerically studied effects of a co-flow jet on high lift devices by using Reynolds-averaged Navier-Stokes solver enclosed with k-w-SST model. Their study was performed with NACASC(2)0712 airfoil profile at Reynolds number of $Re=5x10^5$ in the range of $-5° \leq \alpha \leq 32°$ angle of attack and a jet momentum coefficient varying from 0.08 to 0.25. They found that the jet location and the suction location on upper surfaces could change the success of the co-flow jet on a high lift device with a wide variety of parameters.

Wu et al. (2020) numerically investigated a co-flow jet on NACA6415 and NACA6415 based co-flow jet flapping airfoil at Reynolds number of $Re=7x10^4$. Numerical study was conducted with Spalart-Allmaras turbulence model. Their study showed that co-flow jet enhanced the lift and thrust coefficients. Furthermore, the propulsive efficiency was increased by 22.6% with using the co-flow jet.

Xu et al. (2015) numerically studied on co-flow jet active flow control method for S809 airfoil at a Reynolds number of $Re=2x10^6$ in the range of angle of attack $-1° \leq \alpha \leq 20°$ for a wind turbine application. An injection slot was installed near the leading edge and a suction slot was located near the trailing edge. Simulation was carried out with a jet momentum coefficient of 0.12. Their study showed that the co-flow jet had excellently positive effect on lift increase, drag reduction and stall margin. The maximum lift coefficient angle increased by 8.8°, α=12.2° to α=21°. The CL_{max} was increased by 100%.

2.1.3. Acoustic Excitation

The active control method acoustic excitation works via sending a sound wave through the loudspeaker to the flow control zone. These transmitted sound waves excites the flow and flow control is achieved in the boundary layer and shear layer.

Yarusevych et al. (2007) experimentally investigated the effect of acoustic excitation amplitude on wake region and boundary layer at low Reynolds numbers for NACA 0025 airfoil. The experiment was performed at the angle of attack of α =5° and at Reynolds number of $Re=1x10^5$ and $1.5x10^5$. The sound pressure levels of 105 dB and 106 dB were examined at the excitation frequencies of 165 Hz and 455 Hz, respectively. Obtained results showed that the acoustic excitation is remarkably affective on the flow structure and the excitation causes decreasing of boundary layer thickness and the wake region.

Yang and Spedding (2013) studied flow separation control with external acoustic excitation at low Reynolds numbers for Eppler 387 airfoil. The experiment was carried out at Reynolds numbers of $Re=4x10^4$ and $6x10^4$, at α=10° and α=8°, respectively. In addition, the experiment was performed at various acoustic excitations. Obtained results showed that the maximum increase in lift-to-drag ratio was by 70%.

Andan and Lee (2018) experimentally investigated effects of acoustic excitation on aero acoustics performance of NACA 0015 airfoil at the range of Reynolds number of $7x10^4 \leq Re \leq 9.5x10^4$ and for α=0°, 3° and 5°. The excitation amplitudes and frequencies were 70 dB, 90 dB, 3 000 Hz and 2 000 Hz, respectively. Their study showed that laminar instability was affected at the high excitation amplitude while lower excitation amplitudes had insignificant change in results.

2.1.4. Suction and Blowing

Suction and blowing control methods are used in order to suppress or break undesired flow structure over wings by sucking or blowing of flow. Using this method, the separated shear layer and boundary layer can be controlled, and also large vortex structures may be suppressed.

Junxuan and ZhenXun (2015) numerically investigated micro blowing and suction on 2D-RAE2822 supercritical airfoil at Reynolds number of Re=6.5 x10^6. Using of both suction and blowing configuration showed that lift coefficient increased by 20% and drag coefficient decreased by about 15%.

Kamari et al. (2018) performed a numerical study on active flow control using blowing and suction at Reynolds number of Re=6x10^4 for SD 7003 airfoil profile. Jet positions were in the range of x/c=0.04 to x/c=0.12 and the jet opening length was 0.11% of chord length. At the angle of attack of α=13°, the suction was highly effective with compared to other cases. It was obtained that the lift and lift-to-drag ratios increased by 94% and 500%, respectively. At the angle of attack of α=16°, lift and lift-to-drag ratios was increased by 142% and 476%, respectively.

James et al. (2018) numerically investigated a secondary blowing method to control boundary layer separation and enhance the aerodynamic performance. A simulation was carried out on NACA 0012 and LA203A airfoils in the range of $2° \leq \alpha \leq 18°$ and $2° \leq \alpha \leq 20°$, respectively when the blowing jet located to x/c=0.6 . Their study showed that blowing delayed stall angle and increased lift coefficient.

2.2. Passive Flow Control

2.2.1. Cavity

Cavity is used for airfoil flow control by trapping vortex. Suction surface of airfoil is located with cavity along spanwise direction to create a recirculation region. This cavity excites the large-scale vortex in the flow.

Fatehi et al. (2019) studied optimized cavity on Riso_B1_18 airfoil for wind turbine blades at Re=1.6x10^6. They observed that the cavity on airfoil was well capable to control the stall margin by dropping vortex, averted the flow fluctuations and they showed that the lift-to-drag ratio was increased by cavity. They also performed an experiment to validate with numerical results. The lift-to-drag ratio was increased by 31% and 57% at angle of attack of α=14° and 20°, respectively with using optimized cavity.

Raj Mohamed et al. (2019) performed a numerical study on NACA 2412 airfoil with bio-inspired nose at a low subsonic speed for angle of attack in the range from α=0° to 16° . They aimed to delay the flow separation and improve aerodynamic efficiency (decreasing drag and increasing lift). They observed that maximum increase in lift-to-drag ratio was 22.4% while the average increase was 8.6% at all angles of attack.

Lam and Leung (2018) numerically investigated aeroacoustic characteristics with cavity on the suction surface of NACA 0018 airfoil at $Re=2x10^4$ and α=0°. Their study showed that the cavity enervated the noise source; however, it produced additional acoustic because of the cavity oscillation modes. They also pointed out that the cavity increased lift-to-drag ratio to 5.3.

Manolesos and Voutsinas (2016) investigated a new flap device on LI30-FB10 flat back airfoil profile, experimentally. Experiment was carried out at $Re=1.5x10^6$ and in the angles of attack range from α=-4° to 20° and they studied various type of drag reduction devices. They compared all drag reduction devices and the best device was determined as combination of an offset cavity plate and flap. They obtained that the best increase in aerodynamic efficiency was by 131%.

Taherian et al. (2017) performed an experiment for the RISO airfoil at various Reynolds number of $Re=1.5x10^3$, $2x10^3$ and $2.5x10^3$. They compared the RISO airfoil with and without cavity for thick blunt trailing edge airfoil. The airfoil profile was cut x/c=0.3 from the trailing edge. They showed that the cutting trailing edge performed a positive effect on the wake region downstream of the airfoil when separation occurred. In addition, they showed that the adding cavity on the blunt trailing edge increased the momentum and because of this, more reduction was obtained in the wake. Therefore, drag was reduced with compared to the base airfoil.

Olsman and Colonius (2011) presented 2D direct numerical simulation with cavity on the NACA 0018 airfoil and compared the numerical results with the experimental flow visualizations. Flow regime was set to $Re=2x10^3$ and the angles of attack ranged from α=0° to

15°. They pointed out that shear layer oscillations over the cavity produced small vortices and these suppressed boundary layer to downstream of the cavity. They observed positive lift at α=0° by cavity while flow was separated forward of the cavity at α=4° and α=6°.

2.2.2. Flexible Membrane Wing

Flexible membrane wings are used to control flow field for a certain broad. That method assists to increase lift slope, maximum lift coefficient and in order to delay stall to high angles of attack with compared to rigid wings.

Viieru et al. (2006) investigated flapping and flexible wings aerodynamics. They studied at Reynolds number of Re=10, 120 and $6x10^3$ which are at low Reynolds number flow regimes. They mainly focused on the dynamics of unsteady flow relation with flapping motion of wings, leading edge vortices, wake occupy systems and rotation of pitching-up. They observed that at Re=$6x10^3$, leading edge vortices were displayed a severe, conical structures. At Re=120, vortex breakdown was faded and leading edge vortices merged with the tip vortices. Furthermore, they investigated that a vortex ring was connected to leading edge vortex, tip vortex and trailing edge at Re=10.

Lian and Shyy (2007) numerically investigated the effects of laminar to turbulent transition on the aerodynamic performance of low Reynolds number flow at Re=$6x10^4$ on SD 7003 airfoil in the range of angles of attack α=-5° to α=15°. Latex membrane was set with no pretension on the suction side of the airfoil at x/c=0.33 to x/c=0.52. They indicated that the flexible wing vibrated and during this vibration process, energy-transferring processes occurred. Therefore, energy was transferred from flexible surface to fluid flow. Obtained results showed that the separation and transition process were affected by flexible wing.

Altar et al. (2012) performed an experimental analysis of aerodynamic characteristics on the flat plat membrane wing with the three different values of pre-strain 5, 7 and 10%. They performed the experiment at Re=$1.37x10^5$, $2.26x10^5$and $3.63x10^5$ at the various angles of attack up to α=27°. They found that the dependence of the mean lift before stall on the pre-stretch of model was negligibly small. In addition, they observed a powerful relation between the Reynolds number and the pre-stall mean lift at a specified level pre-strain. Reduction in the pre-strain of model was showed an increase in mean drag. Results showed that the stall angle was feebly depend on pre-strain value and it was increased at the high Reynolds number.

Timpe et al. (2013) experimentally studied the aerodynamic benefit of membrane wing. Their study was on the flat plate wing with silicone base membrane on the scalloped free trailing edge at Reynolds number of $Re=5x10^4$. They compared two different pre-strain modes of a membrane wing with 1.3% and 2.8% on the rigid plate. They showed that the lift curve linear with the finite wing theory until the angle of attack α=10°. They observed maximum lift between α=25° and 30° and this was a typical value at low aspect ratios for rigid wings, and comparison on lift curve with rigid and membrane wing were approximately 20% at α=10° and 25% at α=25° in the stall region. The lift-to-drag ratios were the highest value at α=6° to α=8° for all three models. They showed that the membrane wings increased the aerodynamic efficiency and at the lowest pretension 1.3%, the lift-to-drag ratio was by about 5.4.

Combes et al (2015) numerically presented a flexible fixed wing with fluid-structure interaction in order to show that was an efficient way to increase wing performance in the pre-stall flight regime. The study was conducted at $Re=7.5x10^4$ and obtained results showed that the endurance could be increased by 7% compared to a rigid wing.

Genç et al. (2016) examined flexible membrane wing with the aspect ratio AR=1, and they conducted with two flow regimes, at $Re=2.5x10^4$ and $Re=5x10^4$ for various angles of attack at α=12°, 16°, 20° and 24°. According to the results, membrane deformation was raised with the increase in angle of attack, vibrational mode was decreased and deviation of maximum standard location proceeded toward to the trailing edge of flexible membrane because of the increase in angle of attack.

Demir and Genç (2017) experimentally investigated the fluid structure interaction over flexible membrane wing at low Reynolds number with AR=3. Flow regimes were set to $Re=2.5x10^4$ and 5x104 in the range of α=0° to 25°. They pointed out that the stall angle depends on the Reynolds number. At lower Reynolds number, stall occurred earlier than higher Reynolds number. With the change of Reynolds number, they observed different vibrational modes. The results showed that the formation of at the leading edge separation was influenced by the vortices and Reynolds number.

2.2.3. Gurney Flap

The Gurney flap is a simple flat plate placed on the pressure side, suction side, or both sides of the trailing edge of the airfoil. The size of the Gurney flap can be small or big. Despite of its small length, it significantly increases the lift coefficient and the lift-to-drag ratio, but it also increases the drag coefficient.

Storms and Jang (1994) experimentally investigated the effects of Gurney flap on NACA 4412 at Reynolds number of $Re=2x10^6$. Different Gurney flap heights such as h/c=0.005, 0.01, 0.015 and 0.02 were set on the trailing edge of the airfoil. The maximum lift coefficient was increased by 31% by adding the Gurney flap. Furthermore, the drag coefficient was decreased near to the maximum lift situation.

Jang et al. (1998) numerically investigated the performance of Gurney flap on NACA 4412 airfoil with the flat plate size of 1-3%c. Gurney flap sizes were h/c=0.005, 0.01, 0.015, 0.02 and 0.03. A numerical solution was performed at Reynold number of $Re=1.64x10^6$ at α=0°, 4°, 8°, 10°, 12°, 14°, 16° and 18°. They marked that the lift coefficient was increased by 0.3 on h/c=0.015 Gurney flap model.

Yee et al. (2007) studied aerodynamic performance of Gurney flap on rotorcraft application at various Mach numbers of M=0.2 to 0.9 on NACA 0012 airfoil with flap height of h/c=0.005, 0.01, 0.02 and 0.04 by numerical solutions. They also performed static aerodynamic characteristics of the Gurney flap compared with clean airfoil at various parameters. They observed that the flap height of h/c=0.02 was the best choice for rotorcraft.

Li et al. (2007) experimentally studied Gurney flap and divergent trailing edge at Reynolds number of $Re=3.15x10^5$ for the supercritical airfoil and the divergent trailing edge airfoil, 2TM and DT5, respectively. The gurney flap heights were chosen as h/c=0.005, h/c=0.01 h/c=0.015 and h/c=0.02, for a wide range of angles of attack from α=-4° to α=8°. They showed that the Gurney flap greatly increased the lift coefficient, the maximum lift coefficient and the maximum lift-to-drag ratio on the supercritical and divergent trailing edge airfoils. They also marked that the lift was increased by shifting shock on the suction side of the airfoil. The maximum increase in both lift and lift-to-drag ratio occurred at h/c=0.02 by 29.2% and 41%, respectively, while increase in lift for the divergent trailing edge supercritical airfoil was 22.3% and 33% at h/c=0.02.

Singh et al. (2007) numerically investigated Gurney flap on NACA 0011 and NACA 4412 in order to show flow field over the airfoils. Their study conducted at Reynolds number of Re=2.2×10^6 at h/c=0.01, h/c=0.02and h/c=0.03 height of Gurney flap on NACA 0011 and at h/c=0.005, h/c=0.01, h/c=0.015 and h/c=0.02 height of Gurney flap on NACA 4412 airfoil at the various angles of attack. They showed that the Gurney flap at low angles of attack, aerodynamic efficiency was increased on the NACA 0011 airfoil while it was not observed on the NACA 4412 airfoil.

Yu et al. (2011) numerically studied the effects of Gurney flap on RAE-2822 supercritical airfoil. The numerical study was conducted with the height of h/c=0.0025 to 0.03 at Reynolds number of Re=5.8×10^6.They observed that the lift of pre-stall and lift-to-drag ratio were increased at low angles of attack. Furthermore, they stated that the takeoff, landing and cruise phase were significantly improved by the Gurney flap height below h/c=0.01.

Daniel and Traub (2013) studied the effects of aspect ratio on Gurney flap aerodynamic performance, experimentally. They experimented with a Reynolds number of Re=2.5×10^5 and angles of attack from α=-6° to 28° with an increase of 2° for the aspect ratio of AR=1, 2 and 3, and the heights of Gurney flap were h/c=0.01, 0.02 and 0.04 on S8036 airfoil. They found that a decrease in aspect ratio and an increase in flap height were required to achieve better aerodynamic efficiency.

Meena et al. (2018) numerically studied the effects of Gurney flap on wake modification of airfoils at low Reynolds number of Re=1×10^3 with four different airfoil profiles such as NACA 0000, NACA 0006, NACA 0012 and NACA 0018. They analyzed a wide range of angles of attack from α=0° to 20° and Gurney flaps heights of h/x=0.3, h/x=0.06, and h/x=0.1. They observed an increase twice in a lift-to-drag ratio by installing a Gurney flap over trailing edge of the airfoil. However, the drag coefficient also increased by the raise of the angle of attack. The maximum lift-to-drag ratio was increased at h/x=0.1 for all airfoil profiles with compared the base airfoil.

2.2.4. Leading Edge Serrations

The leading edge serrations are a passive flow control method, a kind of bioinspired technology inspired from animals. It is used in order to control boundary layer separation by shaping the leading edge of an airfoil.

Ito (2009) experimentally studied leading edge serration on airfoils inspired by an owl wing in order to show aerodynamic effects at low Reynolds number flow at Re=2.1x10^4 and 2.1x10^5. Angles of attack were ranged from α=-10° to 45°. Leading edges were grouped into three group with the 16, 20 and 26 teeth/inch. They observed a slight change on values by the increase in the angle of attack. At Re=2.1x10^4, 20 and 26 teeth/inch were showed better performance than base model and 16 teeth/inch on the lift coefficient while the lift coefficient at Re=2.1x10^5 was unsatisfactory.

Winzen et al. (2014) experimentally performed leading edge serrations inspired by owl, conducted in the range of Re=4x10^4 to 1.2x10^5 and angles of attack from α=-15° to 20°. They analyzed three models which are clean, metal and silicon based serration materials. The height of the serrations was 2 mm with a diameter of 0.3 mm and the spacing between serrations was set to 1 mm. Their study showed that the serrations reduced aerodynamic performance and resulted in a higher drag, especially for the metal serrations. The lift coefficient was increased by about 10% at a ≥ 10° on the metal serration.

Narayanan et al. (2015) experimentally investigated the effects of leading edge serrations in order to reduce noise. The leading edge serration profiles were formed by sinusoidal profile. A NACA-65 and a flat plate were studied to compare the differences in noise reduction. Significant noise reduction was observed at medium frequencies in the range of 500 Hz and 8 kHz, while it was insignificant at low frequencies.

Bidermann et al. (2017) performed an aeroacoustic study by leading edge and sinusoidal leading edge on the noise reduction mechanism in order to determine the influences and dependencies on the turbulence intensity, serration amplitude, wavelength, angle of attack and Reynolds number. They studied a NACA 65(12)10 airfoil at chord Reynolds number range of 2.5x10^5 ≤ Re ≤ 6x10^5 with and without leading edge serrations.

2.2.5. Leading Edge Slats

The leading edge slats are known as a passive flow control mechanism in order to delay flow separation on aircrafts. The space between main wing and slat is increased and that causes acceleration in flow by large and small vortices. Acceleration on flow causes increase in kinetic energy and momentum, thus delaying stall.

Bangalore and Sankar (1995) numerically investigated leading edge slats at rotors in order to show aerodynamic performance. They studied with VR7 and UH-60A with baseline and slatted rotors at Reynolds number of $Re=2.75x10^6$. They showed that leading edge slats affected the hovering performance of rotor at high angles of attack and that the rotor with slats produced more thrust with less power consumption.

Bangalore and Sankar (1997) examined forward flight of slatted rotors, numerically. They studied a UH-60A rotor at tip Mach number of Ma=0.628. Coefficient of pressure, lift, drag and normal force were depicted on the baseline and the slatted rotor. Obtained results showed that the slat had benefit on replacement retreating side dynamic stall and it reduced the pitching moments and torque on retreating side by comparing with the baseline rotor.

Mishra and Baeder (2016) numerically studied leading edge slat on rotor performance at free stream Mach number of Ma=0.157 and tip Mach number of $Ma_{tip}=0.665$. The SC2110 was chosen as the main airfoil and slats were S-1 and S-6. The thrust was increased by 10% on the S-6 slat model. They pointed out that S-1 and S-6 slats were highly powerful on rotor performance even in the hardest flight condition.

2.2.6. Micro Small Cylinder

Micro small cylinders are used to control boundary layer separation and to retard the stall angle of wing. Depending on application, they can cause suppression of the vortex shedding and change flow structure over the wing by installing around any location of wing.

Li et al. (2014) experimentally investigated rod and airfoil configurations to show the influence of vortex structure based on noise radiation. The NACA 0012 airfoil was studied with eight different rod diameters of D=3mm, 5mm, 8mm, 11mm, 15mm, 18mm, 21mm and 25mm, and also a square rod with height of H=15mm were used. Space between airfoil and rod was ranged from L=30 to L=170mm. The experiment was conducted at Re_D= $6.3x10^3$ to Re_D=$106x10^3$ based on rod diameter and at Re_C=$45x10^3$ to Re_C=$90x10^3$ based on airfoil chord length. They showed that the critical gap/diameter ratio of L/D= 3.3 has the highest decrease in noise level by more than 30 dB.

Luo et al. (2017) investigated the effects of micro cylinder near the leading edge of airfoil, numerically. The chord Reynolds number of NACA 0012 were at Re=$6x10^6$ and rod were mounted with two angles of attack, at α=16° and 23° with respect to chord axis. The diameter of rod was varied from D/c=0.005 to 0.02 and spacing between rod and airfoil was ranged from s/c=0.005 to 0.035. They showed that the location and the space had a significant effect on stall conditions.

Rousoulis et al. (2017) numerically investigated the effects of rotational rod, installed in front of the airfoil in order to noise control. A NACA 0012 and circular rod were coupled and were spaced by the chord length. The study was carried out at Reynolds number based on airfoil chord length and diameter of cylinder at Re_C=4.8x105and Re_D=4.8x104, respectively. Frequencies were between 0.5 and 2 times the natural shedding frequency. They showed that the rotation of cylinder highly effected noise reduction.

2.2.7. Partially Flexible Wings

Partially flexible wings are used in the same way as flexible membrane wings. However, the flexibility is closed with an area over the wing surface, whereas the flexible membrane wings are covered along span-wise direction. The partially added flexibility is used to control the flow regionally.

Cleaver et al. (2014) experimentally investigated the partially flexible wing attached on the trailing edge of NACA 0012 for different flexibilities and lengths of the flexible part at a Reynolds number of Re=4x104. Stainless steel, vinyl, polyester and aluminum were tested for the length of flexible part of l/c=0.1, l/c=0.3 and l/c=0.3 . They obtained the highest improvement on the largest flexible plate more thrust than base model by 28%.

Açıkel and Genç (2018) experimentally studied the effect of a partially flexible wing mounted on the suction side of a NACA 4412 wind turbine blade between x/c=0.2 and x/c=0.7 at different Reynolds number of Re=2.5x10^4, 5x10^4, 7.5x10^4. The lift-to-drag ratio was increased about 100% at Re=2.5x104 and at α=6° by suppressing laminar separation bubble. In addition, the lift coefficient was increased while the drag coefficient was reduced.

2.2.8. Slotted Airfoils

Slotted airfoil control method is based on increasing flow velocity by a corridor on the airfoil. flow velocity increases at the exit of corridor and increase in velocity causes the flow separation over the airfoil. The flow separation means that reduction in mean velocity. By decreasing the velocity, pressure increases and produces lift force.

Baragona et al. (2003) investigated both experimentally and numerically the effect of a single slotted flap in order to show changes in aerodynamic performance at Reynolds number of Re=2x10^6 in the range of angle of attack from α=-6° to 15° for NACA 63-415 airfoil. The gap between main airfoil and flap ratios were gap distance of g/c=0.015, 0.02, 0.025, 0.03, 0.035, 0.04 and overlap distance of O/c=0.01 and 0.02. The maximum lift coefficient was observed 2.53 at g/c=0.03 and O/c=0.02 configuration.

Belamadi et al (2016) numerically investigated the improvement of aerodynamic performance at Reynolds number of Re=1x10^6 with various slot configurations at x/c=0.2 to 0.8 at slot slope β=-60° and slot width of y/c=0.01. The simulation was carried out for NREL S809 airfoil with 21% thick of airfoil chord length. This airfoil was generally used for horizontal axis wind turbine blade in the range of angles of attack α=15° to 20°. The results were compared for all configuration and angles of attack with each other. The highest lift coefficient was about 1.5 at α=20° with the final configuration.

Ni et al. (2019) numerically studied effects of a slotted airfoil on wind energy applications. A NACA 634-021 airfoil with internal slot was tested in the range of angles of attack α=0° to 30° with nine different slot configurations at Reynolds number of Re=1x10^5. An experimental study was also performed to compare numerical results and it was well matched with the numerical solutions. At the optimal design, increase in maximum lift and increase in lift-to-drag ratio was by 58% and 14%, respectively.

Mohamed et al. (2020) performed a numerical study on the slotted airfoil of Darrieus wind turbine. The NACA 0018 airfoil was performed at Reynolds number of Re=2.5x10^5 in the range of angles of attack from α=0° to 30°. Ten configurations were performed such as W/C ratio from 0.02 to 0.035, L/C ratio from 0.15 to 0.35 and β was ranged from β=45° to 60°. Their study observed that the slotted airfoil positively affected delay on boundary layer separation at the high angle of attack, increased lift and decreased drag.

2.2.9. Splitter Plate

A splitter plate is a simple plate placed over the body upstream, downstream, or both upstream and downstream of the body to control recirculation area, length of vortex formation, and drag coefficient reduction by changing the influence of the upper and lower shear layers.

Nakagawa (1992) experimentally investigated the effect of NACA 0018 airfoil used as a splitter plate behind of a square prism. They performed experiment between at Mach number of Ma=0.11 and Ma=0.91. The space between airfoil and square prism was with the ratio of L/D=2, when the chord length and square side length were 20 mm. The shear layers and vortices were controlled by the presence of an airfoil behind of a square prism. Obtained results showed that the Strouhal number was independent from Mach number. With the appearance of shock waves, Strouhal number was suddenly increased and also, it was showed that the increase in Strouhal was continued with the increase of Mach number.

Metzinger et al. (2018) investigated experimentally and numerically the effect of a splitter plate attached the trailing edge of the FB-3500-1750 airfoil with a trailing edge thickness 17% and maximum thickness 35% of the chord length to investigate the aerodynamic performance and vortex shedding behavior of splitter plate. They conducted at the Reynolds number of Re=6.66x10^5 and splitter plate was between 50 to 150% of the trailing edge length. The increase in the splitter plate length was showed some adverse effects, such as an increase in base drag and loss in the maximum lift. Also, study showed that the increase in splitter plate length was depicted raise on Strouhal number. The best splitter plate configuration was the 50% of trailing edge thickness, and it showed that the increase in drag and decrease in maximum lift was by 27% and 5%, respectively.

Song (2020) numerically investigated splitter plate on a DU97-W-300 wind turbine airfoil with a flat back trailing edge and a splitter plate added configuration. The numerical solution performed at Reynolds number of $Re=3x10^6$ at a constant angle of attack, α=4°. The flat back and splitter plate length was 10% of chord length. They obtained that the addition of splitter plate remarkably effected the wake flow and decrease in drag and noise.

Ozkan (2021) experimentally showed that the behaviors of a splitter plate mounted on the trailing edge of a NACA 0012 at the angle of attack of α =16° and at Reynolds number of $Re=2x10^4$. Various splitter plate and chord length ratios were implemented such as L/C =0.1, 0.2 and 0.3 and compared with the base airfoil. This study showed that the trailing edge vortex was rolled up and turbulent structures were moderately prevented by the use of splitter plate on L/C =0.2, and longer length of vortex formation was occurred at L/C=0.3. The turbulence fluctuations were decreased and vortex-shedding frequency was weakened in the airfoil wake region.

2.2.10. Vortex Generators

Vortex generators are small devices that placed over the wing surface in order to induce stream-wise vortex. Flat plate, wedge, ramp, airfoil, wishbone are the types of vortex generators. They are used to control flow separation by increasing momentum mixing. They have a wide range of use from low to high flow velocity.

Bragg and Gregorek (1987) experimentally studied the effects of vortex generators on airfoil characteristic performance. The experiment was performed at Reynolds number of $Re=9x10^5$ for Voyager canard airfoil at various angle of attack ranges from α=-4° to 18° and three types of vortex generator were used such as small vortex generator, large vortex generator and delta vortex generator. They attached the vortex generators at x/c=0.17 and 0.45 for small vortex generators while large and delta vortex generators were only at x/c=0.45. Obtained results showed that four configuration of vortex generators increased lift coefficient and decreased drag coefficient. They recommended the delta vortex generator because of the low increase in drag and high increase in lift.

Kerho et al. (1993) experimentally investigated effect of the sizing and spacing of vortex generators installed on Liebeck LA2573A airfoil to show behavior of vortex generators on laminar separation bubble. The experiment was carried out from Reynolds number of Re=2x10^5 to 6x10^5 in the angles of attack below the stall angle. They showed that the use of vortex generator decreased drag at lower Reynolds number, such as at C_L=0.572 drag reduction was maximum by 38% at Re=2.35x10^5.

Lin et al. (1994) experimentally investigated the effects of vortex generators to control separation on the high lift airfoils. The experiment was carried out at Reynolds number of Re=5x10^6 and Re=9x10^6 and various angles of attack ranges from α=-4° to 24°. They indicated that the optimum high lift configuration was achieved when the vortex generators were applied on flap, found at z/c=0.0018 to get maximum lift and optimum location was x/c=25. Moreover, the hidden vortex generators caused no drag during cruise flight.

Seshagiri et al. (2009) investigated aerodynamic performance of vortex generators on airfoil at low Reynolds number flow with six different static vortex generators. In addition, an active vortex generator was also tested. The experiment was performed at Reynolds number of Re=8x10^4 000 and Re=1.6x10^5 in the angles of attack range from α=-4° to 18°. All vortex generator configurations increased lift coefficient. The maximum lift coefficient increased by 25% at Re=1.6x10^5 while active vortex generator was not effective as static vortex generators.

2.2.11. Riblets and Roughness Surfaces

Riblets and roughness surfaces are drag reduction mechanisms. These surfaces form small vortices and cause flow re-energized. The flow has more momentum energy and it causes suppression on separated flow by re-energized flow.

Huber and Mueller (1987) experimentally investigated trip wire roughness on the Wortmann FX- 63-137 airfoil. The experiment was carried out at Reynolds number of Re=1x10^5 in the range of angle of attack from α=-16° to 24°. The trip wire was located at the front of the pressure surface of the airfoil between 0.01< x/c <0.03, with a roughness height to chord ratio h/c=0.00583 and 0.003. The maximum lift was observed at the angle of attack α=15° around C_L=1.54.

Wang et al. (2000) experimentally investigated the effect of riblet surface on turbulent boundary layer for a flat plate surface at freestream velocity 17.5 m/s. The V-type riblet surface was covered over the flat plate with the parameters; height, width and spacing, 1mm, 1mm, 2mm, respectively. Obtained results showed that the riblet surface showed good results with compared smooth plate and turbulent intensity was increased about 6.7%, however, its position was decreased by 6.4%. They also proved that the riblet surface caused turbulent drag reduction.

Gopalarathnam et al. (2001) experimentally performed a low Reynolds number airfoil design by using trips in the range of $1x10^5 < Re < 3x10^5$. Three different airfoil were studied with various trip location configurations. Airfoil profiles were SA 7024, SA7025, SA7026 and trip locations were at the upper surface of airfoil x/c=0.1, x/c=0.2, x/c=0.3 and x/c=0.1. They showed that the trips were useful for drag reduction and lift enhancement at low Reynolds number flow than high Reynolds number flow.

Lee et al. (2005) experimentally studied the effect of fully covered riblet film over a circular cylinder at Reynolds number of $2.5x10^3 < Re < 3.8x10^4$ with the parameters, height and space between riblets were h=180 μm and s=300 μm. Their study depicted that drag coefficient was decreased by 7.6% at $Re=3.6x10^3$ while increasing drag about 4.2% at $Re=3.6x10^4$.

Lee and Jang (2005) experimentally performed micro riblet film installed on the suction side of NACA 0012 airfoil to control flow. The Experiment conducted in low Reynolds number flow in the range of $1.03x10^4 < Re < 5.14x10^4$. The riblet shape was V-shaped with the dimensions, height of h=176.8 μm, spacing between grooves of s=300 μm and valley of groove were w=50 μm. Obtained results showed that drag force was decreased by 6.6% with compared smooth airfoil at $Re=1.54x10^4$ while drag force increased by 9.8% at $Re=4.62x10^4$.

Riblet film was used for drag reduction method applied to wind turbine airfoils by Sareen et al. (2014). Three different flow regimes were performed such as at $Re=10^6$, $1.5x10^6$ and $1.85x10^6$ with four V-shaped riblet height configurations 44, 62, 100 and 150 μm. The DU 96-W-180 airfoil was covered by riblet film along x/c=0.4 to x/c=1.0 of the suction side of the airfoil and x/c=0.7 to x/c =1.0 of the pressure surface of the airfoil. In all configurations, 62-μm riblet size was obtained as the optimum size, and drag was decreased by 4.5%.

Zhang et al. (2018) performed a large eddy simulation on riblet surface airfoil. An Eppler E374 airfoil was simulated at Reynolds number of $Re=2x10^5$ at the angle of attack $\alpha=3°$. The isosceles triangle riblets were installed along x/c=0.3 to x/c=99 with a width of w/c=0.0025 and a height of h/c=0.002. In addition, they attached a trip at x/c=0.13 with the w/c=0.01. The lift coefficient was increased while friction drag coefficient, Reynolds stresses and vortex structure in the boundary layer were decreased.

Wu et al. (2019) investigated transverse groove structure on NACA 0012 airfoil at low Reynolds number flow regimes with variation of spacing with s=0.1, 0.2, 0.5 and 1 mm. The height and the distance between tips of the riblet were equal with spacing length. The riblets were installed between x/c=0.3 to x/c=0.7 named as middle part and x/c=0.5 to x/c=0.9 named as posterior part. They showed that the transverse groove decreased drag by 9.65% on s=0.1 mm configuration.

Tiainen et al. (2020) studied trapezoidal riblets on airfoil and wind turbine performance. They studied in the range of Reynolds number of $8.3x10^4 < Re < 2.48x10^5$ with height and spacing of riblet h=0.149 mm and s=0.298 mm at λ=30° trapezoid angle. The riblets were installed at x/c=0.65 to x/c=0.9 of NACA 0024 airfoil. They observed that the reduction in drag was up to 6.8% and Reynolds stress was decreased up to 80%. Furthermore, they successfully increased power coefficient by 10.9% for three bladed horizontal axis wind turbine.

3. MATERIALS AND METHODS

The present chapter introduces numerical simulation domain, airfoil geometry, mesh information, riblet shapes, locations and sizes. Performing experimental study poses some financial obligations and difficulties while computational fluid analysis provides reduction of cost and time, detail information about flow. The number of computational studies on aerodynamic increases due to faster computer in recent years. In the present study, 2-D numerical analysis on NACA 0018 airfoil was performed using ANSYS FLUENT computational fluid dynamic (CFD) package program.

The Reynolds Number, which is one of the best known and most used dimensionless numbers in fluid mechanics, is determined as the ratio of fluid's inertial forces to viscous forces. It was defined by Osborne Reynolds in 1883 in pipe flow and is a very important dimensionless parameter that serves to define whether the flow is laminar or turbulent regime.

$$Re = \frac{\rho V_\infty L}{\mu} \tag{1}$$

In the dimensionless formula, ρ is the density of the fluid, $V\infty$ is the free flow velocity, L is the characteristic length and μ is the dynamic viscosity. When the Reynolds Number is adapted for the airfoil, the airfoil chord length size c is taken as characteristic and the formula for the airfoil can be arranged.

$$Re = \frac{\rho V_\infty c}{\mu} \tag{2}$$

In the present numerical analysis, Reynolds number was kept to constant as $Re=1x10^5$.

Due to the using of non-dimensional numbers, the aerodynamic performance can be compared for different cases. Thus, the using of these dimensionless parameters play a major role in the aerodynamic studies. In order to interpret the performance of the wings, some dimensionless parameters have been derived. With these parameters, the airfoil performance can be evaluated for different angles of attack. Some of the main dimensionless parameters used in aerodynamics are lift coefficient, drag coefficient and pressure coefficient. Lift force has a great importance for the device to be designed at the preliminary design stage, and changes can be made in advanced design stages. With the change of the airfoil profile and angle of attack, the wing can exhibit different types of flow structure. The most important information given by the lift force is the stall angle and it states that the efficiency of the vehicle starts to show a negative effect on the determined angle of attack. The drag force refers to the resistance effect between the fluid and the airfoil. All bluff bodies that interact with the fluid create a specific resistance force between the fluid and surface. This resistance force may vary according to the wing profile, angle of attack and flow regime. The pressure coefficient, on the other hand, is a dimensionless parameter obtained by proportioning the static pressure and dynamic pressure of the flow around the body, and it is a dimensionless number that helps to interpret the pressure distribution on the airfoil.

$$C_L = \frac{F_L}{\frac{1}{2}\rho {V_\infty}^2 A} \tag{3}$$

$$C_D = \frac{F_D}{\frac{1}{2}\rho {V_\infty}^2 A} \tag{4}$$

$$C_P = \frac{P - P_\infty}{\frac{1}{2}\rho {V_\infty}^2} \tag{5}$$

In the formulas given above, C_L is lift coefficient, C_D is drag coefficient, C_P is pressure coefficient, F_L is lift force, F_D is drag force, P is static pressure at the measured point on the wing, P_∞ is free flow static pressure, ρ is fluid density, V_∞ is free stream velocity and A indicates wing reference area.

3.1. Model and Computational Grid

NACA 0018 airfoil was numerically analyzed as test case. The chord length of airfoil was selected as 200 mm. Flow domain was sketched in Figure 3.1. The coordinate system was located at the trailing edge of airfoil. In order to prevent the deterioration of the flow structure due to wall effect, the fluid domain was extended 12.5c in the y-axis direction and 25c along the x-axis diretion. C-type mesh structure was created by ICEM CFD. The using of the C-type mesh structure enables a better distribution on the airfoil especially near the wall, so, it provides more accurate solutions for boundary later. Also, it reduces time effort and memory. The mesh structure around NACA 0018 was shown in the Figure 3.3. Total of 500 000 mesh cells were cretaed. The upper and lower surface of the airfoil was segmented by 350 and 310 nodes, respectively. The nearest node of streamwise distance from trailing edge and leading was $3.2x10^{-4}$m and $2.3x10^{-5}$m. Mesh quality table is given in the Table 3.1.

Table 3.1. Mesh Quality Table

	Present Study				Fluent User Guide
	Min	Max	Average	Standard Deviation	
Skewness quality	1.3E-10	0,13	0,024	0,0390	Max.Skewness<0.25 , Excellent
Orthogonal quality	0,83	1	0,997	0,00555	0.7<Min.Orthogonality<0.95 , Very Good

The first layer thickness on the airfoil was determined as $2.6x10^{-5}$m. The mesh design has been made with the y^+ value is less than 1 and shown in the Figure 3.2. As can be seen from the Figure 3.3, a mesh structure that compresses as it gets closer to the airfoil surface, in order to better solution of boundary layer problems.

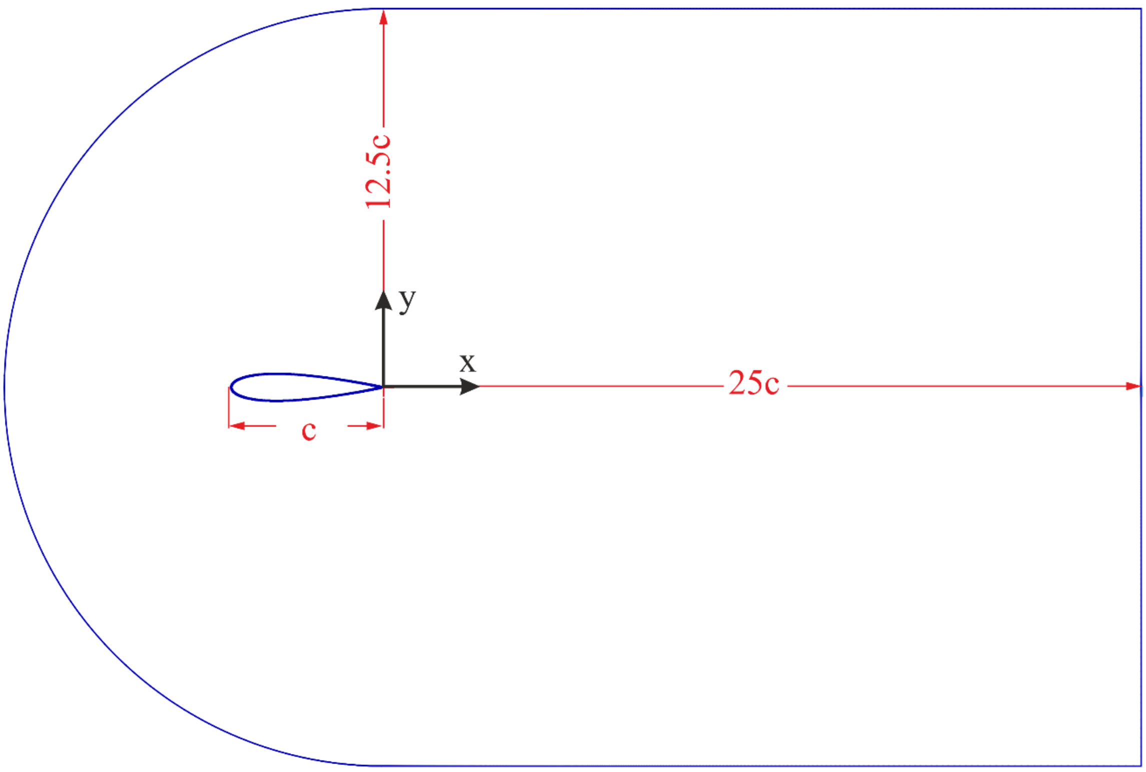

Figure 3.1. Shematic View of Flow Domain

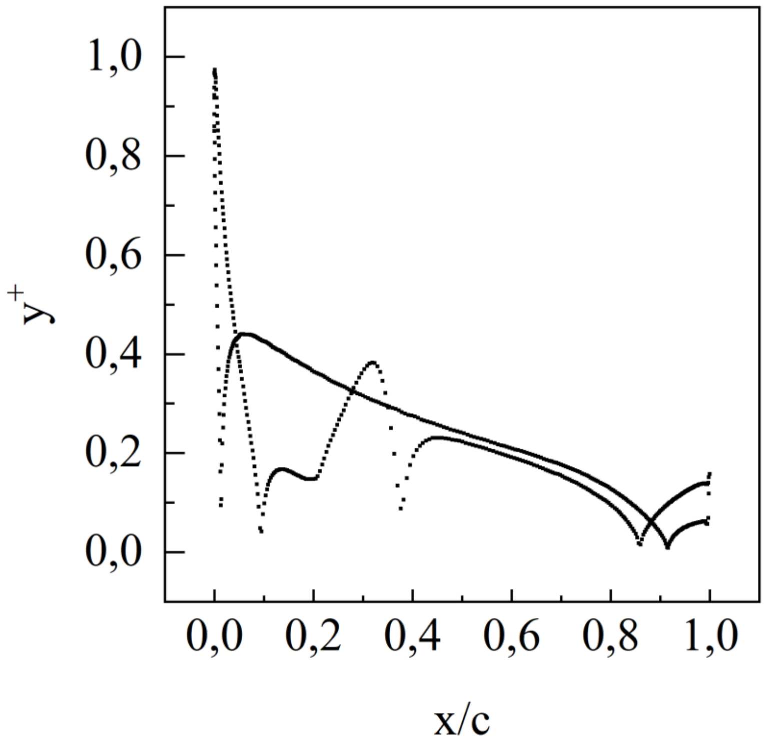

Figure 3.2. Distribution of y^+ over Airfoil

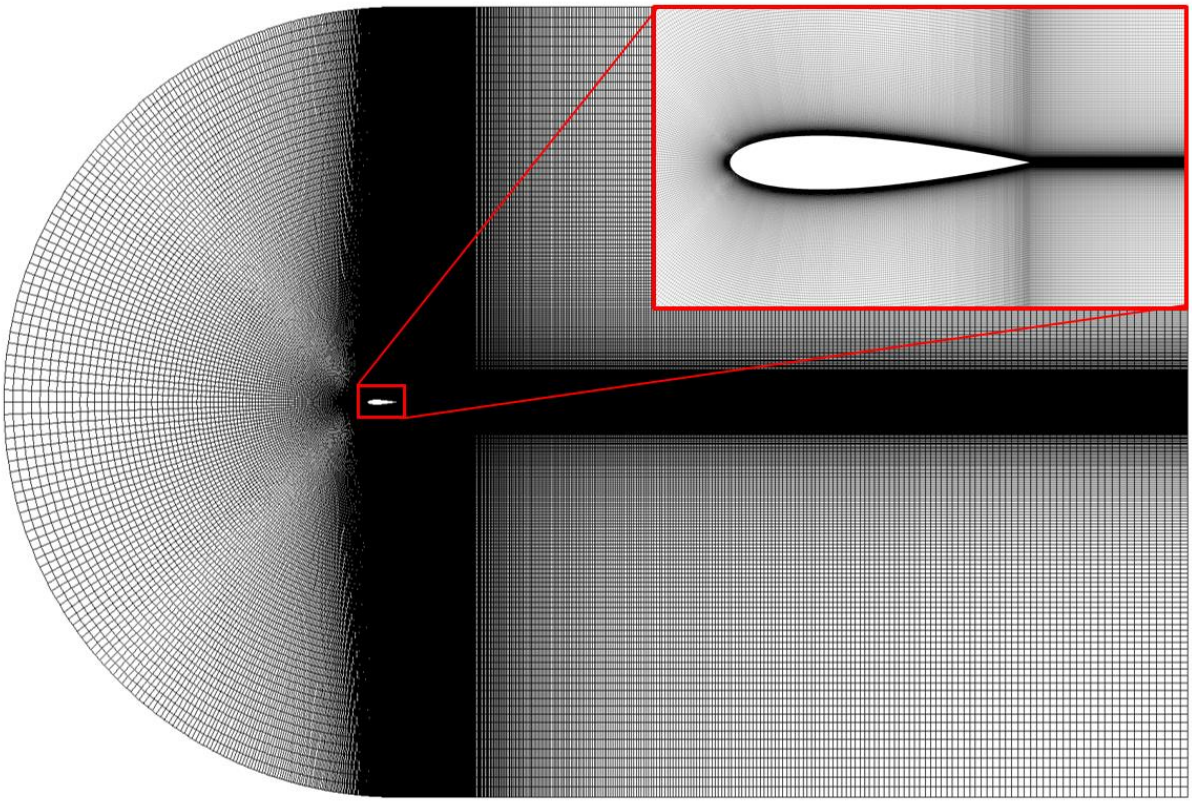

Figure 3.3. Mesh Structure of Airfoil

In this study, it is aimed to increase the aerodynamic performance of NACA 0018 airfoil by using riblet surface. The parameters of riblet was sketched in the Figure 3.4. In the Figure 3.4, the riblet height is indicated by (h), the riblet base length is indicated by (w), while the gap between the two riblet base corners is indicated by (s). A pioneer study was performed by Wu et al. (2019) on drag reduction on NACA 0012 airfoil by means of triangular riblets placed on the pressure side of airfoil. In their study, a cavity surface was carried out by opening a channel inside the wing. The sizes of cavity were determined as h = s = w and they numerically examined four different values of s. Unlike in their study, the riblets create a roughness on the suction side of airfoil in this study. The main parameters of triangular riblet were selected as height, location, the number of riblet and space between two riblet. These parameters were dimensioned by chord length of airfoil.

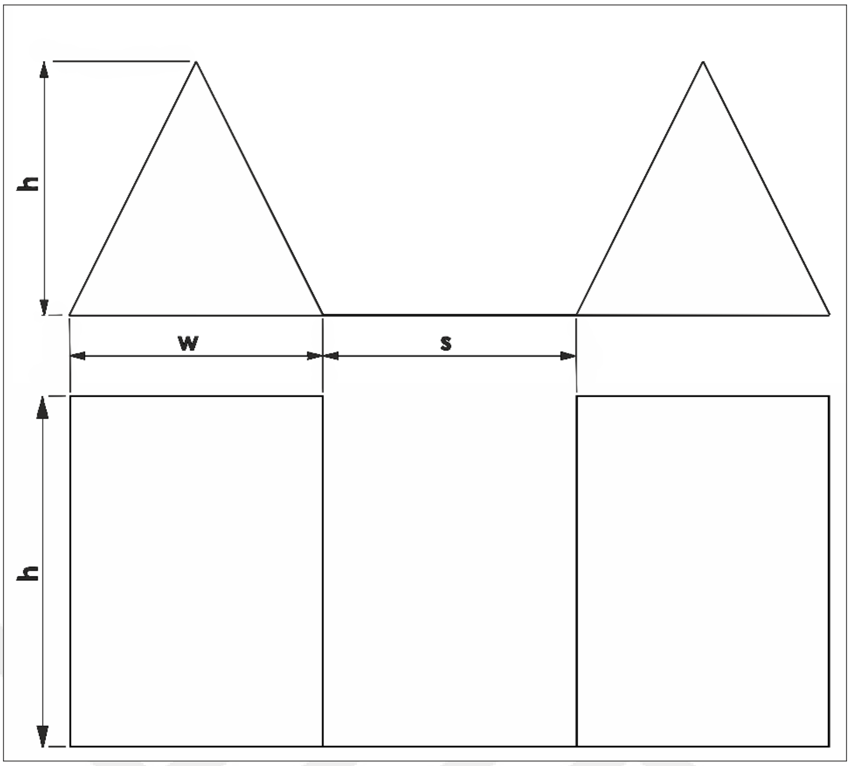

Figure 3.4. Explanation of Riblet Geometry

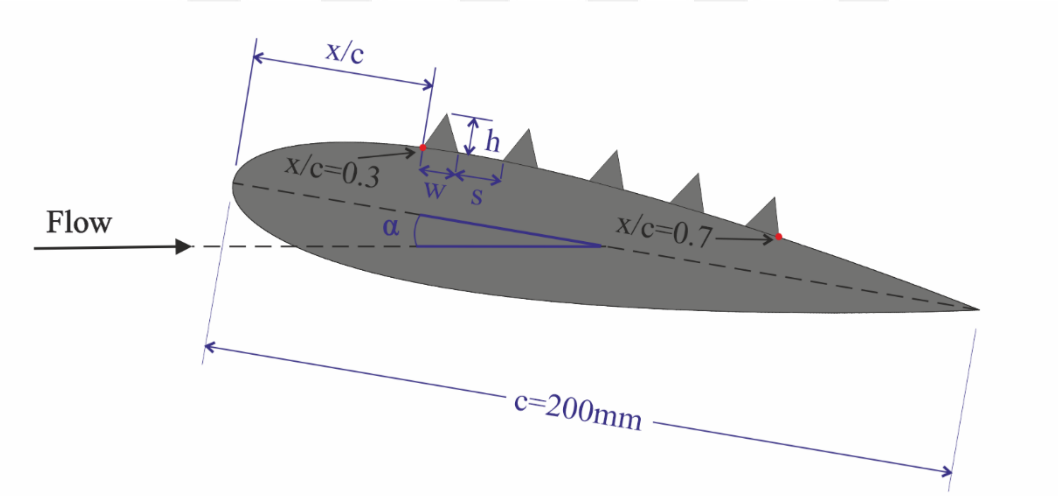

Figure 3.5. Representation of the Riblet on the Airfoil

Figure 3.5 shows a riblet over an airfoil with the parameters location(x/c), height (h), width (w) and space(s) of riblets, and angle of attack. Examined riblet configurations are given in Table 3.2. NACA 0018 smooth airfoil is called as M0 model. M1 model is a single riblet located at x/c=0.3 with height and width of h/c=w/c=0.005. M2 model is also have the same parameter except location. A single riblet is installed at x/c=0.7 on M2 model. M3 model is double riblet configuration and riblets are located at x/c=0.3 and x/c=0.7. The M1, M2 and M3 models compose of Group I. Group I concerns location of the riblets. Group II contains model M4,M5, M6 and M7. In the Group II, the effect of gap ratio is studied. All models have same height and width as models of Group I at $0.3<x/<0.7$. M4 to M7 model, density of riblet increases by decreasing space between riblets. The gap ratios of M4, M5, M6 and M7 are 0.1, 0.01, 0.005 and 0, respectively. M7 model is fully covered by riblets at $0.3<x/<0.7$ that is no space between riblets. Group III consists of M7, M8 and M9 models. The sizes of riblets of M8 and M9 are same with M7 model and there is no space between riblets. The riblets were located for M8 and M9 models in the range of $0.3<x/c<0.5$ and $0.1<x/c<0.7$, respectively. The Group IV includes M7, M10 and M11. The effect of riblet height is investigated for Group 4 and they are located at $0.3<x/<0.7$. The height of riblet is selected 0.005, 0.0025 and 0.01 for as M7, M10 and M11, respectively. At the last group, in Group V, rectangular riblets are investigated in order to reveal the effect of geometry of riblet. The widths and gap ratio are kept constant as w/c=0.002 and s/c=0.0025. The heights of M12, M13 and M14 models are h/c=0.0025, 0.005 and 0.01, respectively.

All models were analyzed for angles of attack of α=0° to α=19°, at Reynolds number of $Re=1x10^5$. C-type mesh is applied for the controlled surface in the same way as it is applied in the uncontrolled airfoil. The mesh structure around NACA 0018 with riblet surface is shown in the Figure 3.6. Total number of cells are apromimately 500 000. The riblet edges were divided into 10 nodes in order to have harmony between the riblet and airfoil surface mesh distance. The mesh structure, which becomes denser as it gets closer to the wing surface, helps the boundary layer solutions to advance correctly. As the mesh structure rises above the control surface, it expands at a growth rate of 1.2. The y^+ value specified in the uncontrolled condition is designed to be $y^+<1$ in all controlled airfoils. Detailed mesh structure of the wing profile with control surface is given in the Figure 3.6.

Table 3.2. Information of Riblet Models: Location, Height, Width and Gap Ratio

Model	x/c	h/c	w/c	s/c
M0	-	-	-	-
M1	x/c=0.3	0.005	0.005	-
M2	x/c=0.7	0.005	0.005	-
M3	x/c=0.3 and 0.7	0.005	0.005	-
M4	0.3 < x/c < 0.7	0.005	0.005	0.1
M5	0.3 < x/c < 0.7	0.005	0.005	0.01
M6	0.3 < x/c < 0.7	0.005	0.005	0.005
M7	0.3 < x/c < 0.7	0.005	0.005	0
M8	0.3 < x/c < 0.5	0.005	0.005	0
M9	0.1 < x/c < 0.7	0.005	0.005	0
M10	0.3 < x/c < 0.7	0.0025	0.005	0
M11	0.3 < x/c < 0.7	0.01	0.005	0
M12	0.3 < x/c < 0.7	0.0025	0.002	0.0025
M13	0.3 < x/c < 0.7	0.005	0.002	0.0025
M14	0.3 < x/c < 0.7	0.01	0.002	0.0025

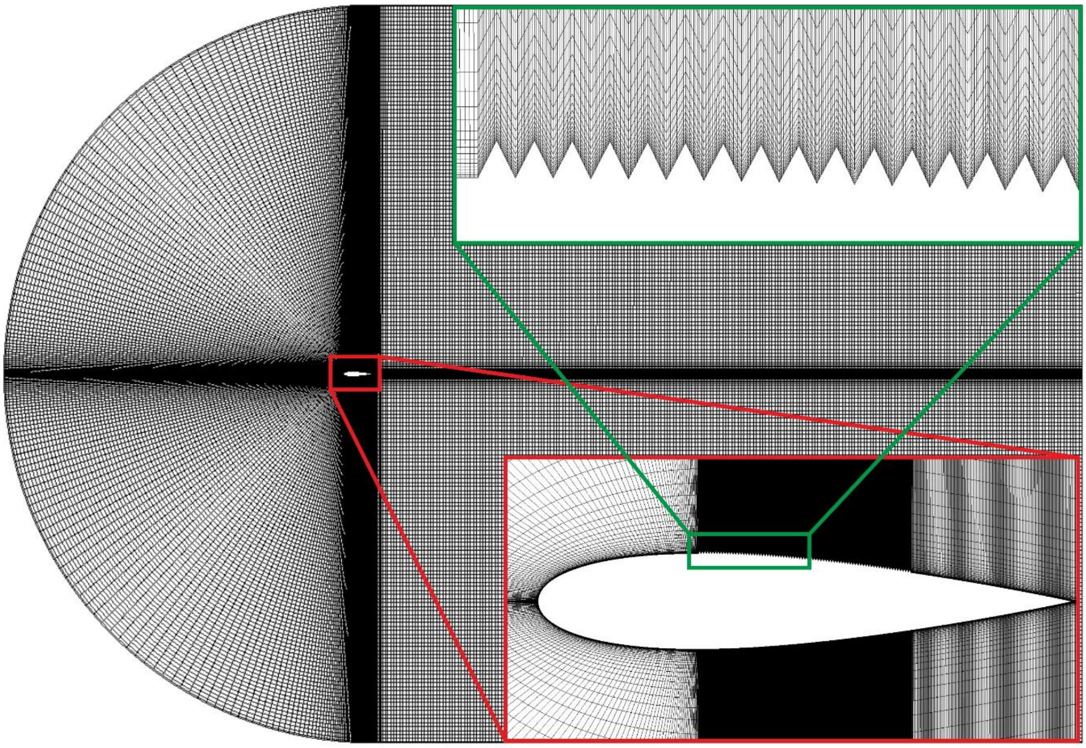

Figure 3.6. Controlled Airfoil and Mesh Structure with Close View

3.2. Numerical Model and Boundary Conditions

ANSYS Fluent is based on RANS equation derived from continuity, momentum and energy equations General form of the continuity, momentum and energy equations are given in the Eq.6, Eq.7 and Eq.8, respectively. In the equations, p stands for static pressure, $\bar{\bar{\tau}}$ to stress tensor, $\rho\vec{g}$ to gravitational force and $\vec{F}$ to body forces. On the energy equation, k_{eff} states for effective conductivity, $\vec{J}_j$ to diffusion flux of species j. Right side of the Eq.8 represent energy transfer caused by conduction, species diffusion and viscous dissipation, respectively. Also, S_h consists of heat of chemical reaction and other volumetric heat sources. (Fluent,2013)

$$\frac{\partial \rho}{\partial t} + \nabla \cdot (\rho\vec{v}) = 0 \tag{6}$$

$$\frac{\partial}{\partial t}(\rho\vec{v}) + \nabla \cdot (\rho\vec{v}\vec{v}) = -\nabla p + \nabla \cdot (\bar{\bar{\tau}}) + \rho\vec{g} + \vec{F} \tag{7}$$

$$\frac{\partial}{\partial t}(\rho E) + \nabla \cdot (\vec{v}(\rho E + p)) = \nabla \cdot \left(k_{eff}\nabla T - \sum_j h_j \vec{J}_j + \left(\tau_{eff} \cdot \vec{v}\right) \right) + S_h \tag{8}$$

The numerical analyzes were carried out with 2-D, density based, implicit formulation and k-kl-kw turbulence transition model. The transition model found by Walters and Leylek (2004) and it is used to estimate boundary layer development and calculate onset of transition. This model is useful for successfully cope with the transition of the boundary layer from a laminar to a turbulent regime and showed the capability of model in literature [Karasu et al. (2013); Aftab et al. (2016); Ahmed and Elbatran (2018); Gaggero and Villa (2018); Salimipour (2019)] k-kl-w transition model consist of three-equation eddy-viscosity type. In this model, k_T indicates turbulent kinetic energy, k_L to laminar kinetic energy and ω to specific dissipation rate. All details about transport equations and constants can be found in the study of Walters and Leylek (2004).

$$\frac{Dk_T}{Dt} = P_{k_T} + R_{BP} + R_{NAT} - \omega k_T - D_T + \frac{\partial}{\partial x_j}\left[\left(v + \frac{\alpha_T}{\sigma_k}\right)\frac{\partial k_T}{\partial x_j}\right] \tag{9}$$

$$\frac{Dk_L}{Dt} = P_{k_L} + R_{BP} + R_{NAT} - D_L + \frac{\partial}{\partial x_j}\left[v\frac{\partial k_L}{\partial x_j}\right] \tag{10}$$

$$\frac{D\omega}{Dt} = C_{\omega L}\frac{\omega}{k_T}P_{k_T} + \left(\frac{C_{\omega R}}{f_W} - 1\right)\frac{\omega}{k_T}(R_{BP} + R_{NAT}) - C_{\omega 2}\omega^2 + C_{\omega 3}f_\omega \alpha_T f_W^2 \frac{\sqrt{k_T}}{d^3} + \frac{\partial}{\partial x_j}\left[\left(v + \frac{\alpha_T}{\sigma_\omega}\right)\frac{\partial \omega}{\partial x_j}\right] \quad (11)$$

All solutions were analyzed steady-state solution by using coupled-implicit algorithm scheme was utilized for density-based solver. Least square cell-based method was utilized for gradient and second-order upwind method was used for all other parameters on spatial discretization. The region on the airfoil was accepted as no-slip wall condition and the flow area was chosen as pressure far field condition with 5% of turbulent intensity and 0.196m of hydraulic diameter. Residuals for parameters are set to 10^{-8} convergence absolute criteria.

3.3. Validation

First of all, mesh independence study was performed for clean airfoil in order to obtain sensitive results from numerical solution. Four different element numbers (which were 60 000, 125 000, 250 000 and 500 000) were examined at angle of attack of α=10° and obtained lift coefficient value, C_L was compared with experimental results that presented by Istvan et al. (2018).

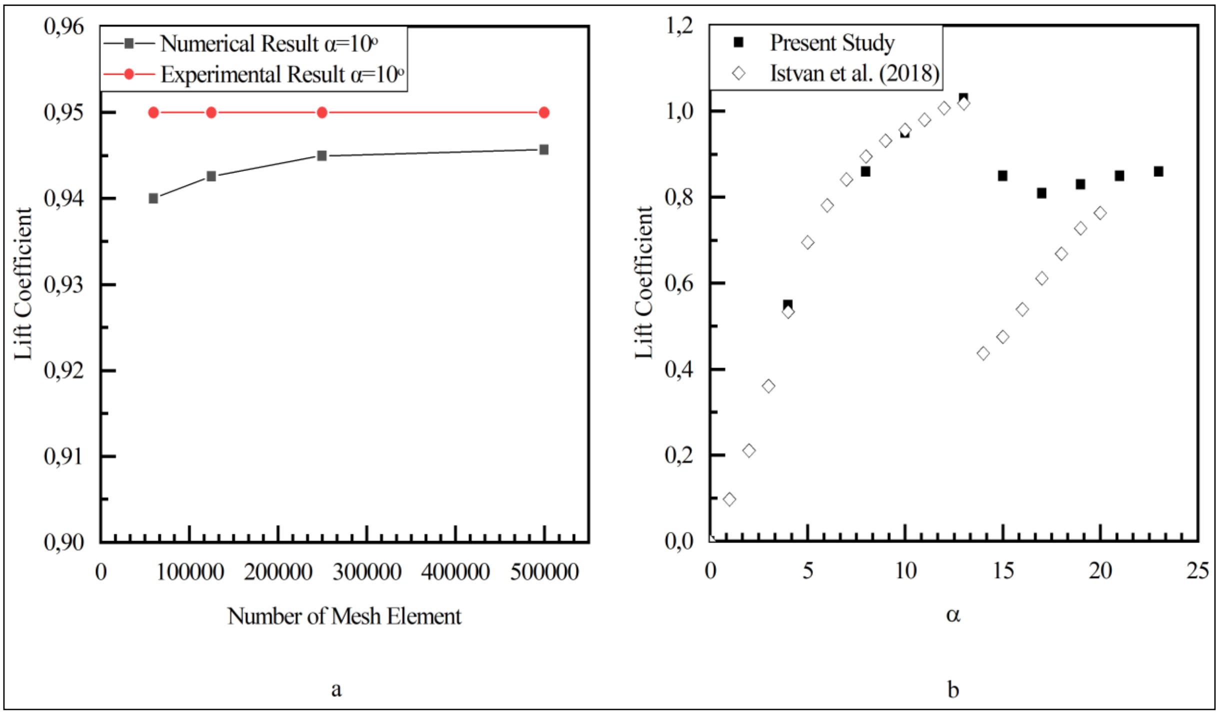

Figure 3.7. a) Mesh Independence Study and b) Comparison of Previous Experimental Results and Present Results

Figure 3.7a shows the variance of C_L with respect to the number of mesh element at angle of attack of α=10°. It is clearly seen that the number of mesh element has insignificant effect on lift coefficient after the number of mesh element is higher than 250 000. In the present study, the number of mesh element was chosen as 500 000 since C_L was nearly same with experimental result. After that mesh independence study, the values of C_L were compared with experimental results for different angles of attack for α=4°, α=8°, α=10° and α=13° at Reynolds number of $Re=1x10^5$. Figure 3.7b present the variation of lift coefficient with respect to angle of attack. It is observed that the value of C_L is good agreement with experimental result especially for α≤13°. On the other hand, it is obtained some difference in lift coefficient value for post- stall conditions. In addition to comparison of present numerical and previous experiment, - C_P values are also compared at α=8° and α=13° in the Figure 3.8. It is observed that the pressure coefficients of present study are well matched with the previous experiment.

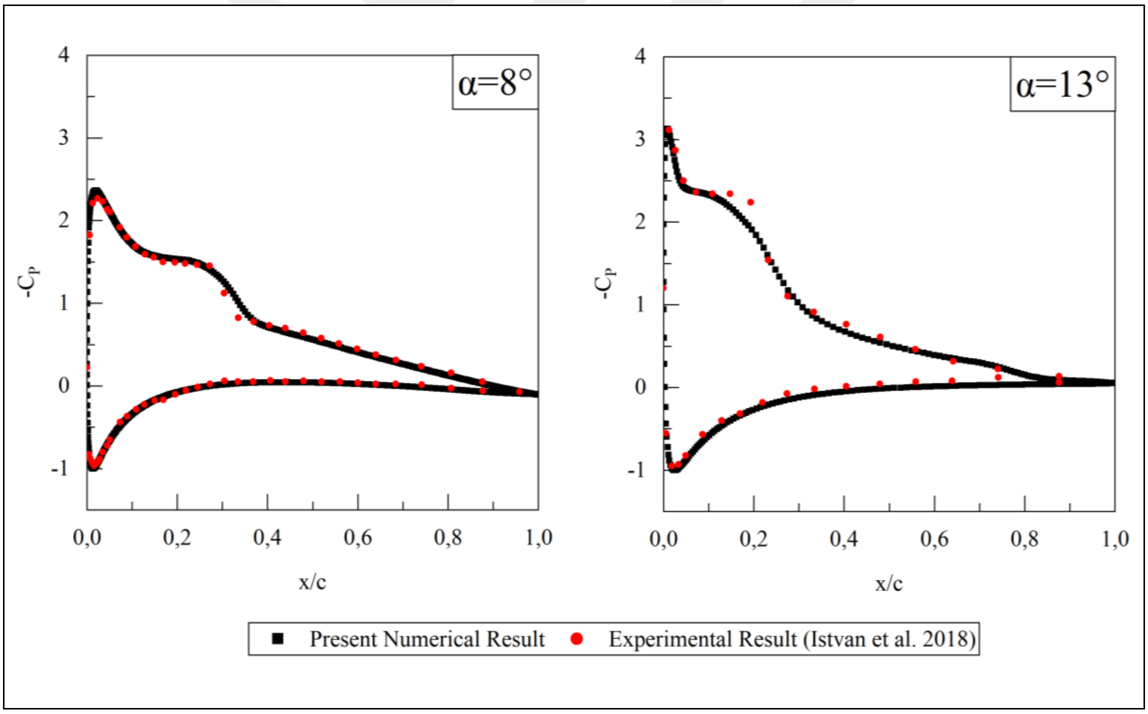

Figure 3.8. Comparison of Previous Experimental and Present Numerical Pressure Coefficient

3.4. Experimental Setup

In this section, experimental setup is presented. Experiments were carried out for M0 model in order to validation of the numerical solution. Experiments were performed in an open-suction type wind tunnel with the test section of 570mm x 570mm x 1000mm at University of Nigde Omer Halis Demir. General view of wind tunnel is presented in Figure 3.9. The inlet contraction ratio of the wind tunnel is 6.3:1. The airfoil is placed vertically in test section to eliminate the gravity. The turbulence intensity level is lower than 1%.

Figure 3.9. General View of Open-Suction Type Wind Tunnel

In Figure 3.10, NACA 0018 model is presented. The model is produced with PLA material by Raise 3D Pro 2 printer with the 200mm chord length and 450mm span length. The interface effect considered and the related set up is prepared in the test section. One of the end plate placed top surface of the section and the other one is located at bottom side. The airfoil shaped supports used to hold the end plates on top/bottom layer. The airfoil is centered between these end plates with a gap of 1.75mm. The net aerodynamic forces acting on the airfoil is clearly measured with the help of this method.

Figure 3.10. NACA 0018 Model

In order to measure drag and lift forces, ATI Gamma model six axis load cell is used. Measurements are taken at 500 Hz sampling frequency at averaging level of 50. Therefore, a total of 300 data samples were taken for each case and measurements were repeated two times to ensure a good time averaged data. The angle of attack was given by a rotary unit, controlled via computer. Force measurement equipment and rotary unit is presented in Figure 3.11.

Figure 3.11. Force Measurement System and Rotary Unit

Experiments were carried out at constant Reynolds number of Re=1x10^5 at angles of attack of $0° \leq \alpha \leq 21°$. The free stream velocity is measured by using ManoAir500 model type manometer and a pitot static tube showed in Figure 3.12. The calibration of the manometer is made before starting the experiments. The pressure and temperature values of the environment were measured as 85 kPa and 25 °C. Free-stream velocity was calculated by Engineering Equation Solver program and formulation was created based on constant Reynolds number given in Figure 3.13.

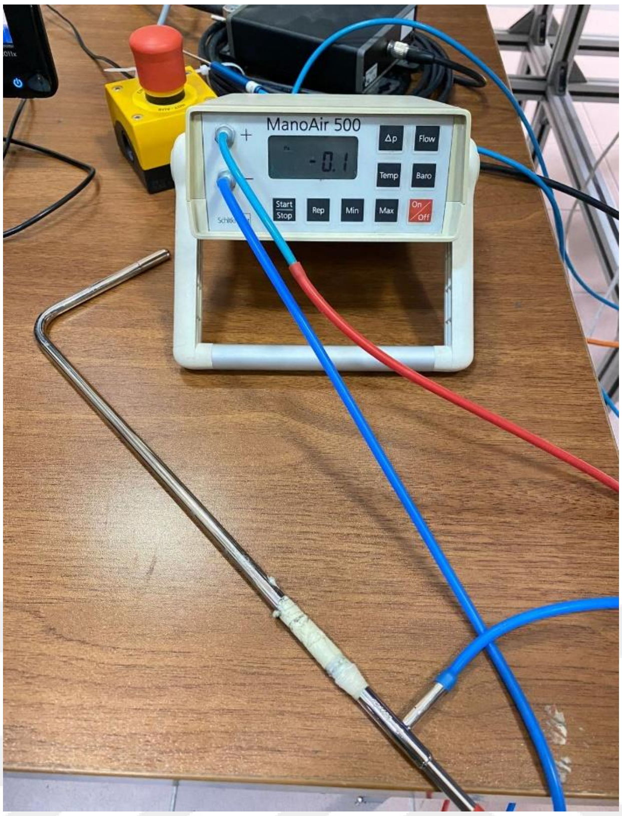

Figure 3.12. ManoAir500 Model Type Manometer and Pitot Static Tube

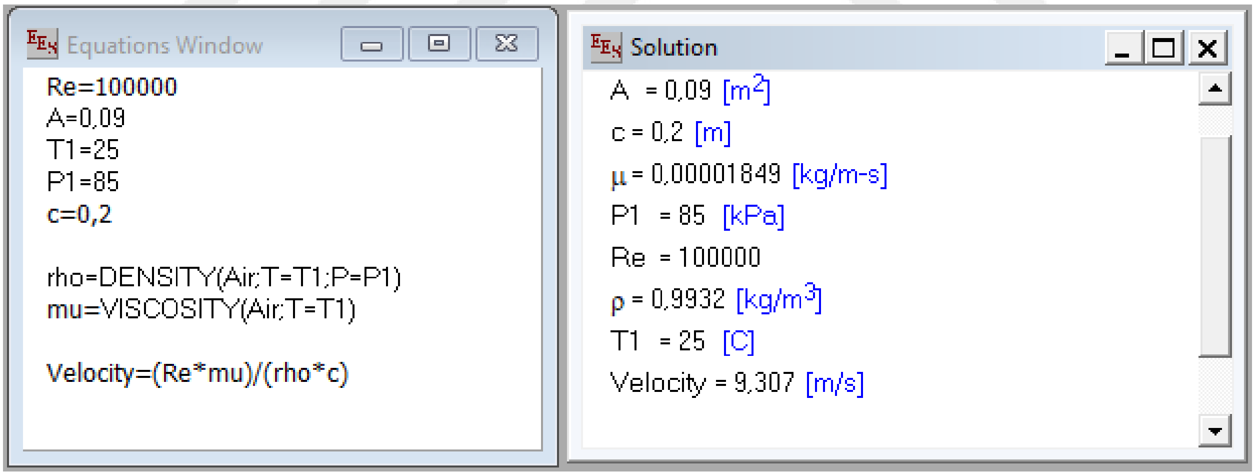

Figure 3.13. Determination of Free Stream Velocity in EES

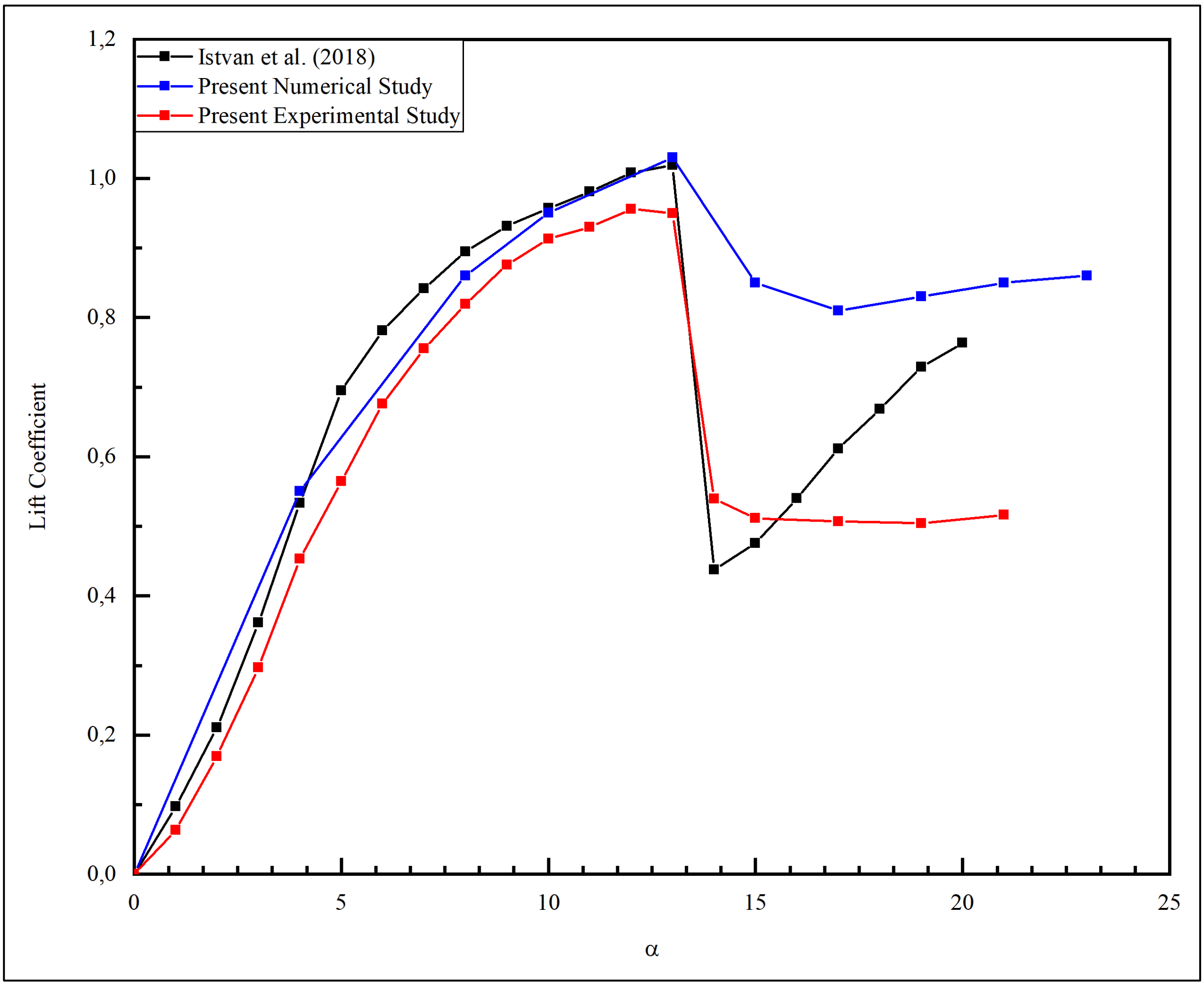

Figure 3.14 Variation of Mean Lift Coefficient at Various Angles of Attack

Figure 3.14 presents variation of mean lift coefficient for present numerical study, present experimental study and experimental study of Istvan et al. (2018) at various angles of attack. It is clearly seen that at pre-stall angles of attack α≤13°, mean lift coefficient values have similar trend until stall angle of α=13°. It is showed that the stall angle determined from present numerical study is same with the experimental studies.

4. RESULTS AND DISCUSSIONS

Firstly, numerical solution was performed for clean airfoil to constitute reference. Obtained results from clean airfoil were compared with different riblet configurations. In this section, the results were also evaluated in the five subchapter in order to compare parameters of riblet in detail.

In Figure 4.1 is given that the variance of lift coefficient of M0 smooth airfoil with the angle of attack. At angle of attack of α=0°, the lift coefficient is obtained as zero since airfoil geometry is symmetrical. On the other hand, the lift coefficient increases gradually with increasing angle of attack. The maximum value of lift coefficient of C_L=1.05 is reached at angle of attack of α=13°. The lift coefficient drops suddenly to C_L=0.85 at angle of attack of α=15° due to stall condition. It is obtained that the lift coefficient increases for α ≥ 17°

The variance of drag coefficient of M0 smooth airfoil with the angle of attack is presented in Figure 4.2. At angle of attack of α=0°, the drag coefficient is found as C_D=0.023. The increase in angle of attack causes to create more drag force by increasing in front sectional area of airfoil. At low angles of attack of α≤10°, drag coefficient is increased slowly while it is suddenly increased by 222% from α=13° to α=15° due to stall condition. Maximum drag is obtained as C_D=0.31 at the angle of attack of α=19°.

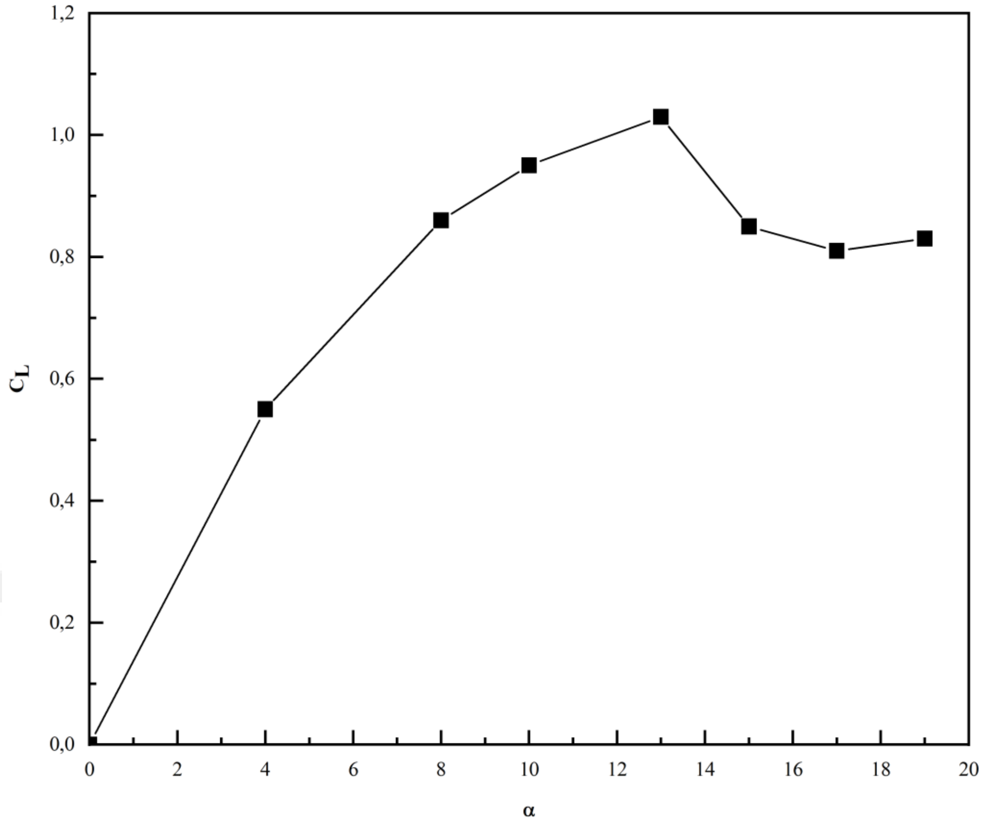

Figure 4.1. Variation of Lift Coefficient of M0 Smooth Airfoil with the Angles of Attack

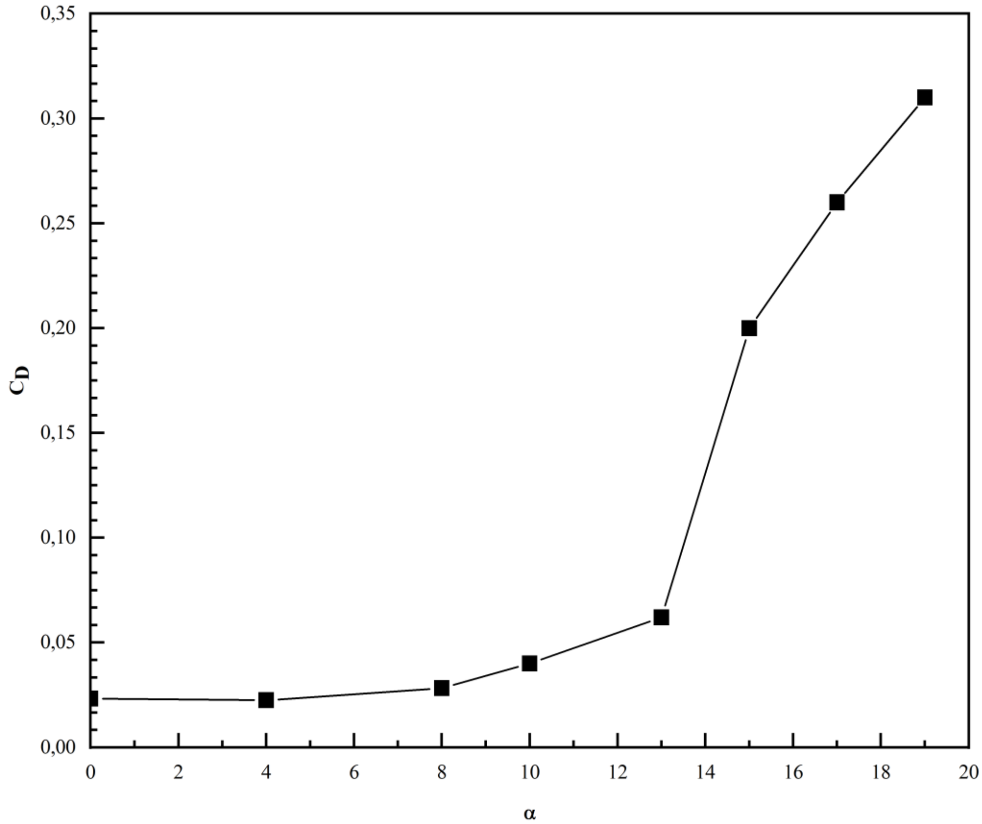

Figure 4.2. The Variation of Drag Coefficient of M0 Smooth Airfoil with the Angle of Attack

Streamline topology of M0 smooth airfoil is presented in Figure 4.3 for angle of attack in range of 0°≤α≤19°. At α=0°, formation of trailing edge separation which designated as TES in the figure, is observed on both suction and pressure surface. Increase in angle of attack prevents formation of trailing edge separation on pressure surface. At α=4°, flow separation occurs at x/c=0.46 and flow reattaches to surface at x/c=0.62. Laminar separation bubble occurs between those points. It is also clearly seen from figure, laminar separation bubble moves through leading edge until angle of attack of α=13° which is stall angle. At α=13°, LSB and TES is just before of the merging of bubbles, and TES is enlarged until α=13°. At α=15°, denoted by F shows a large recirculation region that LSB and TES are merged.

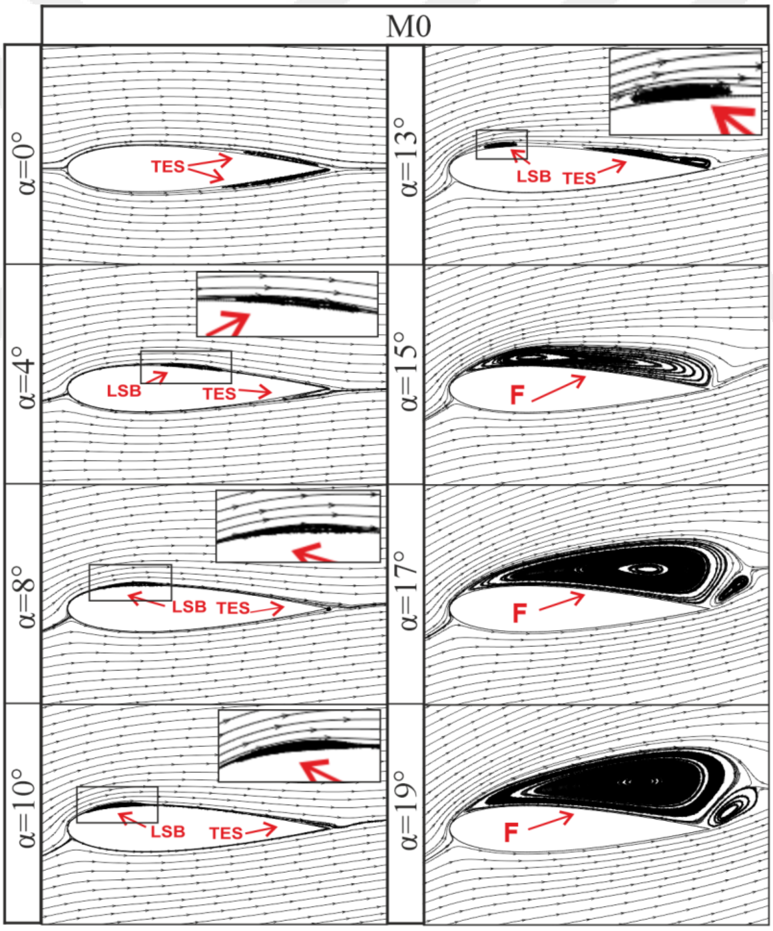

Figure 4.3. Streamline Topology of M0 Smooth Airfoil at Various Angles of Attack

Distributions of pressure coefficient are presented for α= 0°, 4°, 8°, 10°, 13°, 15°, 17° and 19° in Figure 4.4 in order to understand flow dynamics such as formation of the laminar separation bubble, separation, transition and reattachment points. In the Figure 4.4, hump of the curve on the suction surface of airfoil indicates the separation of the boundary layer caused by high adverse pressure gradient. The point where start hump indicate occurrence of flow separation, and the highest point of the hump indicates formation of transition. Finally, flow reattaches at the end of hump. At α=0°, distribution of pressure coefficient is symmetrical and trailing edge separation occurs on both pressure and suction surface of airfoil. The separation and reattachment points are found at x/c=0.46 and x/c=0.62 for α=4°, and x/c=0.061 and x/c=0.262 for α=10°, respectively. The points showed that increasing in the angle of attack causes formation of separation and reattachment, earlier. In addition, this situation leads to decrease in bubble size. Moreover, obtained results are compared with the experimental results. It is observed that the numerical pressure coefficients also matched with experimental study of Istvan et al. (2018) for pre-stall angles. It is clearly seen from Figure 4.4 that, $-C_P$ has highest value until stall angle of angle (α=13°). At post-stall angles of attack, pressure distributions decrease over upper surface of airfoil due to merging of LSB and TES. Formation of a large recirculation region causes stall and diminishment of performance.

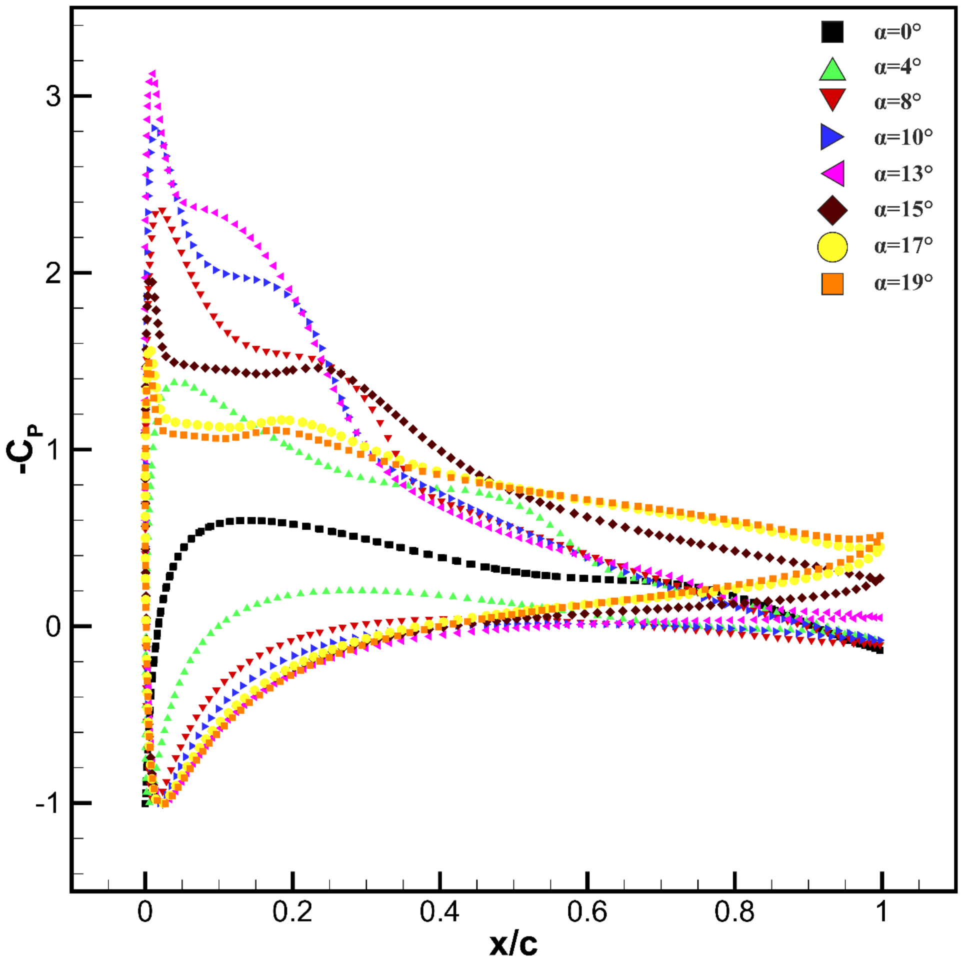

Figure 4.4. Pressure Coefficient of M0 Smooth Airfoil with Different the Angles of Attack

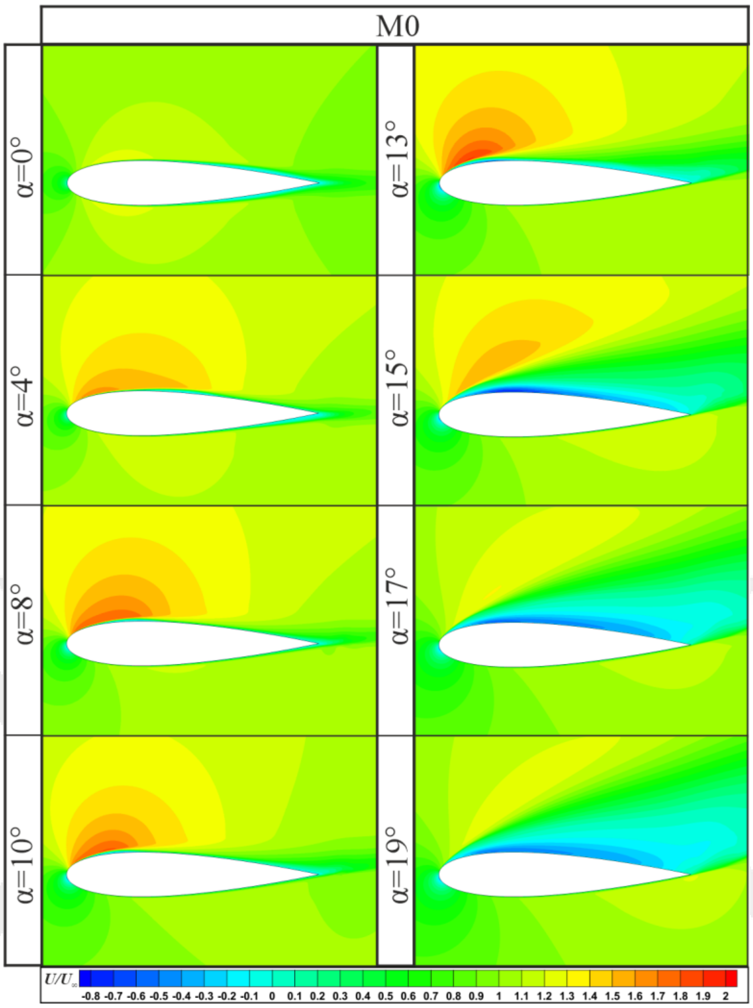

Figure 4.5. Stream-Wise Velocity Contours of M0 Smooth Airfoil with the Angles of Attack

Stream-wise velocity contours of M0 smooth airfoil are depicted in Figure 4.5 for angles of attack from 0° to 19°. The stream-wise velocity contours are useful to show velocity accelerations and decelerations over airfoil. A red region represents an acceleration in velocity due to increase in angle of attack and blue region demonstrates deceleration in velocity due to flow separations and formation bubbles. At pre-stall angle cases, from α=0° to α=13°, velocity increases on the leading edge of upper surface and it is seen with saturated red region. The most saturated red region (the highest velocity) is observed at α=13°. At α=0°, a light blue region occurs on the both upper and lower surface near the trailing edge of airfoil. With the increasing of angle of attack, velocity increases on the lower surface of airfoil and prevents formation of separation on the lower surface of airfoil. Due to the viscous force at high angles of attack, boundary layer separation and laminar separation bubble occur. At post-stall angles, laminar separation bubble and separation on trailing edge merge and creates a large re-circulation region which is depicted with blue region in figure. The increasing in angle of attack causes enlargement of re-circulation region.

4.1. Group I – Location of Riblet

In Group I, single and double riblets examined which are placed over upper surface of smooth airfoil M0. The riblet is placed at x/c=0.3, x/c=0.7 and both x/c=0.3 and 0.7 for M1, M2 and M3 models, respectively. The effect of the location is investigated and obtained results are compared with the smooth airfoil model (M0).

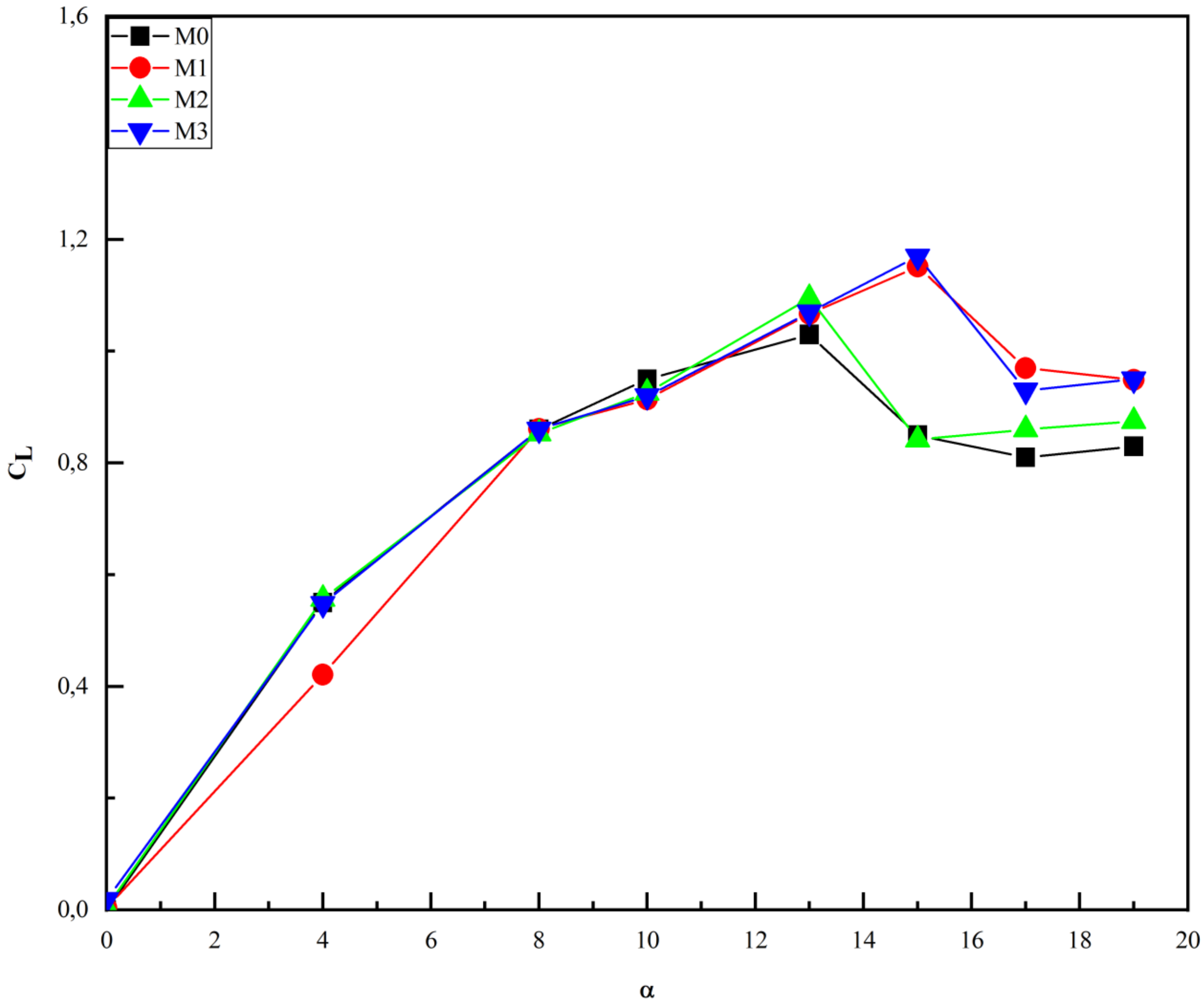

Figure 4.6. Variation of Lift Coefficient of Group I with the Angles of Attack

Figure 4.6 presents comparison of the lift coefficients for Group I at angles of attack of α=0°, 4°, 8°, 10°, 13°, 15°, 17° and 19°. In the lift coefficient graph, it is observed that the effect of riblet is insignificant up to angle of attack of α=13° except for M1 model. At α=4°, the value of lift coefficient for M1 model is approximately 23.5% lower than other models. The stall angle of M2 model is determined as α=13° and this value is same with the smooth airfoil. However, the M1 and M3 models delay the stall angle and stall occurs at α=15°. The M1 and M3 models cause an increase in lift coefficient. The value of maximum lift coefficient is obtained at α=15°

increased by 11% when compared to M0 model at α=13°

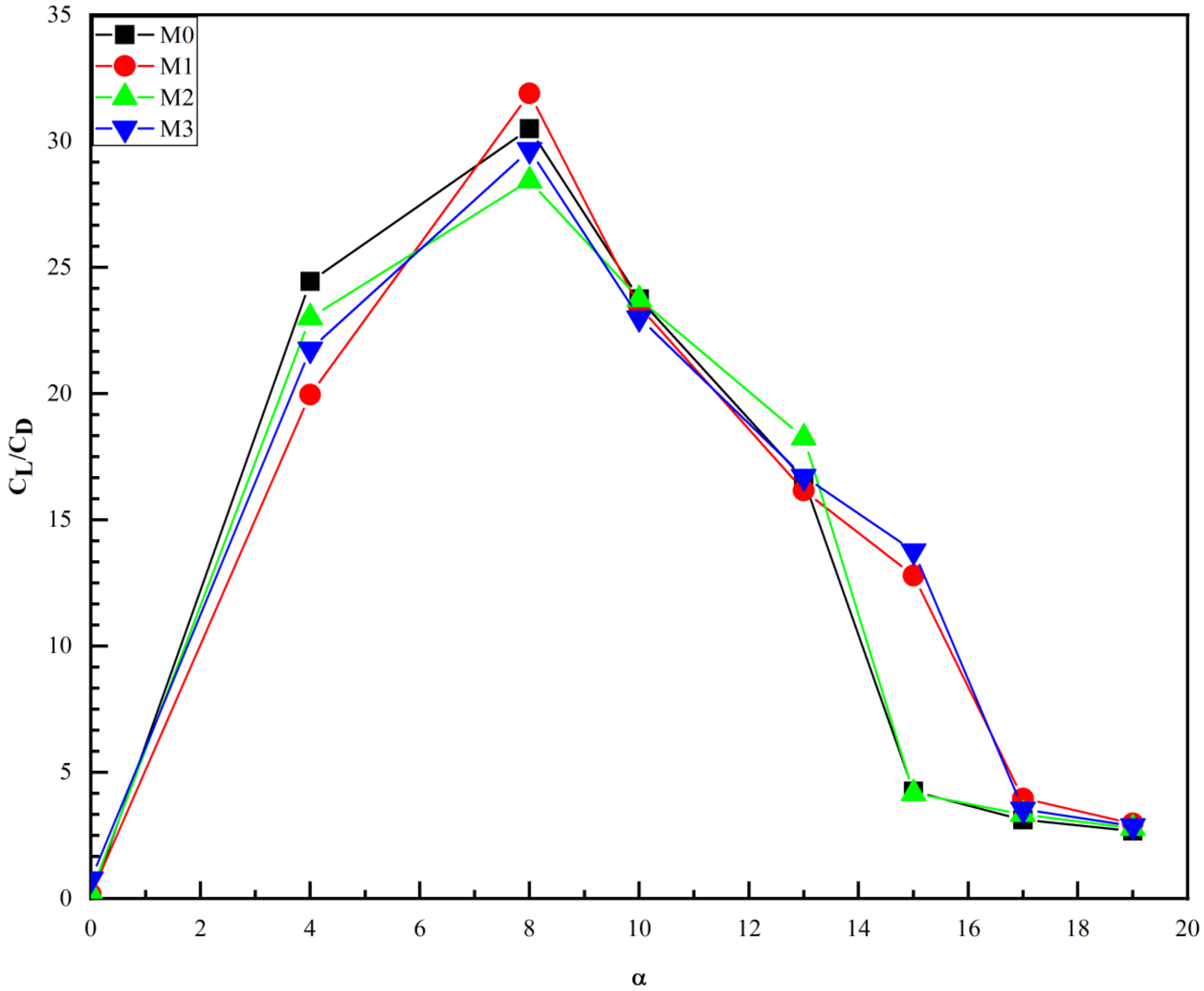

Figure 4.7. Variation of Lift-to-Drag Ratio of Group I with the Angles of Attack

Figure 4.7 shows lift-to-drag ratio at angles of attack of α=0°, 4°, 8°, 10°, 13°, 15°, 17° and 19°. It is observed that riblet adversely affects lift-to-drag ratios for all models in the range of 0°≤α≤4°, while the M0 model shows the highest value of 24.5 at α=4°.The highest lift-to-drag ratio is C_L/C_D=23.1 and about 6.6% when compared to M2 and M0 models. At α=8°, the M1 model depicts a sudden increase in the lift-to-drag ratio by 4% in comparison with M0 model. At α≥8°, the lift-to-drag ratios decrease with the increasing the angle of attack. However, the magnitude of the lift-to-drag ratio for the M0 and M2 models is 4.25 and 4.16 at α=15°, while it is obtained for M1 and M3 models as 12.8 and 13.8, respectively. The rate of maximum improvement in lift-to-drag ratio acquired at α=15° increased by 223% for M3 models.

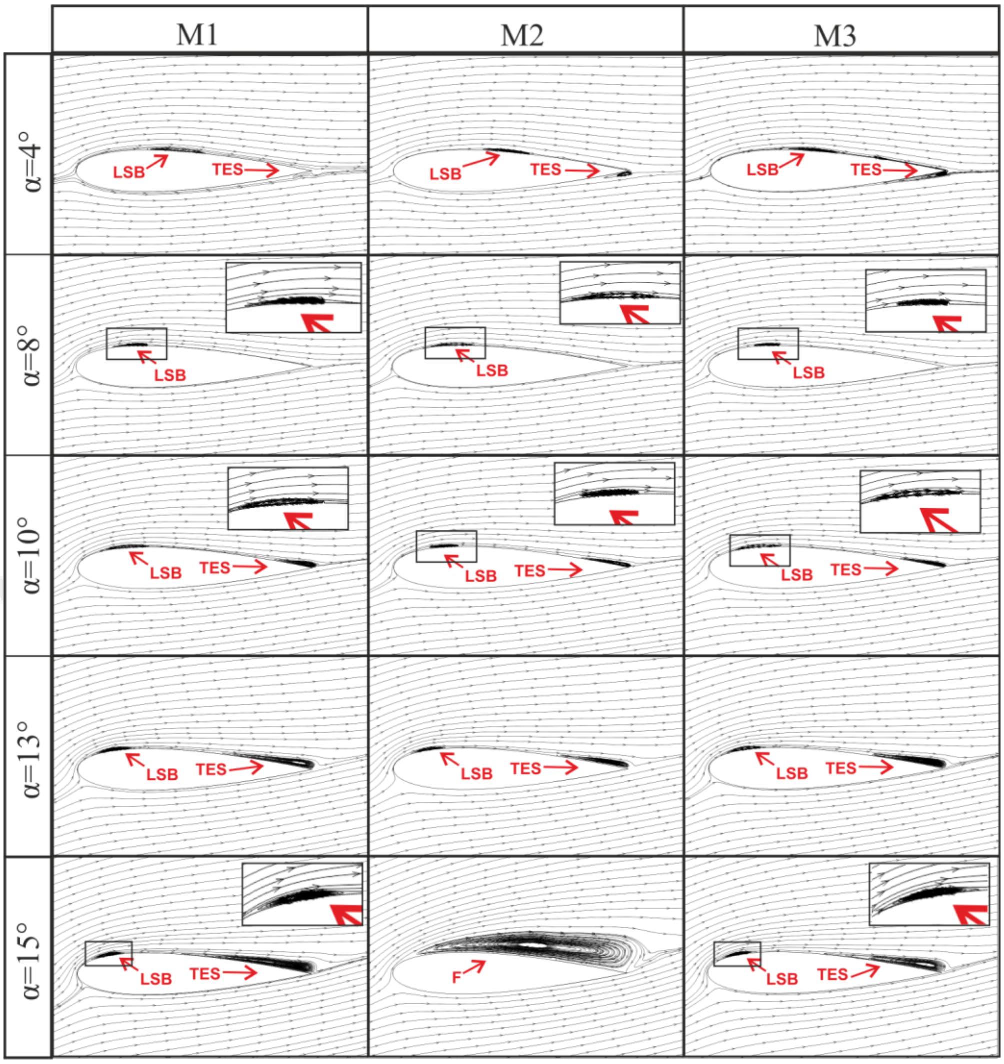

Figure 4.8. Streamline Topology of Group I at Various Angles of Attack

Figure 4.8 presents streamline topology in order to reveal flow structure of M1, M2 and M3 models at angle of attack of α=4°,8°,10°,13° and 15°. For M1, M2 and M3 models, at α=4°, it is observed that the presence of riblet have insignificant effect on the streamline topology when compared to smooth airfoil M0. Trailing edge separations are seen on the lower surface of models. The laminar separation occurs at x/c=0.3 for M1 and M3 models while it is observed at x/c=0.49 for M2 model. The size of bubble for M1 and M3 models is smaller than M2 model. When angle of attack increased to α=8°, TES disappears and LSB moves through leading edge for all models. On the other hand, the size of LSB decreases for M1 and M3 while it enlarges for M2. With the increasing angle of attack, LSB is suppressed and prevented to move toward leading edge by control elements. At α=13°, it is observed that located riblet at x/c=0.7 prevents moving of trailing edge separation for M2 and M3 models. Furthermore, M1 model has smaller bubble size in comparison with M0 model. Due to the suppression of LSB and TES, it is seen an increase in the lift coefficient for M1 and M3 at α=13°. As it is mentioned before in the Figure 4.6, M0 and M2 are stalled at α=13°. At α=15°, the M0 and M2 models have a large recirculation region due to the stall and caused to increase in drag coefficient while M1 and M3 models preserve their performance. It is observed that riblet located at the x/c=0.3 is dominant on the streamline topology. The size of LSB of M1 and M3 is smaller than smooth model of M0. Since merging of LSB and TES are prevented, stall is delayed. Obtained results indicate that the effect of located riblet at x/c=0.3 and at both x/c=0.3 and 0.7 are nearly same.

Figure 4.9 shows pressure distributions on M0, M1, M2 and M3 models at α= 0°, 4°, 8°, 10°, 13°, 15°, 17° and 19°. The pressure distribution shows insufficient performance at low angles of attack, but transition point moves from x/c=0,55 to 0,45 for M1 and M3 models at α=4° when compared to M0 model. The early transition causes early reattachment. For α<13°, early transition occurs for all models and the M2 model has insignificant effect on control of bubble location. The maximum decrease in the laminar separation bubble length of M3 is approximately 29% in the comparison with M0 at α=13°. At α=15°, located riblets on M1 and M3 increase the performance of airfoil, but $-C_P$ values of M0 and M2 decrease due to the stall. At high angles of attack α≥17°, pressure distribution over the models decrease due to large recirculation regions.

Stream-wise velocity contours are given in the Figure 4.10 for M1, M2 and M3 models at the angle of attack of α=4°,8°,10°,13° and 15°. At low angles of attack, α≤10, reverse flow occurs. With the increase in angle of attack, at α=13°, M0 and M2 models have a large re-circulation region due to deceleration in the stream-wise velocity. At α=15°, M1 and M3 models allow acceleration in velocity and diminishes the size of recirculation region when compared to the M0 model.

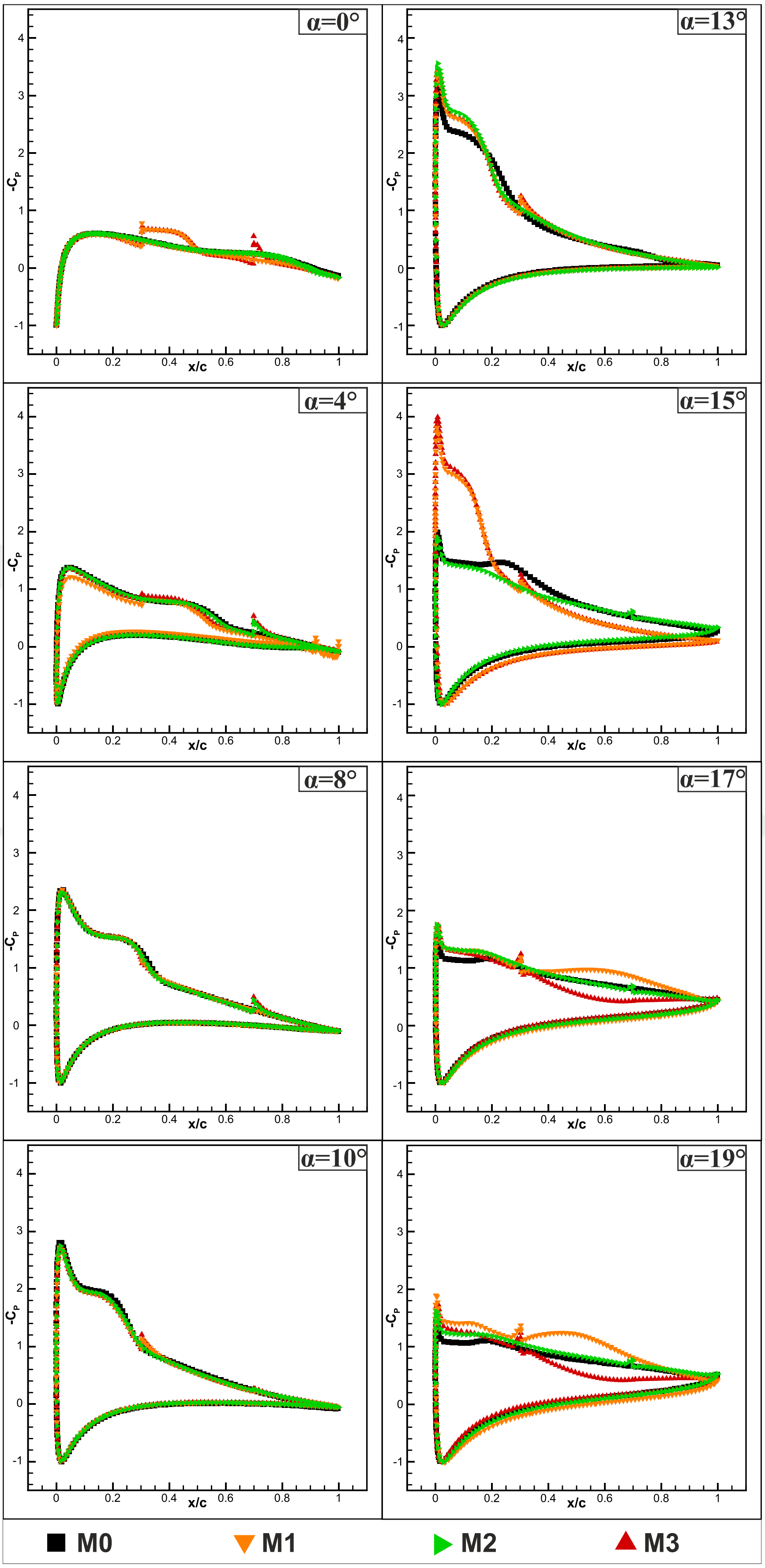

Figure 4.9. Pressure Coefficient of Group I at Various Angles of Attack

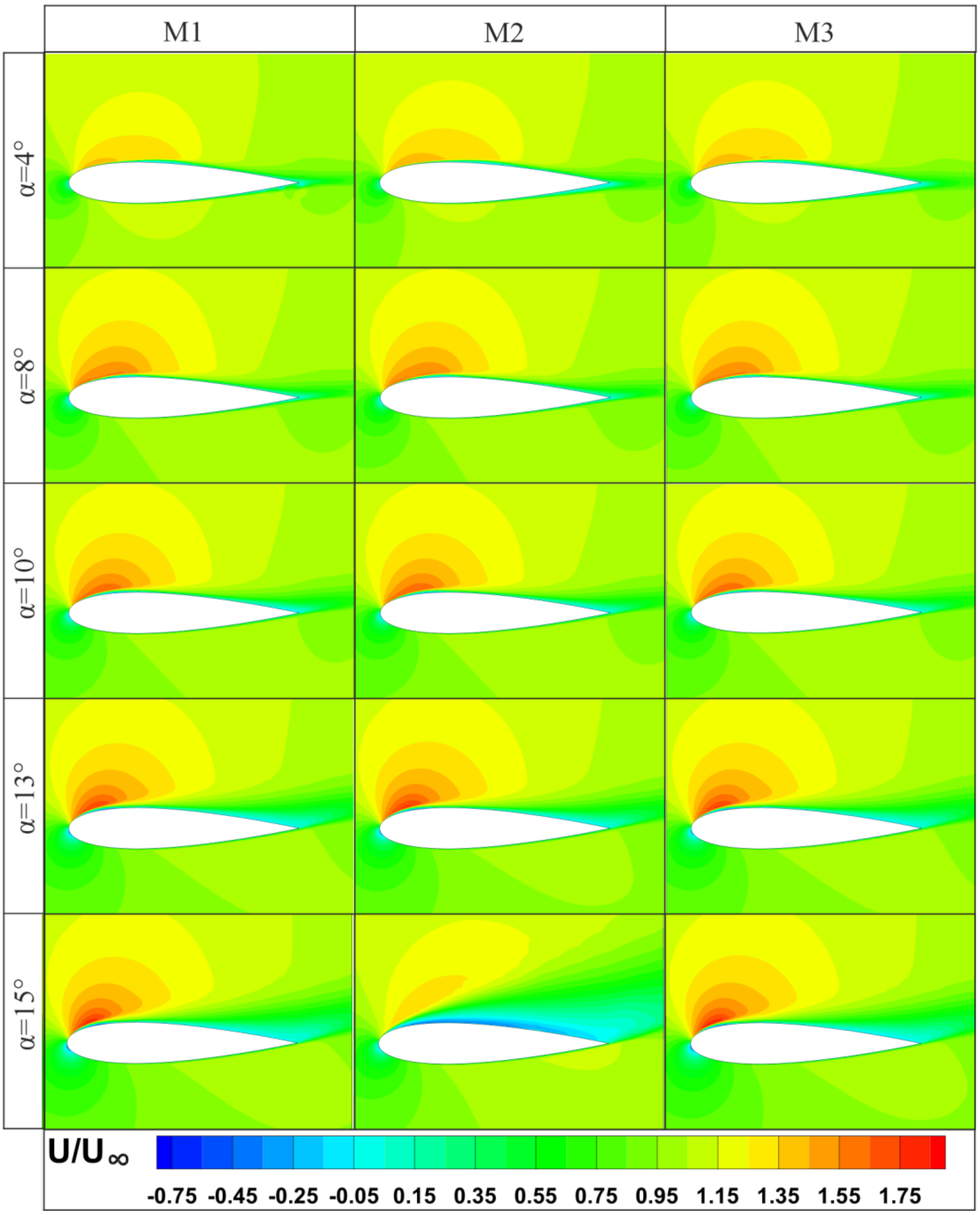

Figure 4.10. Stream-Wise Velocity Contours of Group I with the Angles of Attack

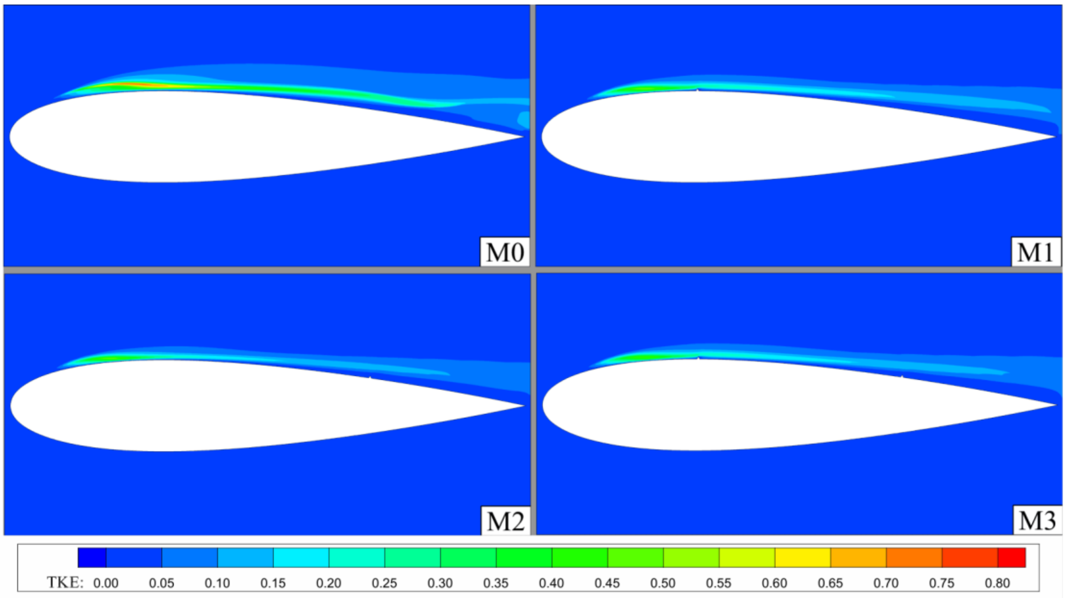

Figure 4.11. Turbulence Kinetic Energy of Group I at α=13°

Comparison of Turbulence Kinetic Energy for M0, M1, M2 and M3 at α=13° is given in the Figure 4.11. At stall angle of M0 model (α=13°), large fluctiatons intensify the turbulence kinetic energy and it effects performance of airfoil in a negative manner. It is observed that using of riblet decreases the maximum magnirude of the turbuleny kinetic energy in comparison with M0 model.

As a result of Group I, installing a single riblet at x/c=0.7 has insignificant affect. Obtained results show that M2 model behaves like M0 smooth airfoil model, no change in laminar separation bubble length and location. M1 and M3 models are more successful than M0 and M2 models on the stall control. M1 and M3 suppress LSB and prevent movement of TES toward the leading edge. The location between x/c=0.3 and x/c=0.7 is determined as important range. Gap ratio of riblet will discuss in the next section for that determined range.

4.2. Group II – Gap Ratio

In the previous section, the location of riblet was investigated to determine optimum model. It is obtained that M3 model had better performance when compared to other models. Because of that, in Group II, it will be focused on the gap ratio. The section, where is between x/c=0.3 and x/c=0.7 will be filled with riblet for each model.

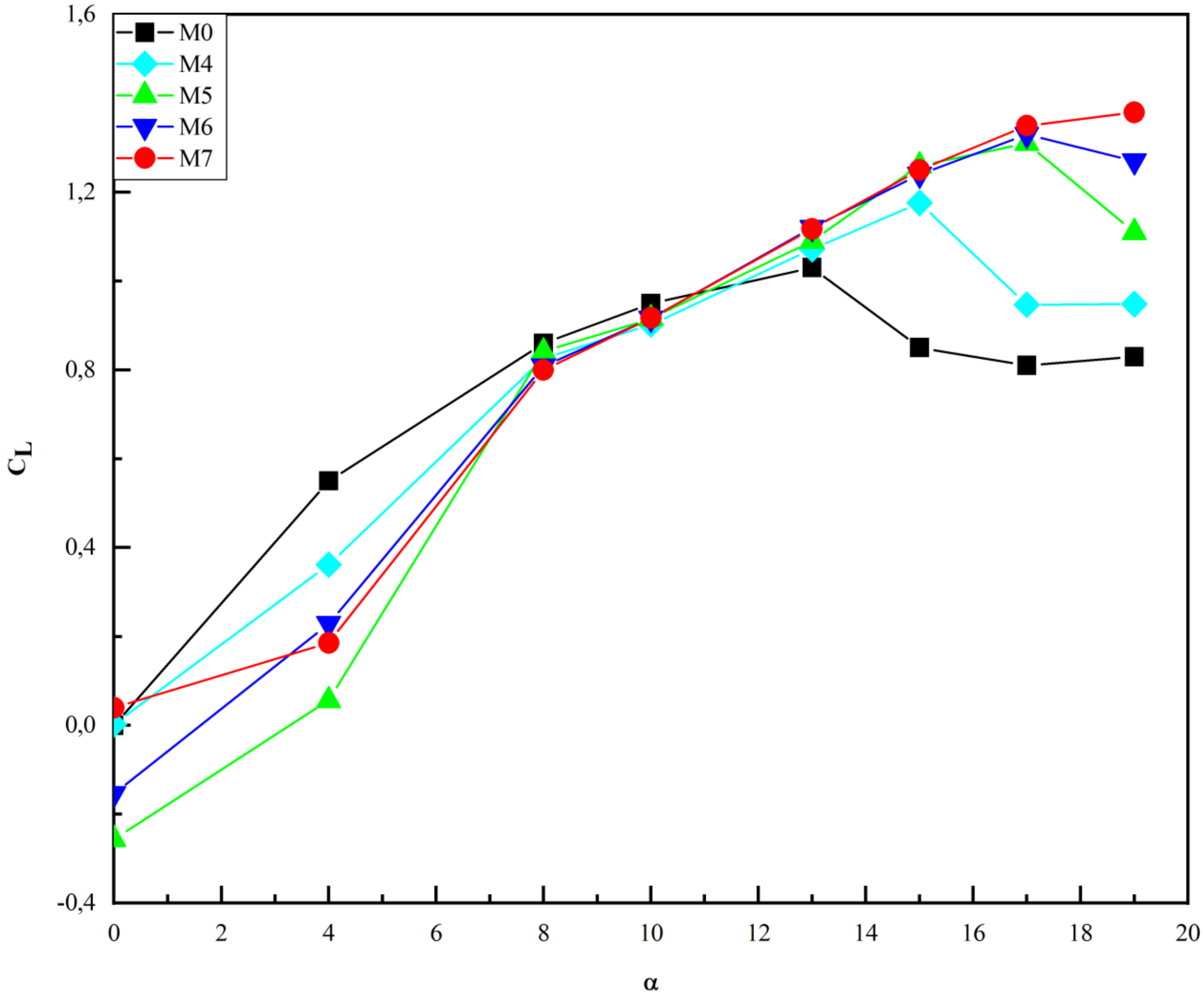

Figure 4.12. Variation of Lift Coefficient of Group II with the Angles of Attack

Lift coefficients of Group II at angles of attack of α=0°, 4°, 8°, 10°, 13°, 15°, 17° and 19° are presented in Figure 4.12. It is observed that the effect of riblet is insignificant up to angle of attack of α=13°. At α=0°, M5 and M6 models have negative lift coefficient value because of the higher pressure on the upper surface while the value of M4 and M7 is approxinately same with M0 model. At α=4°, M4, M5, M6 and M7 underperform compared to M0 model. M5 model has the lowest lift coefficient value and it decreases by 90% in comparison with M0 model. All models display similar trend at α=8° and α=10°, while the values of lift coefficient are slightly higher than the M0 model at α=13°. The value of lift coefficient of M6 and M7 model increase by 9% in contrast with M0 model at α=13°. The stall angle is determined as α=15° for M4 model while it is obtained as α=17° for the M5, and M6 models. On the other hand, stall angle is shifted to α=19° for M7 model. The M7 model shifts the stall angle by 6°, resulting in an increase in lift coefficient by 34% at α=19° when compared to M0 model at α=13°.

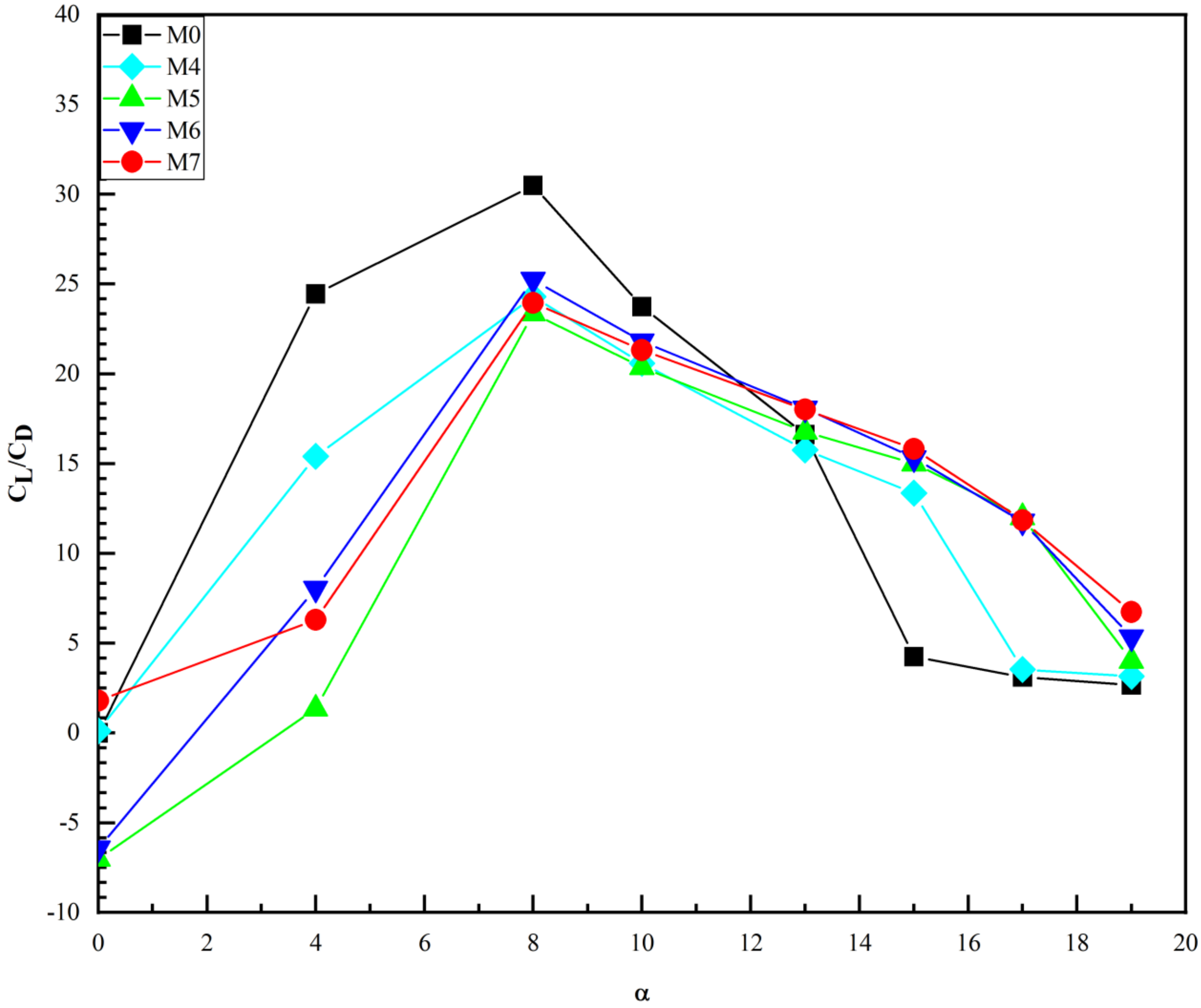

Figure 4.13. Variation of Lift-to-Drag Ratio of Group II with the Angles of Attack

Figure 4.13 presents lift-to-drag ratio of Group at angles of attack of α=0°, 4°, 8°, 10°, 13°, 15°, 17° and 19°. It is seen that, lift-to-drag ratio of riblet models is lower than M0 model at α≤10°. Lift-to-drag ratio of M5 model decreases by 95%. All models have approximately same value at α=8° and 10°. At α=13°, performance of models increases due to delaying stall except M0 model. The maximum lift-to-drag ratio is obtained for M7 model at α=15°. It is increased by 272% when compared to M0 model.

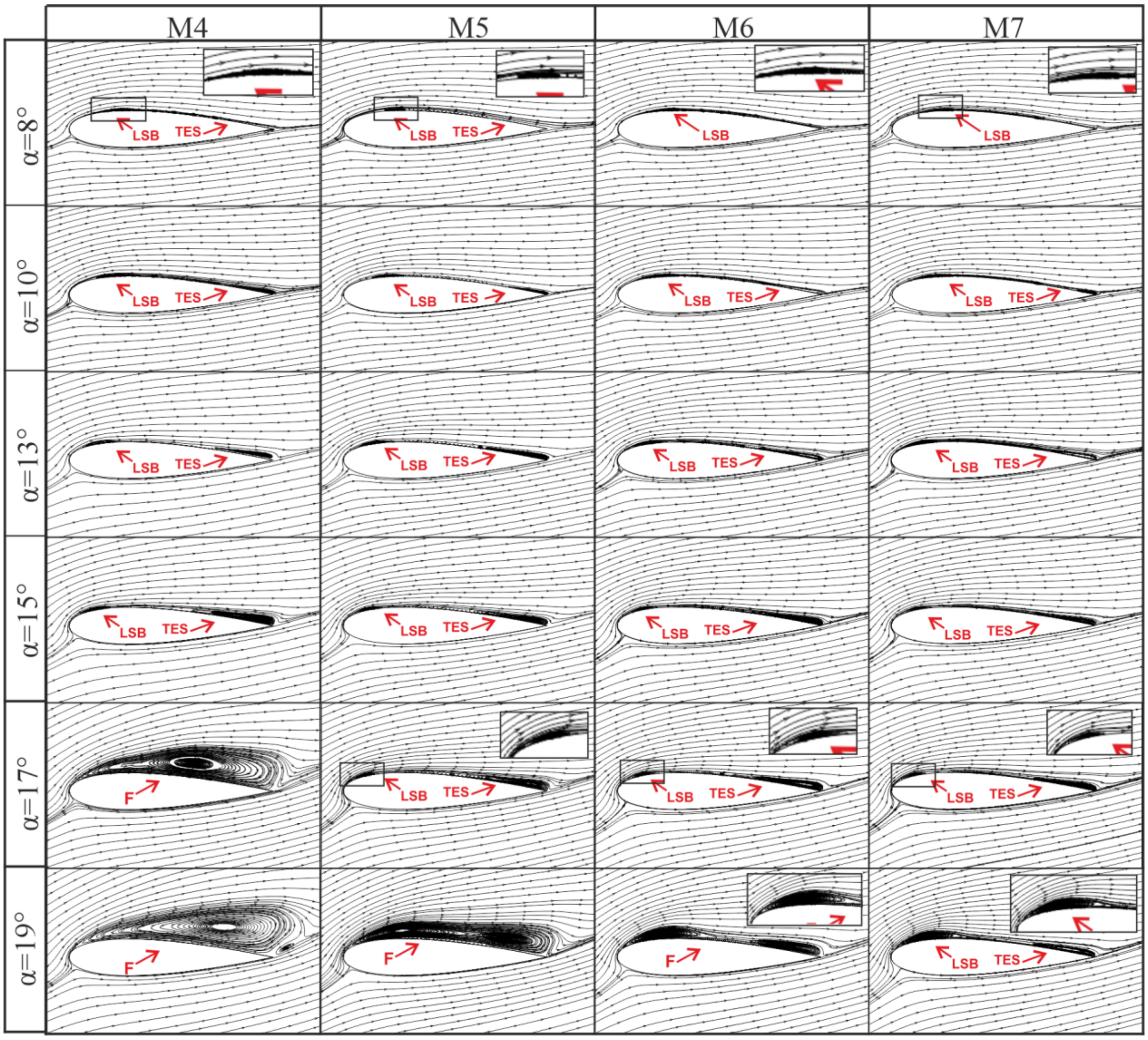

Figure 4.14. Streamline Topology of Group II at Various Angles of Attack

Figure 4.14 shows streamline topologies to show flow structure around M4, M5, M6 and M7 models. Angles of attack is selected as α =8°, 10°, 13°, 15°, 17° and 19°. As it is discussed in Figure 4.3, stall occurs at α=13° for M0 model and formation of large recirculation region over the upper surface of airfoil is observed at α=15°, α=17° and α=19°. When riblet surface is used, at α=10° and α=13°, the size of trailing edge separation region increases in comparison with angle of attack of α=8°. Moreover, laminar separation bubble moves toward to leading edge. It is observed that streamline topology is nearly same until the angle of attack α=15° for all models. At α=15°, M4 model has the largest TES size since the gap ratio (s/c=0.1) is high and separation fills the area between riblets. At α=17°, LSB and TES merges and creates a large recirculation region. Prove of that is also showed in the Figure 4.12 at α=17°, a large recirculation area occurs for M5 model due to formation of stall. M6 stalls at α=17° due to the enlargement of LSB and TES, and creates a recirculation region at α=19°. M7 model has the zero gap between riblet (s=0) and prevents merging of the LSB and TES. Figure 4.14 shows that decreasing the riblet gap ratio restricts the movement of TES and LSB, and shifts the stall angle.

Figure 4.15 is given to show pressure distribution at 0°≤α≤19° for M0, M4, M5, M6, and M7 models. At low angles of attack, using of riblet has insignificant effect on the pressure distribution around the airfoil. On the other hand, riblet remarkably affect with the increasing of the angle of attack. At α=8°, pressure distribution shows that formation of reattachment begin earlier for all models (x/c=0.3) when compared to the M0 model (x/c=0.38). Located riblet at x/c=0.3 causes formation of early transition. However, recirculation regions are observed between riblets for M4 model having high gap ratio. As seen from the figure, decrease in the $-C_P$ is seen due to the merging of LSB and TES at α=15°, α=17°, α=19° and α=19° for M0, M4, M5, and M6, respectively. The maximum decrease in the laminar separation bubble length is about 30% when comparing the M0 and M6 models at α=13°. The magnitude of $-C_P$ increases until α=19° for the M7 model since gap ratio of riblet is zero. Therefore, it prevents formation of recirculation region.

Stream-wise velocity contours are given in the Figure 4.16 to show velocity field over airfoil. Contours of M4, M5, M6 and M7 models is presented in the range of 8°≤α≤19°. As seen from the figure, stream-wise velocities decrease with the increase in angle of attack after the stall angles. At pre-stall angle cases, velocity increases on the leading edge of upper surface. For smooth airfoil M0 model, a large recirculation region occurs at α=15° due to the stall. The stream-wise velocity increases until stall angle of other models. M4 shows low velocity field at α=17° and α=19° and blue region depicts recirculation region while it is observed at α=19° for M5 and M6. For M7 model, the laminar separation bubble and trailing edge separation occurs separately at α=19° when compared to other models. Using of riblets over the airfoil suppress recirculation region especially for low gap ratio of riblet in comparison with smooth airfoil M0 model.

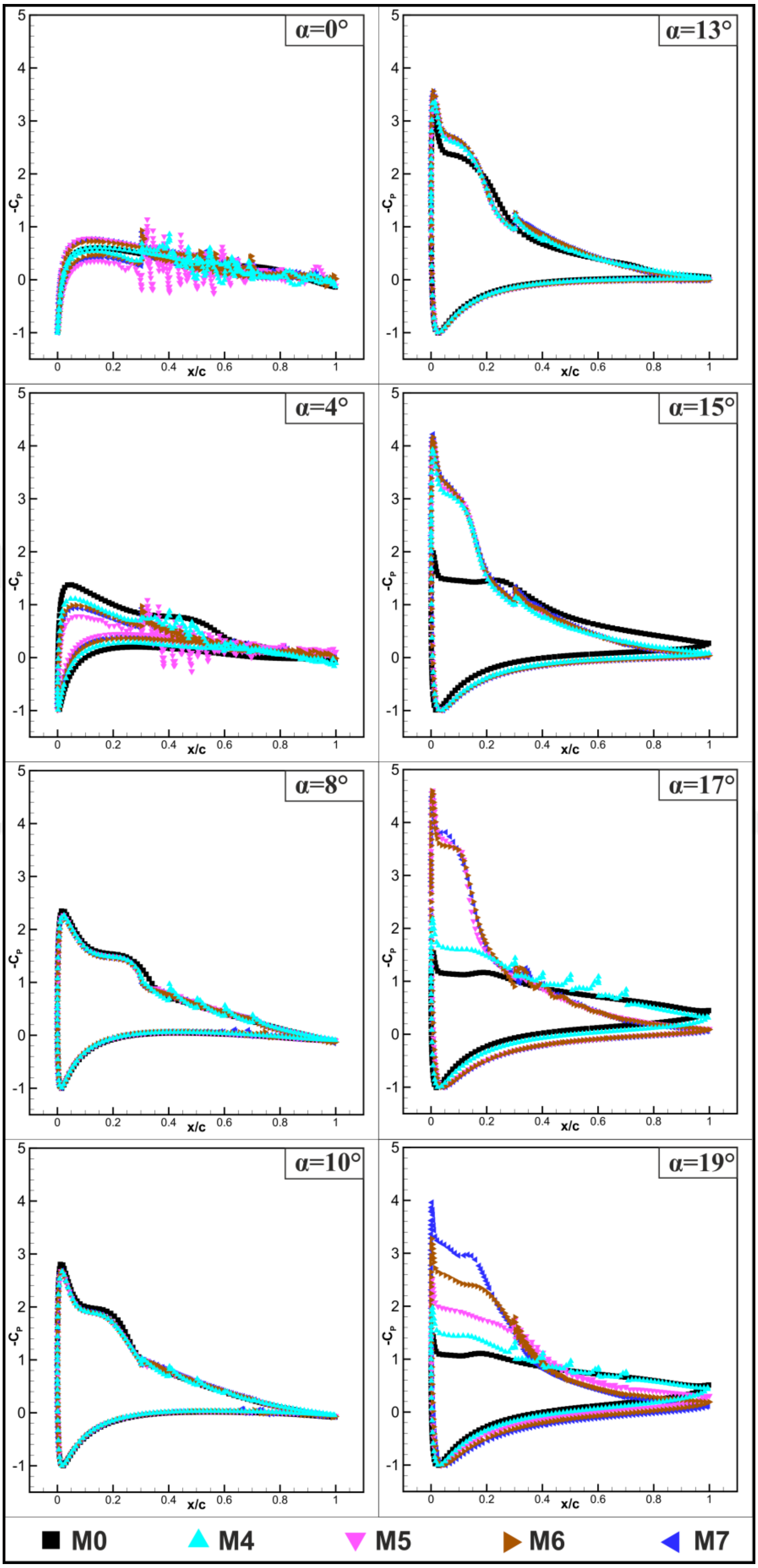

Figure 4.15. Pressure Coefficient of Group II at Various Angles of Attack

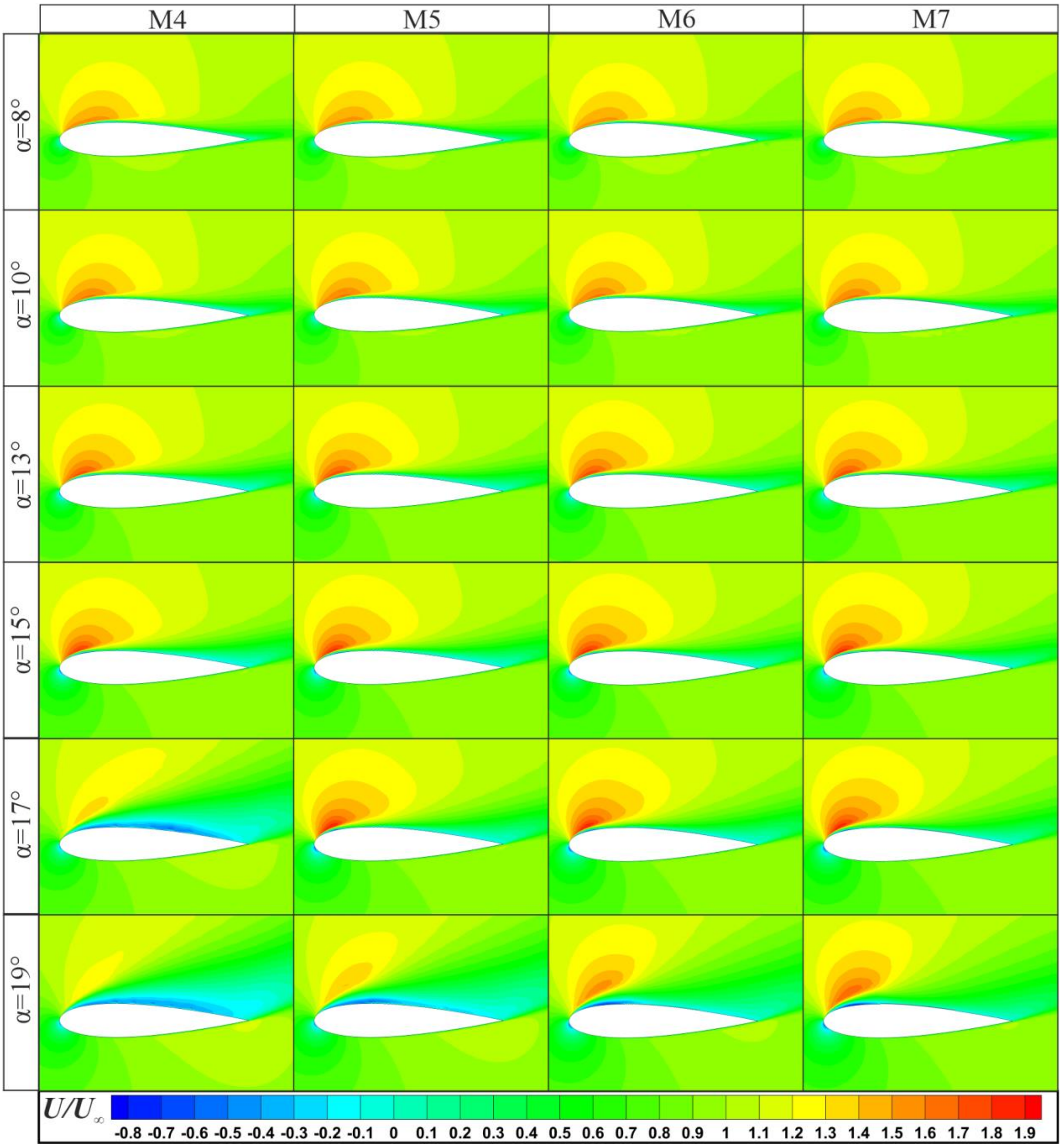

Figure 4.16. Stream-Wise Velocity Contours of Group II with the Angles of Attack

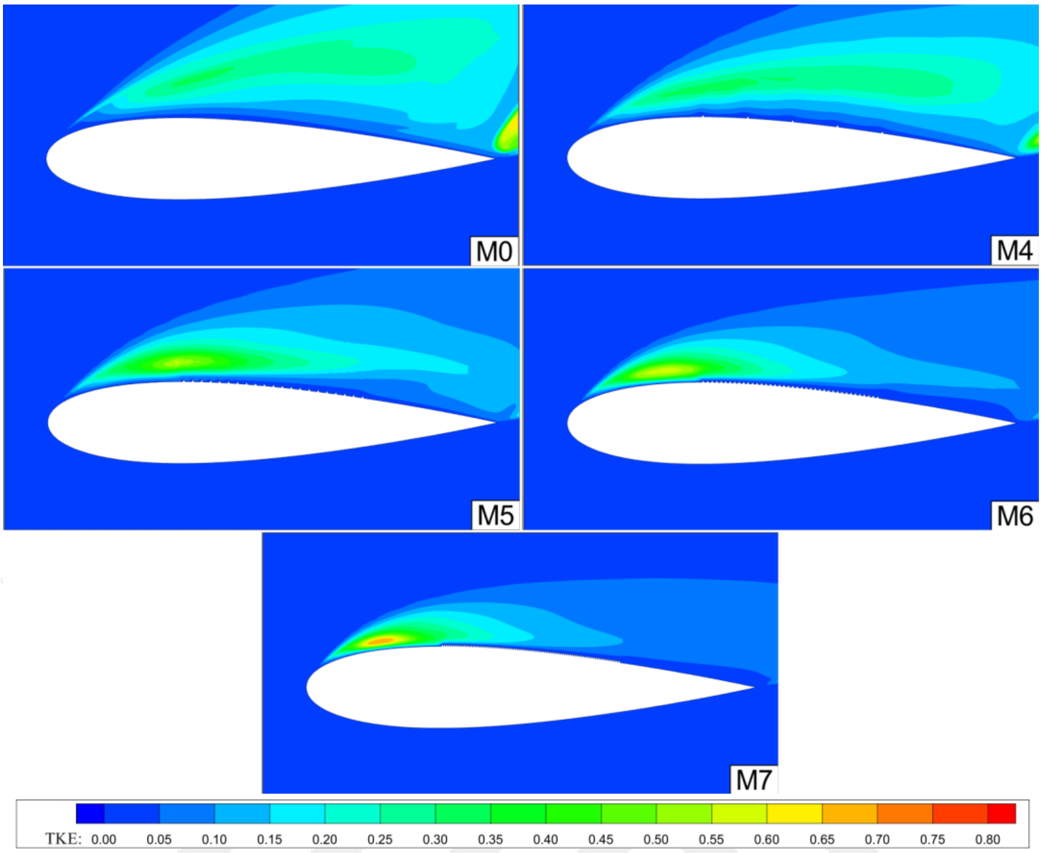

Figure 4.17. Turbulence Kinetic Energy of Group II at α=19°

Comparison of Turbulence Kinetic Energy for M0, M4, M5, M6 and M7 at α=19° is given in the Figure 4.17. Large fluctuation and low values of turbulence kinetic energy are seen on the on the M0, M4 and M5 models. For all models, stall occurs at the angle of attack of α=19° except M7 models. Highest value of turbulence kinetic energy is obtained on the upper surface of M7 model.

Group II shows that increasing riblet number in the region 0.3<x/c<0.7, shows a good performance due to the delaying of stall. Also flow control is achieved as a result of decreasing bubble size. The high gap ratio model M4 stalls at α=15° while zero gap ratio model M7 stalled at α=19°. In the next group, the size of riblet region on the model will be discussed.

4.3. Group III – The Size of Riblet Region

In Group 3, the effect of the gap ratio is determined and riblets are located at chord wise section in the range of 0.3 to 0.7. In this section, two models, which are M8 and M9, are examined. The riblets are located at $0.3<x/c<0.5$ and $0.1<x/c<0.7$ for M8 and M9, respectively. The obtained results are also compared to M0 and M7 models.

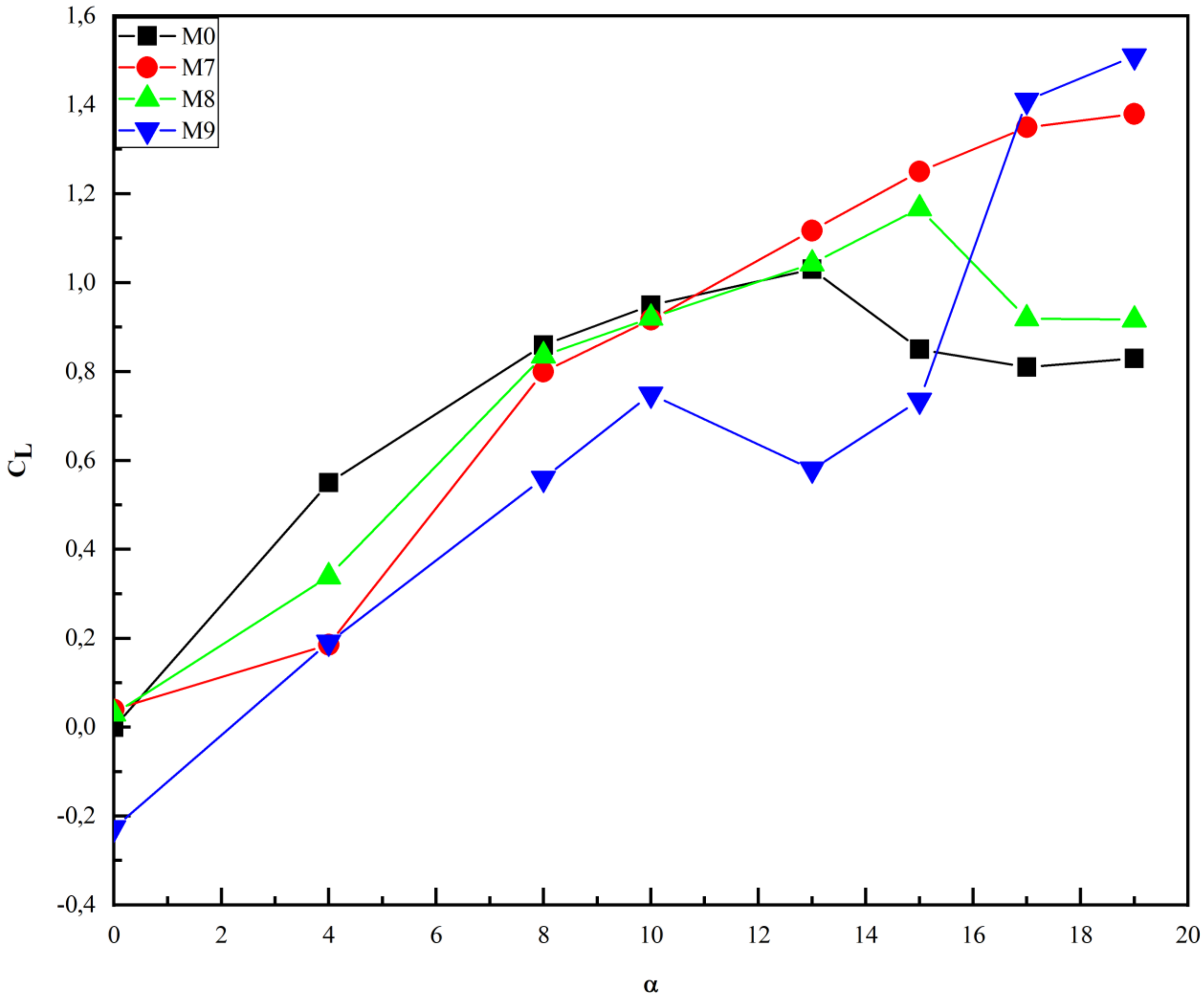

Figure 4.18. Variation of Lift Coefficient of Group III with the Angles of Attack

Lift coefficient of M0, M7, M8 and M9 at α= 0°, 4°, 8°, 10°, 13°, 15°, 17° and 19° is given in Figure 4.18. At lower angles of attack in the range of 4°≤α≤10°, all models perform lower value when compared to M0 model. M9 model display negative lift coefficient at α=0° since riblet causes higher pressure on upper surface than lower surface of the airfoil while M7 and M8 model lead to increase lift coefficient in comparison with M0 model. The M7 and M8 models have nearly same lift coefficient value at α=8° and α=10°. The M9 model stalls at α=10°. At α=15°, M8 stalls while the lift coefficient of M9 increases.

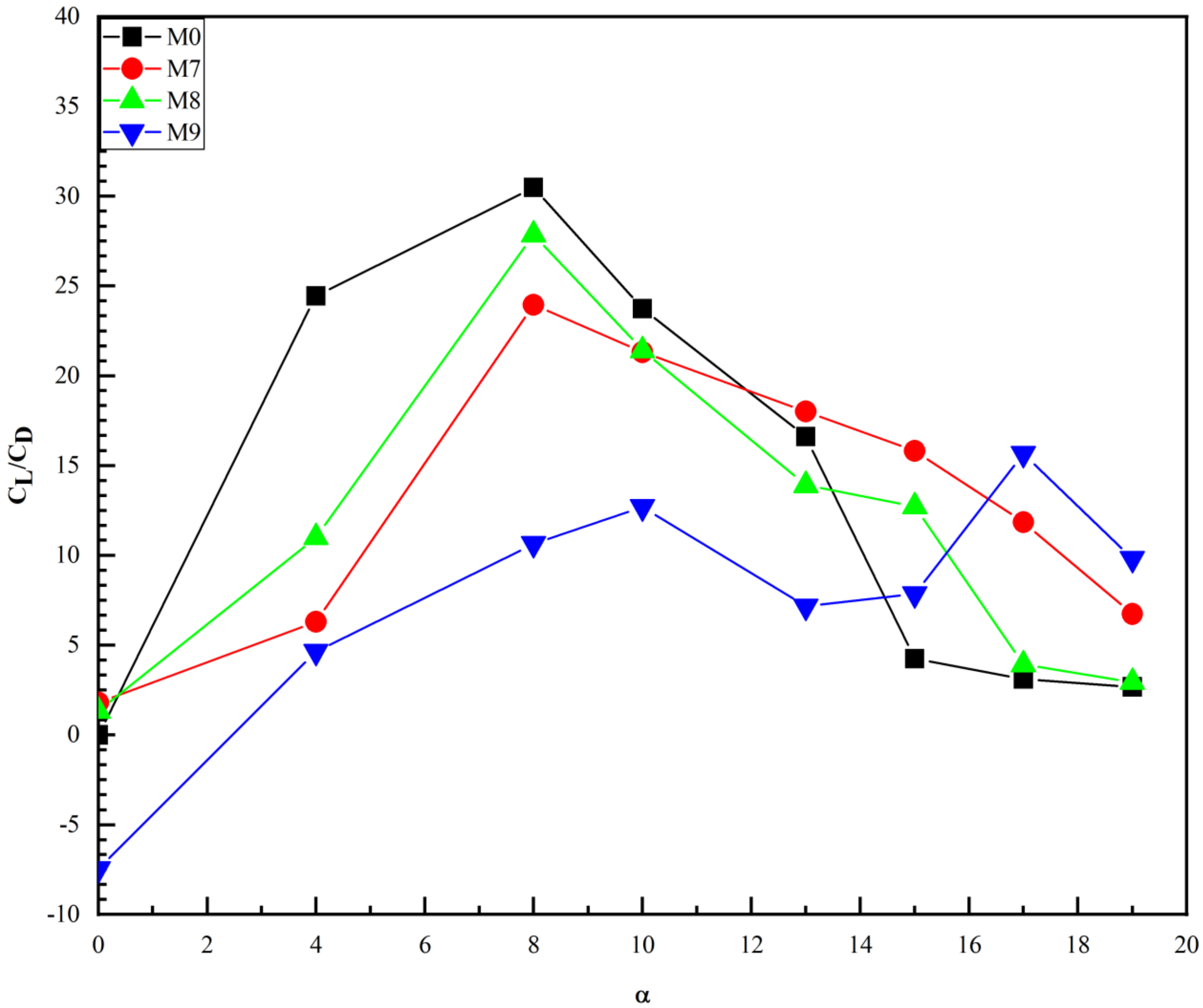

Figure 4.19. Variation of Lift-to-Drag Ratio of Group III with the Angles of Attack

Figure 4.19 shows lift-to-drag ratio of M0, M7, M8 and M9 at α=0°, 4°, 8°, 10°, 13°, 15°, 17° and 19°. Since the number of riblet on M9 model is more than other models, it causes high drag force and negative lift force at α=0°. With the increasing of the angle of attack, lift-to-drag ratio of models increase. At α=8°, lift-to-drag ratio decreases for all models. The M8 model have better lift-to-drag ratio than M7 model at α≤8°. Up to α=13°, the M9 model adversely affect the lift-to-drag ratio when compared to the M0 model. On the other hand, M8 model exhibits nearly same trend with the M0 model. At α=15°, increase in lift-to-drag ratio is obtained about 200% between M8 and M0 models. In the post-stall cases, the M7 model showed the best performance, in Group III.

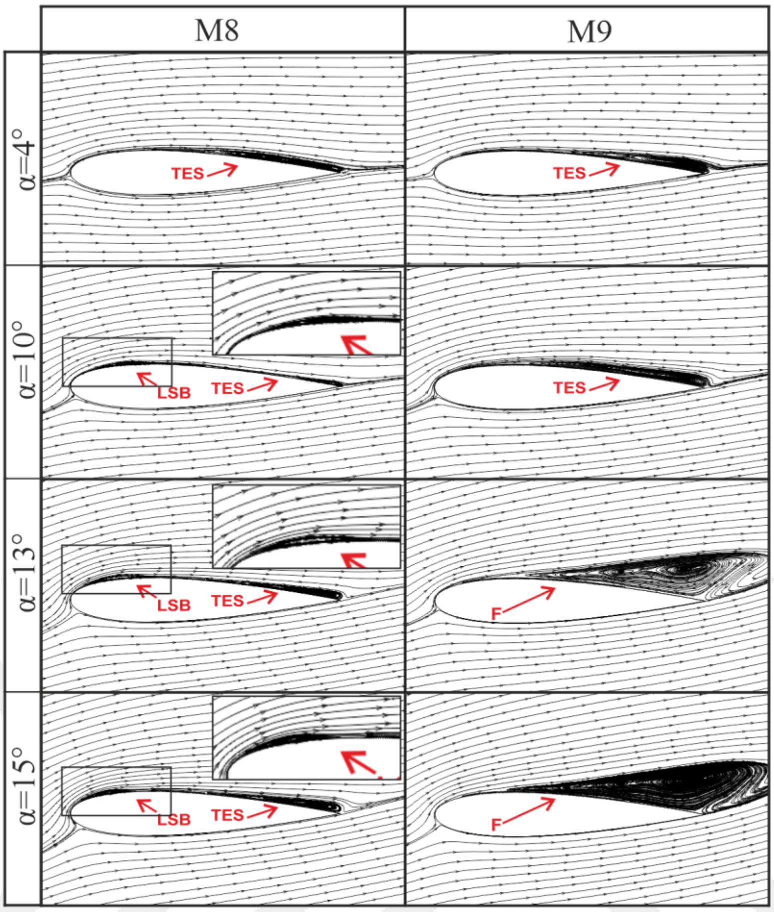

Figure 4.20. Streamline Topology of Group III at Various Angles of Attack

Streamline topology of Group III is given in Figure 4.20 for M8 and M9 at the angles of attack of α=4°, 10°, 13° and 15°. At α=4°, only trailing edge separation occurs for M8 and M9 models when compared to M0 model. At α=10°, laminar separation bubble occurs and TES shrinks for the M8 model while the size of TES enlarges for the M9 model. At α=13°, LSB and TES move through leading edge for the M8 models, and a large recirculation region is observed for M9 model. The M8 model causes early re-attachment. The point of re-attachment is x/c=0.3 and 0.25 at angle of attack of α=13° and α=15°, respectively. Early re-attachment causes decrease in bubble size. The maximum decrease in the laminar separation bubble length is observed for M8 model and that is approximately 21% in the comparison of M0 model at α=8°.

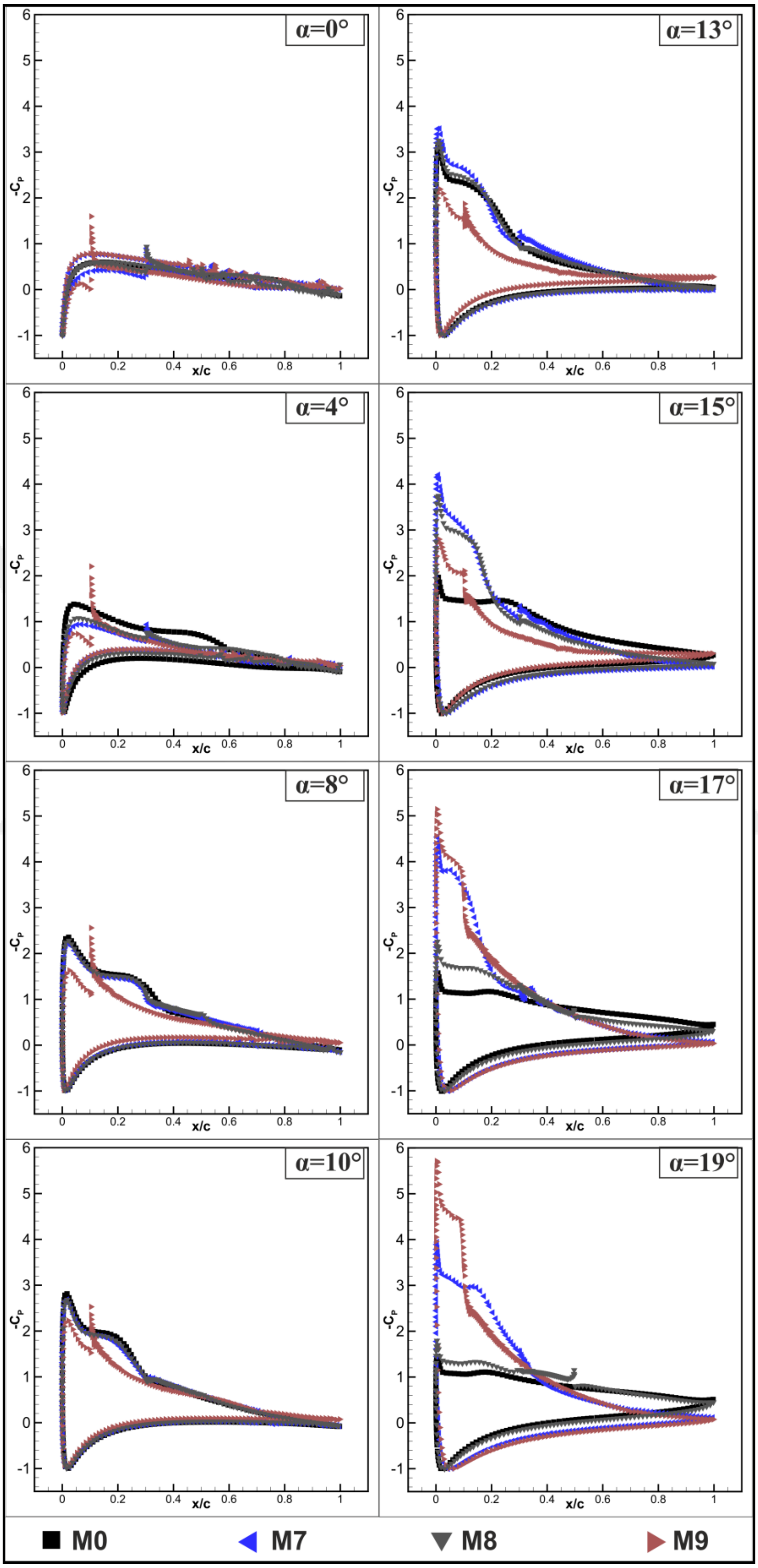

Figure 4.21. Pressure Coefficient of Group III at various Angles of Attack

Pressure distribution of M0, M7, M8 and M9 in the angles of attack 0°≤α≤19° is shown in Figure 4.21. It is clearly seen that riblet surface causes early transition and reattachment at α=8°. Models M7 and M8 have a good capability to control laminar separation bubble length due to early transition. M9 model causes early separation due to wide riblet region. M8 model which has narrow riblet region have better $-C_P$ performance than M9 model since the delaying separation leads to increase in $-C_P$ performance until α=15°. After that angle of attack, LSB and TES merge and performance of M8 decreases. Only M7 model controls the flow and it effective up to α=19°.

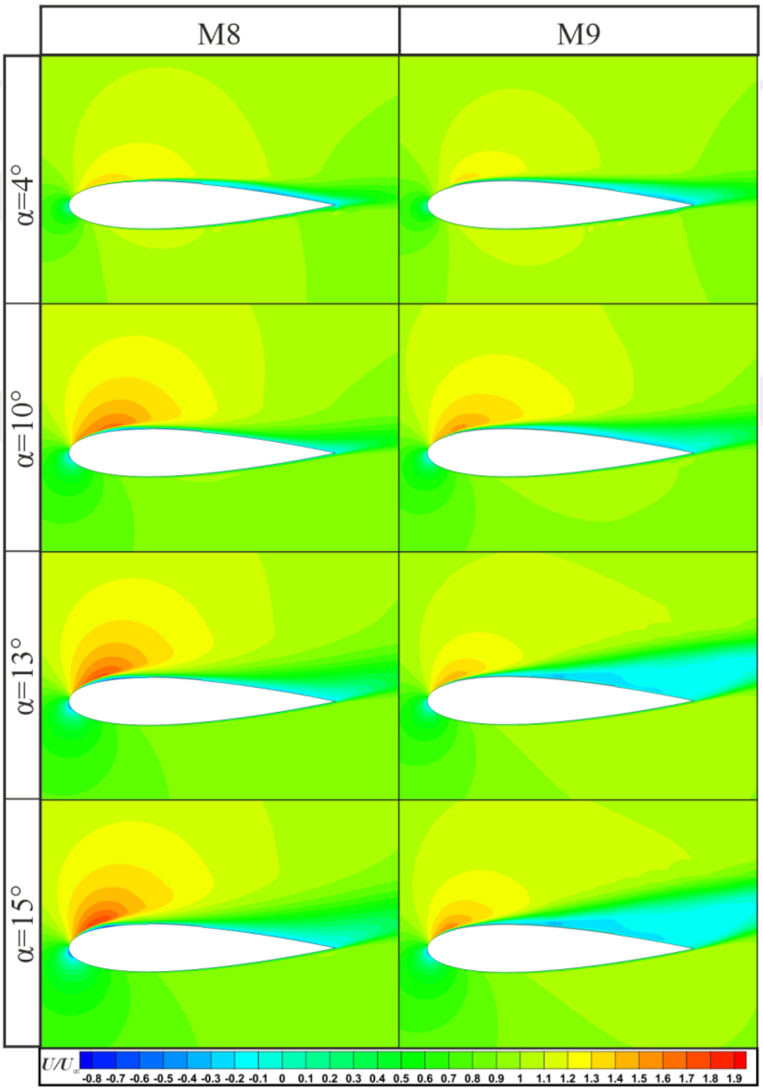

Figure 4.22. Stream-Wise Velocity Contours of Group III with the Angles of Attack

Stream-wise velocity contours are presented in the Figure 4.22 in order to show velocity field over airfoil. The stream-wise contours depict the M8 and M9 at the angles of attack of α=4°, 10°, 13° and 15°. As seen from the Figure 4.22, U/U_∞ increases on the leading edge of airfoil suction surface. M8 and M9 model have deceleration in velocity at the trailing edge of airfoil and causes formation of trailing edge separation. Increase in angle of attack causes acceleration in the flow for M8 model while re-circulation region is observed for M9 model. At α=13° and α=15°, large blue contours depicts re-circulation region.

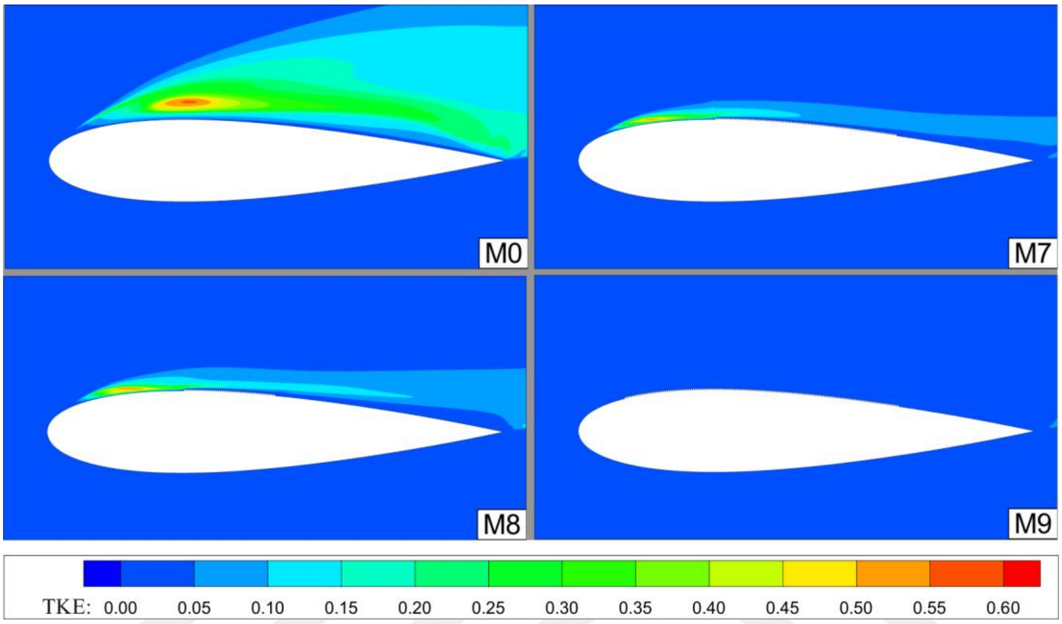

Figure 4.23. Turbulence Kinetic Energy of Group III at α=15°

Figure 4.23 shows comparison of turbulent kinetic energy for M0, M7, M8 and M9 model at α=15°. As it is shown before in Figure 4.18, M9 model stalls at α=10° while other models delay stall angle and red tiny portion on the suction surface of M7 and M8 shows transition process. Low turbulence kinetic energy contours enlarge for M0 because of the stall regime.

In the comparison of the size of riblet region in Group III, changing riblet region location adversely affect performance as seen from the figures. Installed riblets in the region 0.3<x/c<0.7, M7 model shows better performance in the coefficients, streamline and stream-wise velocity field, when compared to other models. In the next group, height of the riblet will be discussed.

4.4. Group IV – Riblet Height

In Group IV includes M0, M7, M10 and M11. Different riblet heights which are h/c=0.025, 0.05 and 0.1 are examined for different angles of attack range. Effects of riblet height on lift coefficient, lift-to-drag ratio, pressure coefficient, streamline topology and stream-wise velocity contour are discussed for Group 4.

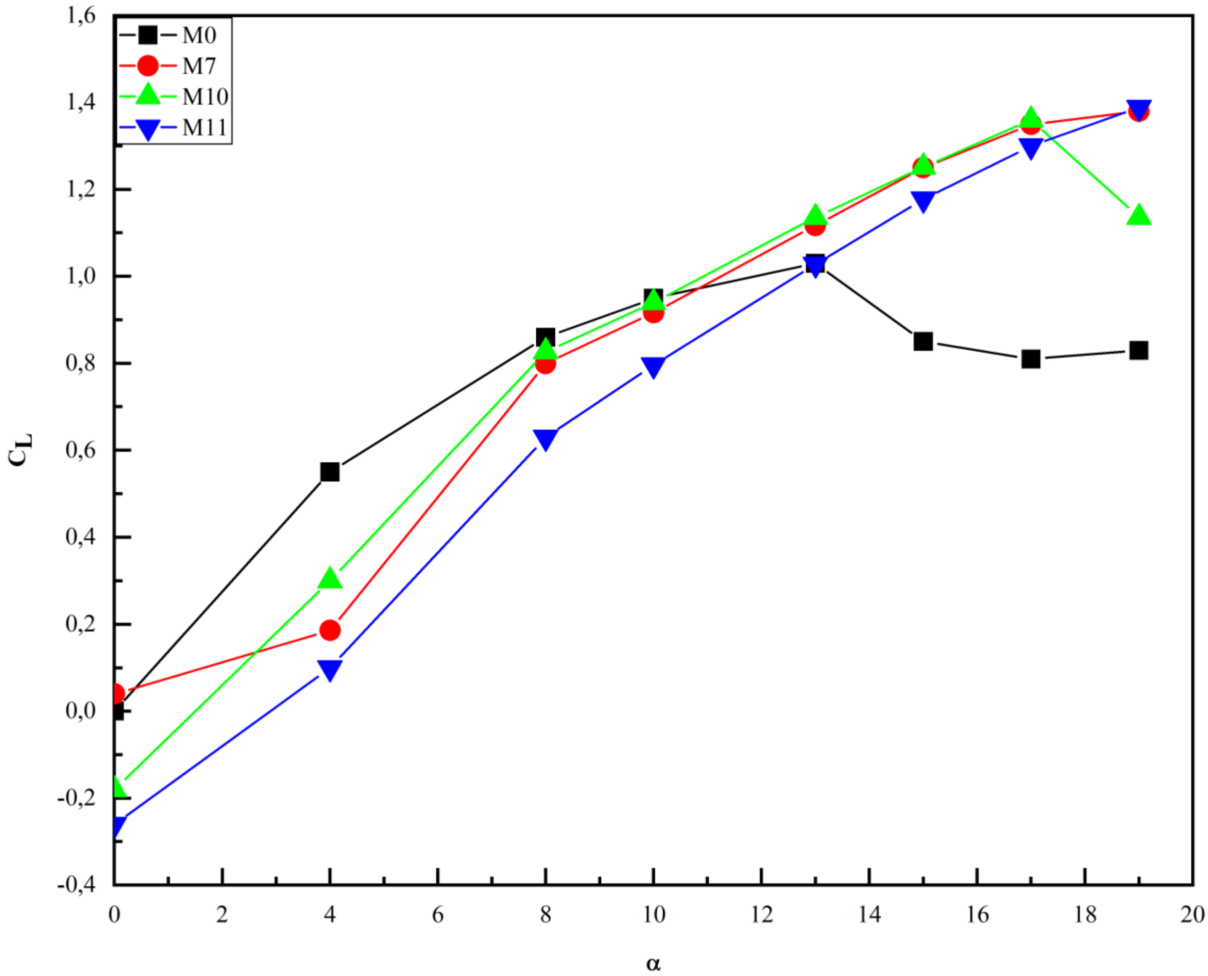

Figure 4.24. Variation of Lift Coefficient of Group IV with the Angles of Attack

In Figure 4.24, the variation of lift coefficients with angle of attack is presented for M0, M7, M10 and M11 models. For α<13, the value of lift coefficient of riblet model is lower than M0 models. Increase or decrease in riblet height to h/c=0.01 or 0.0025 exhibits a negative effect due to the pressure difference over upper and lower surfaces at α=0° compared to M7. The lift coefficient of M11 is decreased about by 80% at α=4°in the comparison with M0. All models show increase in lift coefficient up to high angles of attack, the M7 and M10 models show same trend for lift coefficient slope. It is clearly seen that M7, M10 and M11 models delay stall angle to 19°, 17° and 19°, respectively.

In Figure 4.25, the lift-to-drag ratio for Group IV are showed at α= 0°, 4°, 8°, 10°, 13°, 15°, 17° and 19° for M0, M7, M10 and M11 models. Since M10 and M11, models have negative lift coefficient at α=0°, negative values is obtained for the lift-to-drag ratio. While an increase in the lift-to-drag ratio is observed up to α=8° for all models, then a decrease is observed. The M11 model delays stall up to α=19°, but it creates more drag force than other models due to its high riblet height, and shows poor performance in the lift-to-drag ratio. The M10 model has nearly same value of lift-to-drag ratio with the M0 model at α=8°, and lift-to-drag ratio of M10 model is 5% lower than M0 model. The highest increase in lift-to-drag ratio is observed on M10 model by 290% compared to M0 model at α=15°.

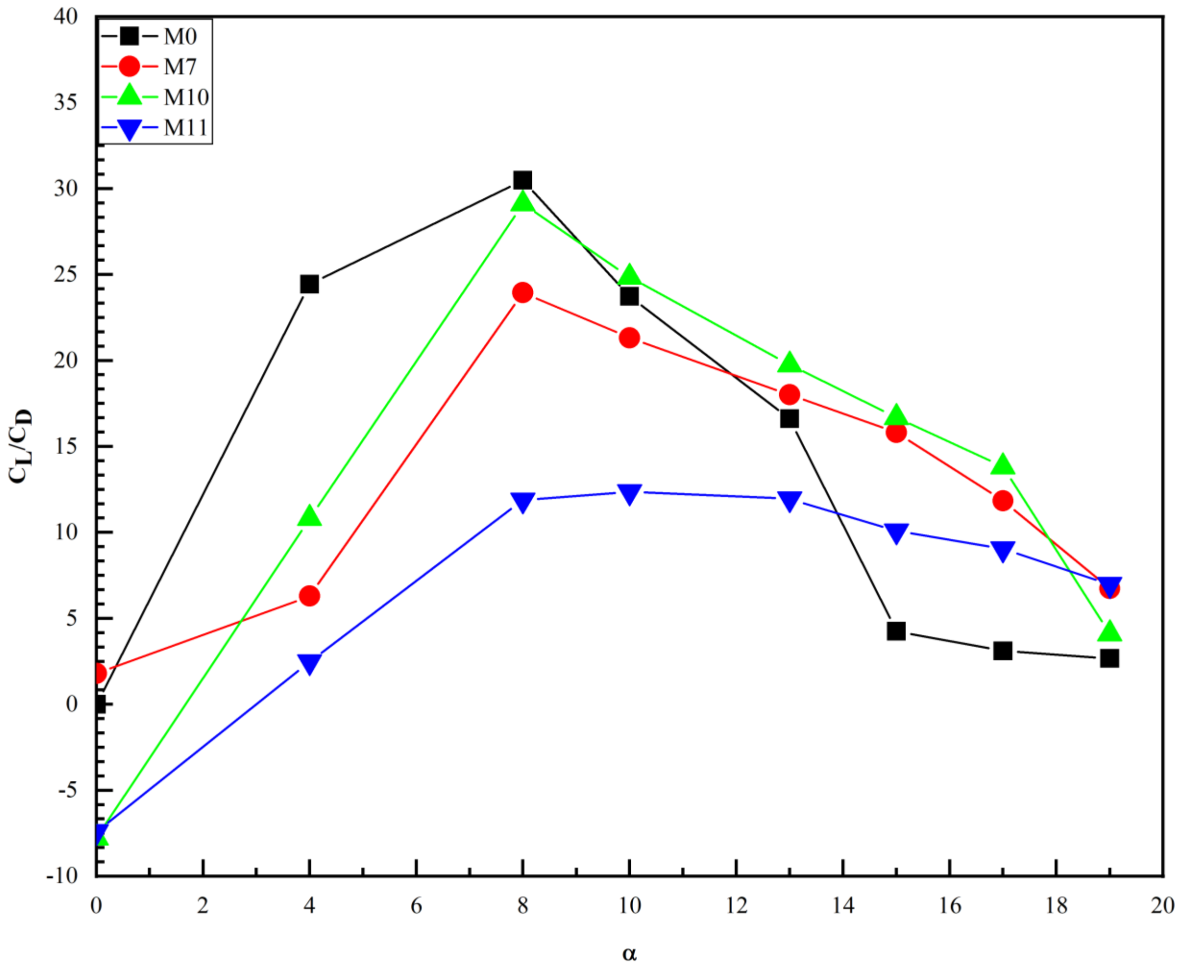

Figure 4.25. Variation of Lift-to-Drag Ratio of Group IV with the Angles of Attack

Streamline topology of Group IV is given in the Figure 4.26 for M10 and M11models at α=4°, 13°, 17° and 19°. At α=4°, height of the riblet causes early separation and late reattachment as seen from the figure and it creates a large bubble on the trailing edge of M11 model. At α=4°, M10 and M11 models prevent LSB formation and only have TES. At α=13°, M10 and M11 models suppress the laminar separation bubble while merging of LSB and TES is observed for M0. Furthermore, M10 model has smaller bubble size due to the lower riblet size and separation occurs latterly when compared to M7 and M11 model. At α=17°, all models have excellent control performance in the comparison of M0 model. A large recirculation region is suppressed. M11 model has larger LSB and M10 has smaller LSB due to the late and early reattachment. At α=19°, the M10 stalls due to merging of LSB and TES while it is not observed for M7 and M11. However, size of LSB is increased for M7 and M11 models while bubble on the trailing edge is approximately stayed same. That figure shows that the M11model, which has highest riblet height, prevents merging of LSB and TES.

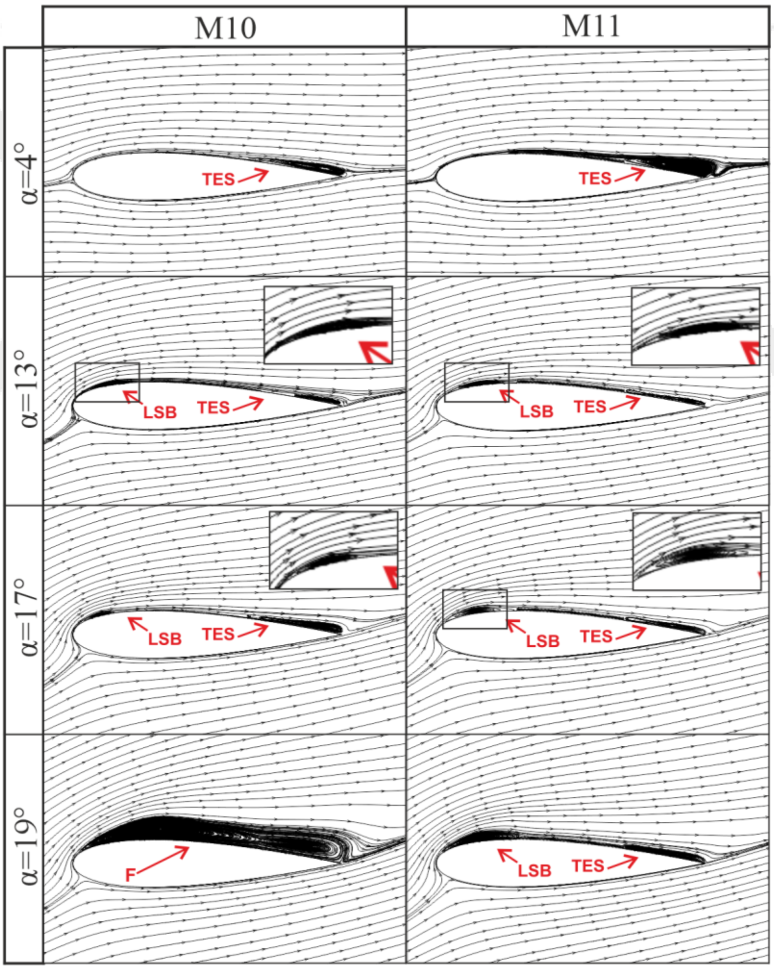

Figure 4.26. Streamline Topology of Group IV at Various Angles of Attack

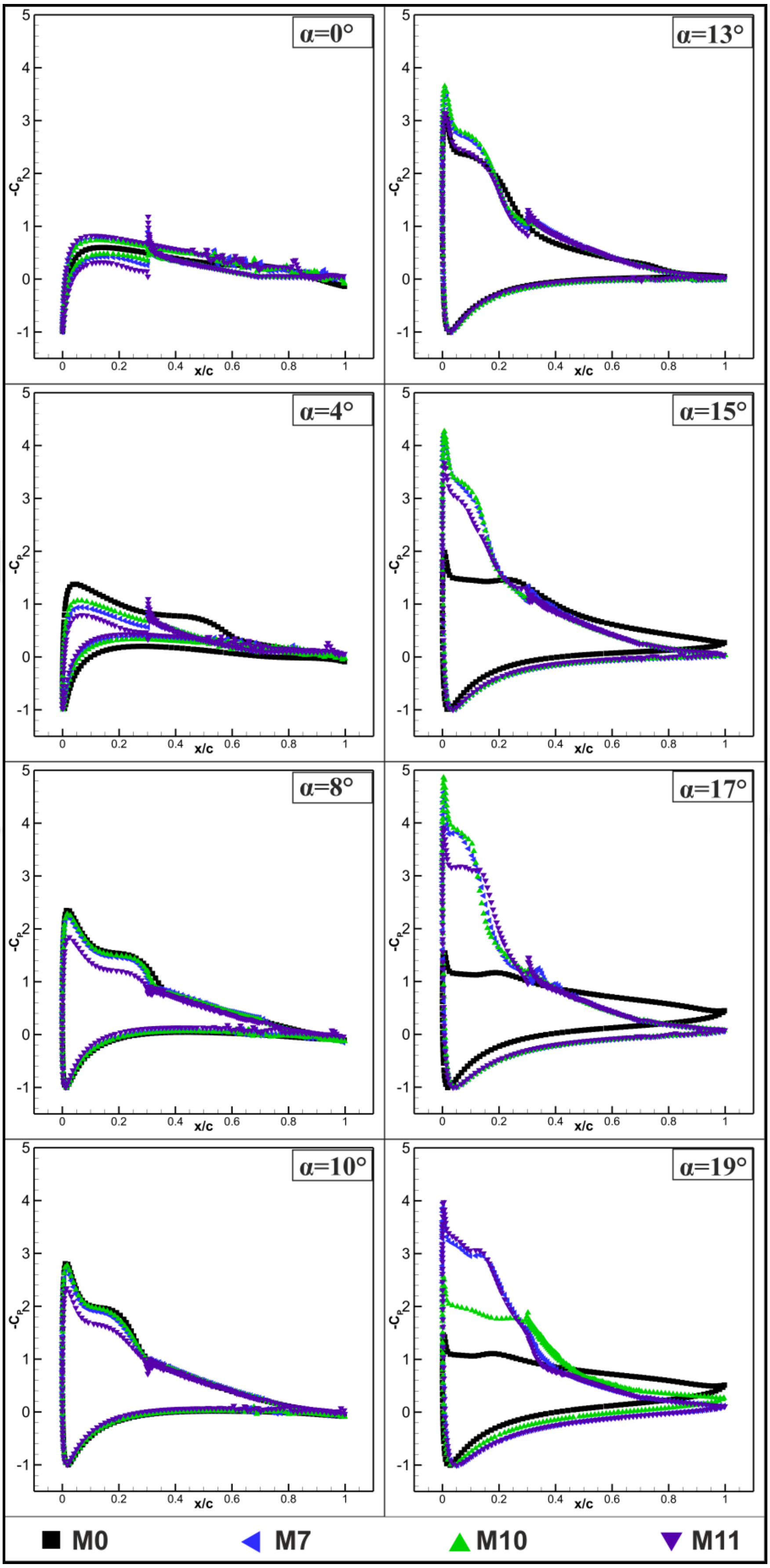

Figure 4.27. Pressure Coefficient of Group IV at Various Angles of Attack

Pressure distribution of M0, M7, M10 and M11 in the angles of attack $0° \leq \alpha \leq 19°$ is given in the Figure 4.27. As it is mentioned before, increase in height of the riblet enhances drag force. Because of that, at low angles of attack, the maximum value of $-C_p$ for M11 model is lower than M7 and M10 models. The M0, M7 and M8 models have nearly same transition point at $\alpha=8°$ and same reattachment point at $\alpha=10°$. At $\alpha=13°$, M7 and M8 have early transition and reattachment than M0 model. The maximum decrease in the laminar separation bubble length is thereabout 32,5% in the comparison of M0 and M10 model at $\alpha=13°$. Until the angle of attack $\alpha=17°$, M11 has lower $-C_P$ performance than M7 and M10 model. The M7 and M10 show nearly same trend on separation, transition and reattachment points up to $\alpha \leq 17°$. At $\alpha=19°$, performance of M10 drops due to stall the pressure coefficient increases for other models.

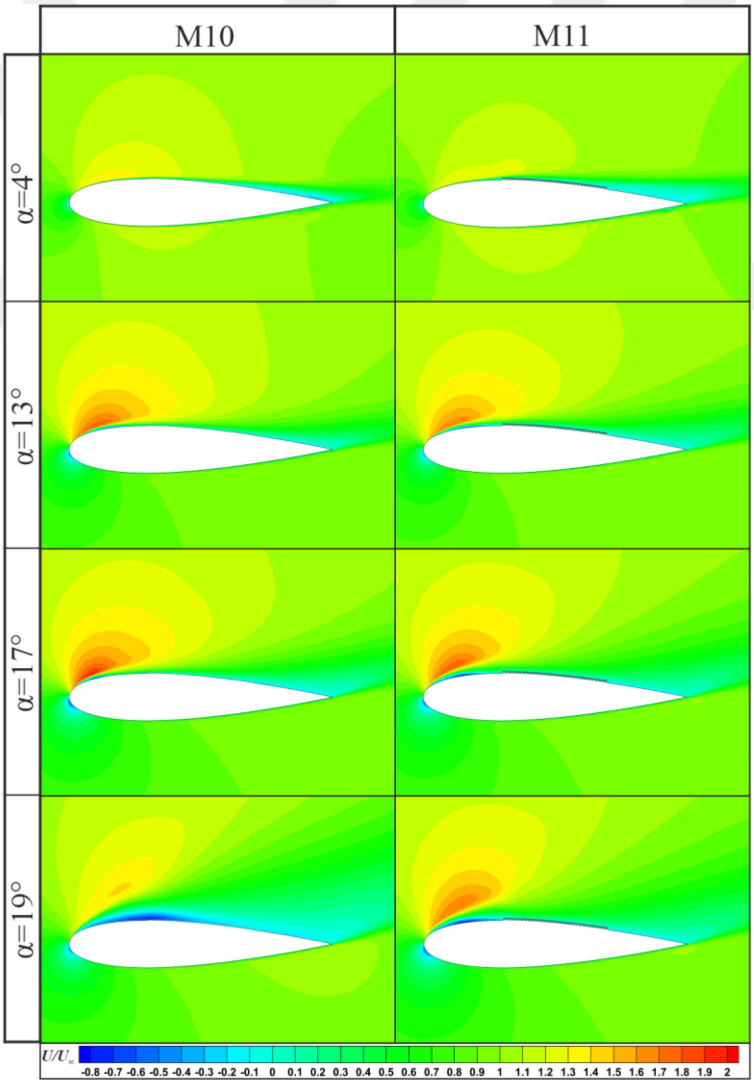

Figure 4.28. Stream-Wise Velocity Contours of Group IV with the Angles of Attack

Stream-wise velocity contours are given in the Figure 4.28 to show velocity field over airfoil for M10 and M11 at α=4°, 13°, 17° and 19°. At α=4° and 13°, low stream-wise velocity is seen on the upper surface of the M10 and M11 models. With the increasing of angle of attack, the height of the riblet is effective on control velocity deceleration as seen at α=19°, M10 model has dark blue region which is re-circulation region while M7 and M11 control that region by higher riblet size by accelerating velocity field.

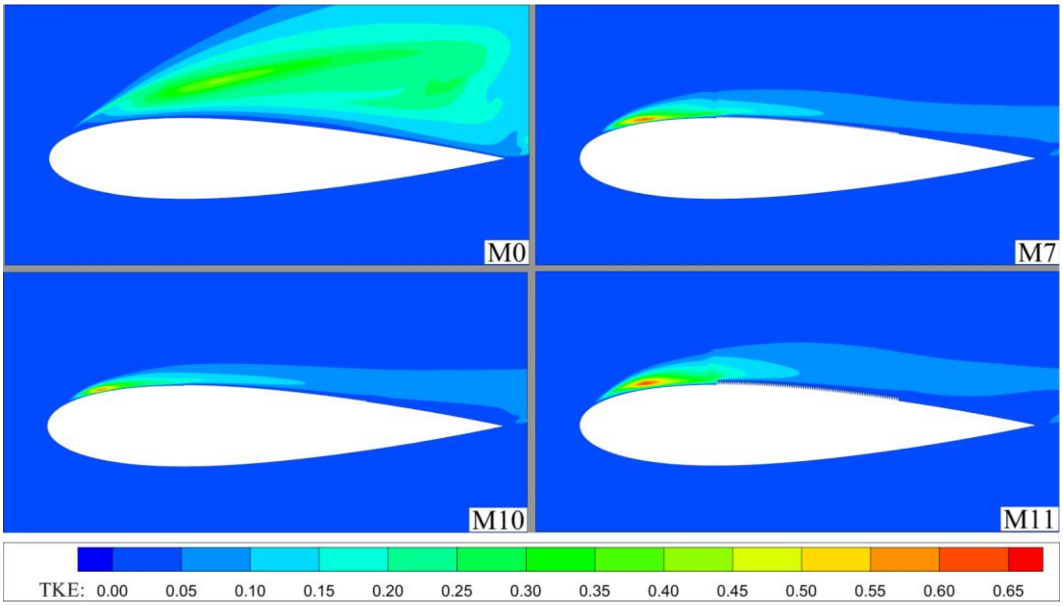

Figure 4.29. Turbulence Kinetic Energy of Group IV at α=17°

Figure 4.29 presents comparison of turbulence kinetic energy for M0, M7, M10 and M11 at α=17°. With the increase in height of riblet causes increase in turbulence kinetic energy. Beginning of the increase is nearly at the same location for M7 and M10 models at α=17° while M11 model causes increase in turbulence kinetic energy.

In conclusion, different riblet heights in Group IV, shows well performance on the control of LSB and TES combination, on delaying stall and increase in lift coefficient. The lower riblet height on M10, delays stall when compared to M0 model but it has lower stall angle than M7 and M11. The M11 model with high riblet size has insignificant effect on the lift-to-drag ratio due to increasing of drag force.

4.5. Group V – Shape of Riblet

In Group V, shape of riblet is discussed. In the previous groups, triangle shape riblets are used to control of flow. To show effect of riblet shape, rectangle riblet cases which are M12, M13 and M14 models with different riblet heights is investigated in order to show how riblet shape changes the performance.

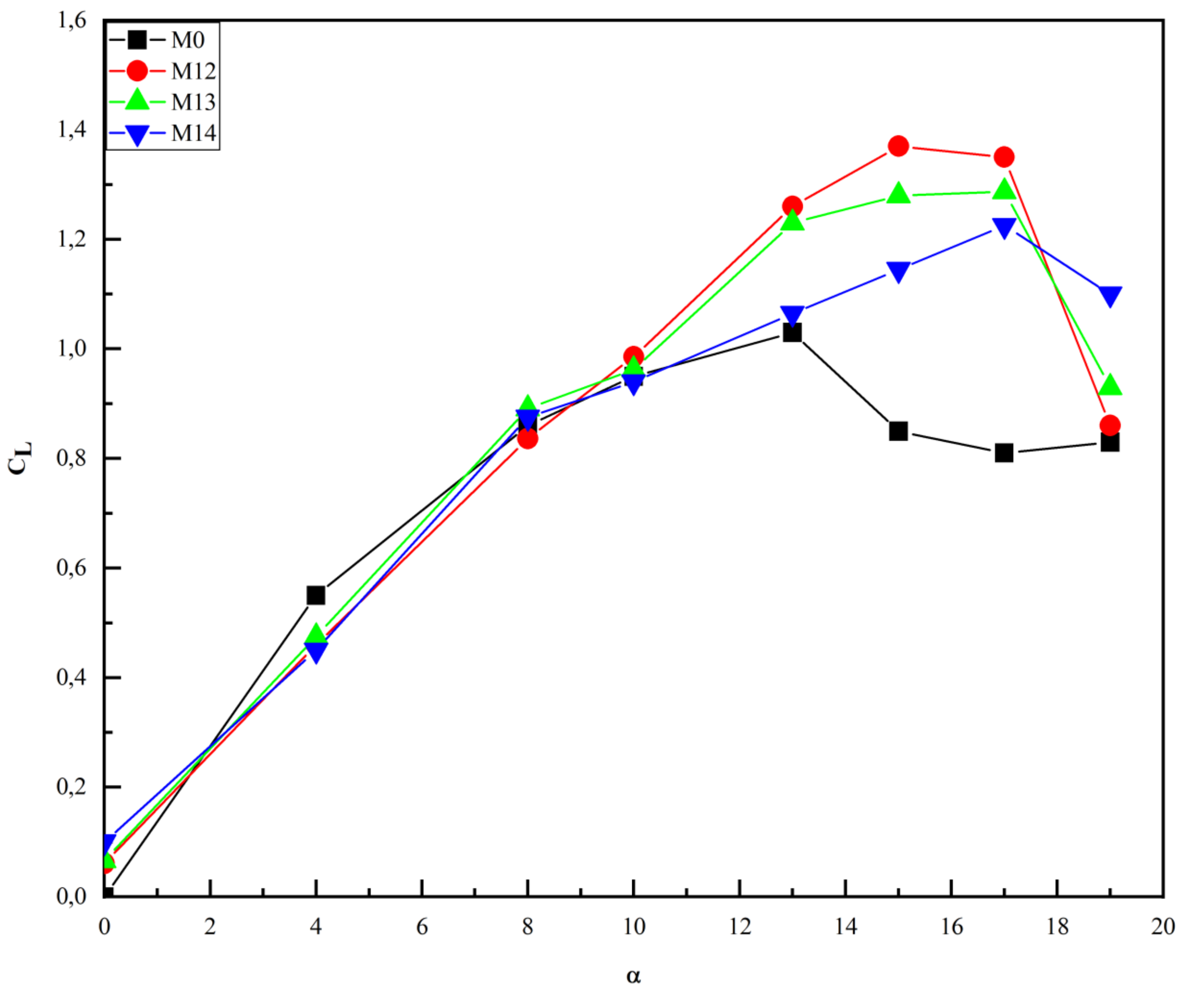

Figure 4.30. Variation of Lift Coefficient of Group V with the Angles of Attack

Lift coefficient of Group V is given in Figure 4.30 for M0, M12, M13 and M14 at the angle of attack of α=0°, 4°, 8°, 10°, 13°, 15°, 17° and 19°. At α=0°, M0 model has zero lift coefficient due to symmetrical shape of airfoil but M12, M13 and M14 models have higher lift value than M0 model. Installing rectangular riblet over airfoil leads to positive lift even at α=0°. At α=4°, the lift coefficients of rectangular riblets are lower than M0 model. The values of lift coefficient for M12, M13 and M14 models are approximately 16% lower than M0 model at α=4°. At α=8° and 10°, all models have nearly same lift coefficients. At α=13°, the highest increase in the lift coefficient is obtained on M12 increase by 33% when compared to M0 model. The increase in lift coefficient for rectangular riblet models continue until stall angle of α=17°. However, M12 stalls gradually while M13 and M14 models shows a sudden stall.

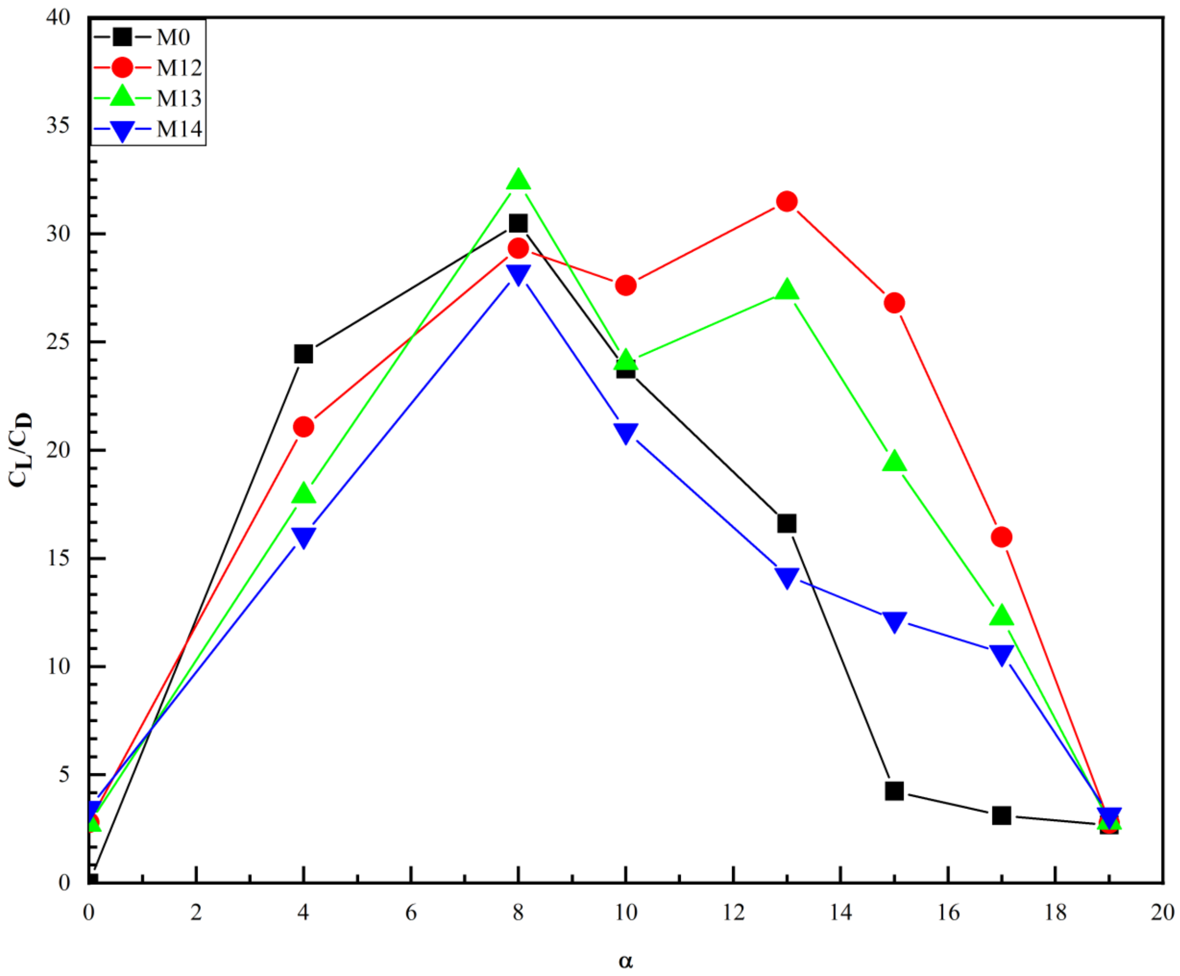

Figure 4.31. Variation of Lift-to-Drag Ratio of Group V with the Angles of Attack

Lift-to-drag ratio of Group V is depicted in Figure 4.31 for M0, M12, M13 and M14 at the angle of attack of α=0°, 4°, 8°, 10°, 13°, 15°, 17° and 19°. At low angles of attack, the effect of drag is higher and causes low lift-to-drag ratio. At α=8°, M13 model has the highest lift-to-drag ratio which is approximately 7% more than M0 model. The lift-to-drag ratios are 16.6, 31.5, 27.3 and 14.2 for M0, M12, M13 and M14, respectively. The best enhancement on lift-to-drag ratio is achieved as 90% at α=13° for M12 in comparison with M0.

Streamline topology of Group V is given in Figure 4.32 for M12, M13 and M14 models at the angles of attack of α=10°, 13°, 15° and 17°. At α=10°, due to the height of the rectangular riblet of M14 model, a small recirculation region occur on the end of riblet geometry while other two model has small TES close to the end of trailing edge and it is clearly seen with the increase in angle of attack to α=13°. The M14 model has a larger TES size than the M12 and M13 model while M0 smooth airfoil model leads to merge of LSB and TES. M14 model prevents the merging of LSB and TES at α=13°. The M12 model suppresses and keeps the LSB and TES size. However, TES enlarge and LSB move forward through leading edge due to the increase in angle of attack for the M13 and M14 model at α=13° and 15°. At α=15°, M12 model has the smallest size of TES and LSB when compared to M13 and M14 models due to change in height of riblet.

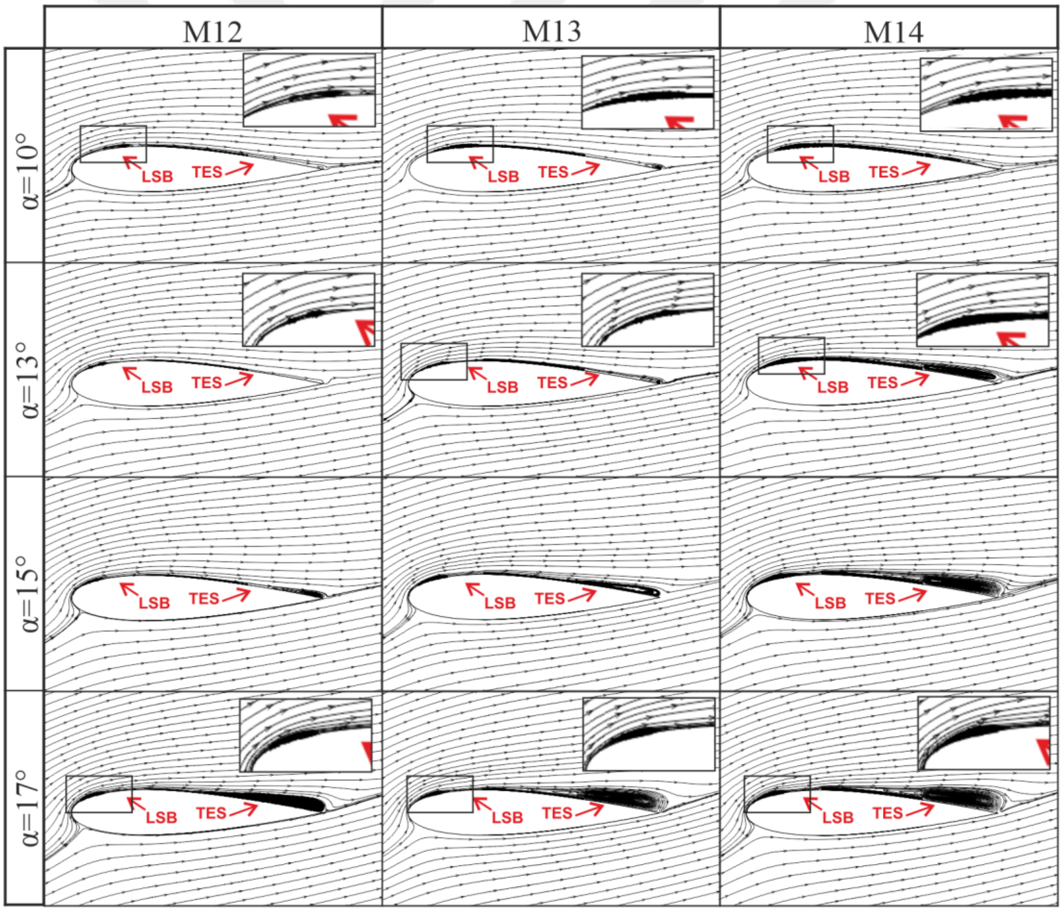

Figure 4.32. Streamline Topology of Group V at Various Angles of Attack

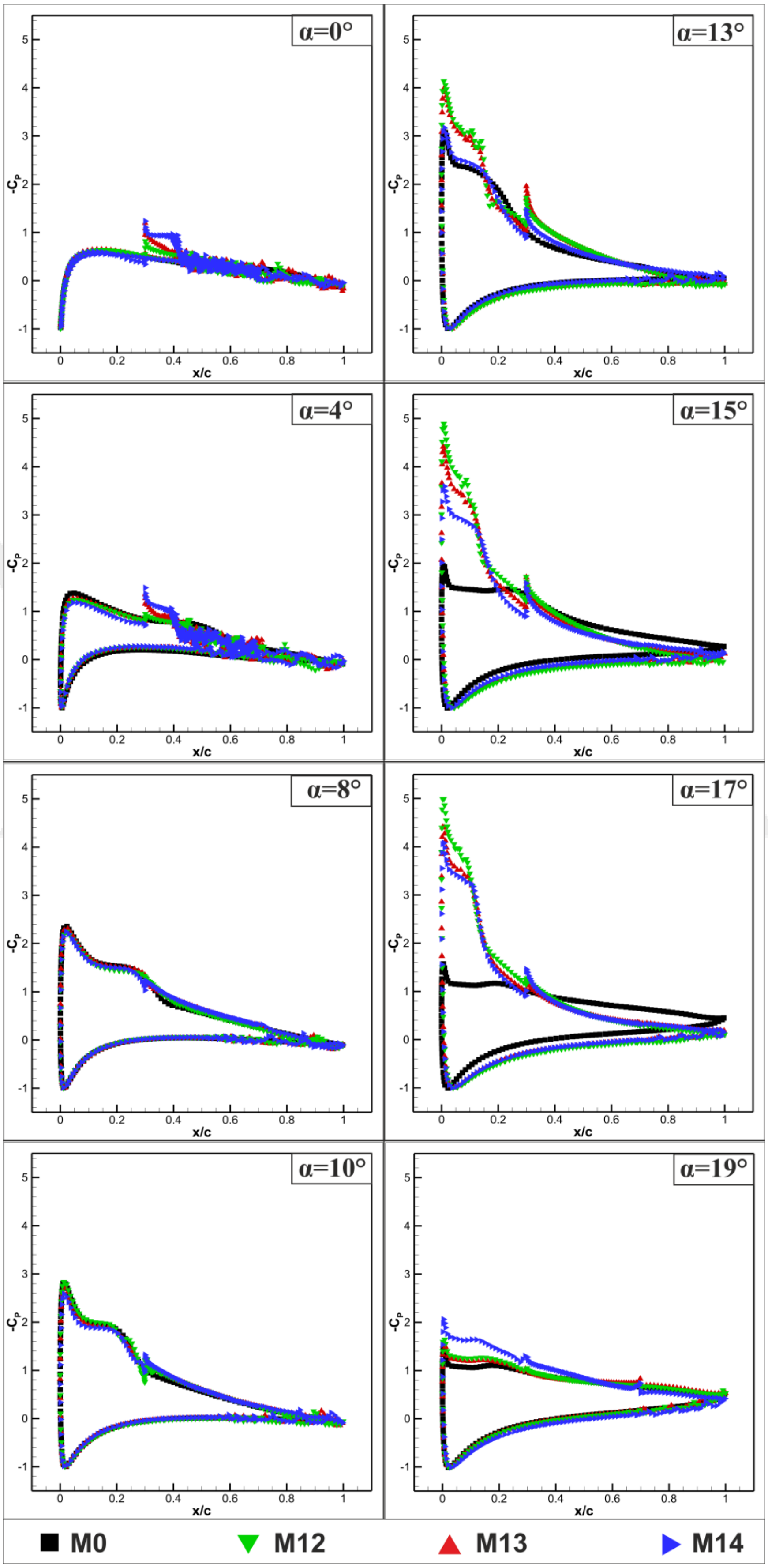

Figure 4.33. Pressure Coefficient of Group V at Various Angles of Attack

Figure 4.33 presents pressure distribution at 0°≤α≤19° for M0, M12, M13 and M14 models. At stall angle of smooth model M0, α=13°, separation point is delayed for M12 and M13 models. This situation causes early transition and reattachment when compared to M14 model because of the increase in riblet height. For α>13°, the size of LSB is smaller than the low angle of attack values. The maximum decrease in the laminar separation bubble length is roundly 48-50% for the M12 and M13 models in comparison with M0 model at α=13°.

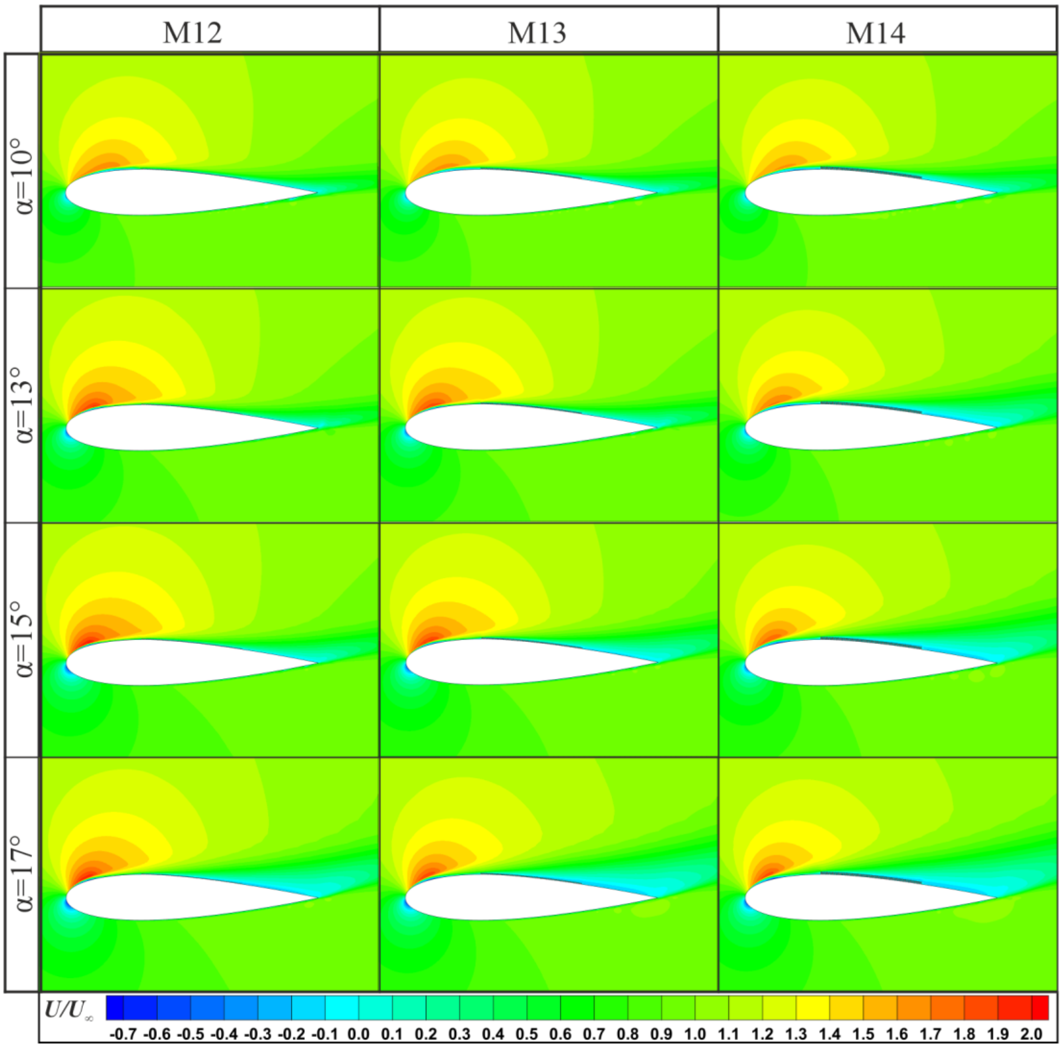

Figure 4.34. Stream-Wise Velocity Contours of Group V with the Angles of Attack

Figure 4.34 depicts stream-wise velocity contours for M12, M13 and M14 models at angles of attack of α=10°, 13°, 15° and 17°. At α=10°, low velocity field on the upper surface is slightly change with the increase in rectangular riblet height. Increase in angle of attack to α=13° causes a concentration of low velocity field for the M14 model. At α=15° and α=17°, it is clearly seen that recirculation region is suppressed for M12 model.

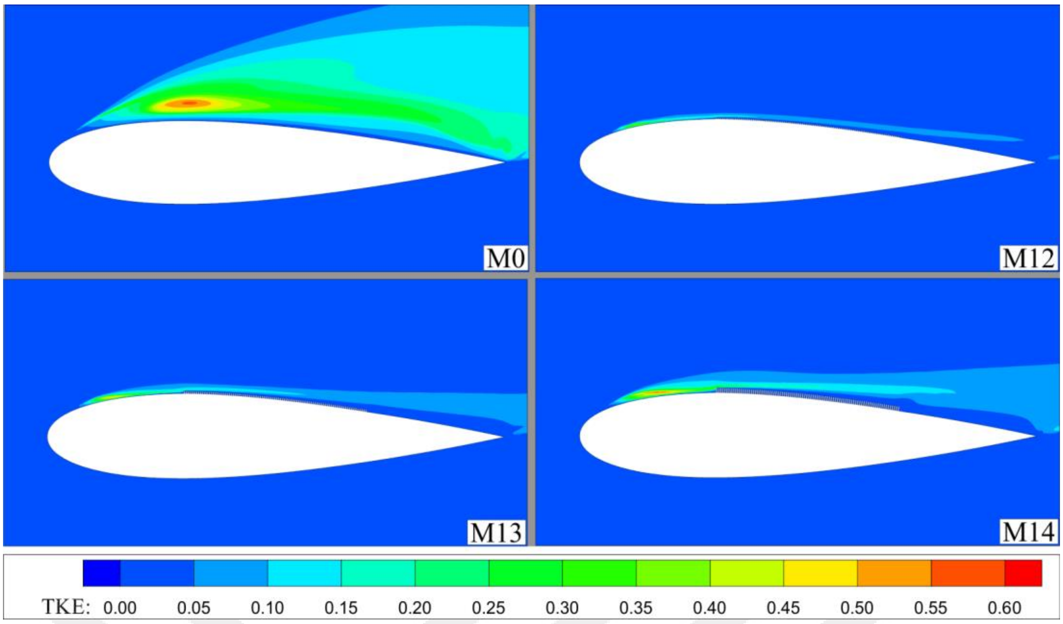

Figure 4.35. Turbulence Kinetic Energy of Group V at α=15°

Figure 4.35 presents comparison of turbulence kinetic energy for M0, M12, M13 and M14 at α=15°. With the increase in height of rectangular riblet causes increase in turbulence kinetic energy. Beginning of the increase is nearly at the same location for M12 and M13 models at α=15° while M14 model causes increase in turbulence kinetic energy.

In conclusion, different riblet heights with rectangular shape riblet in Group V, shows good performance on control of LSB and TES combination, delays stall angle and increase in lift performance. The rectangular shape riblets with low riblet height show good performance on lift-to-drag ratio with compared to triangle riblets. However, they are insufficient for stall control. Lastly, Group V is good on controlling LSB and TES sizes.

5. CONCLUSIONS

Determining of the riblet location has a great importance for the control of the laminar separation bubble. First, single and double riblets placed on the suction surface of the airfoil in order to determine borders of riblet region. The maximum decrease in the laminar separation bubble length is approximately 29% and stall delayed to α=15° for M3 model. Thanks to the location parameter examined in Group I, the double riblet placed at x/c=0.3 and x/c=0.7 helped in determining goals such as LSB control and stall delay. In Group II, the gap ratio of riblet was examined by increasing the number of riblet in the related region. Decrease in the gap ratio causes diminish in the LSB size by 30% and the stall angle is delayed to α=19°. For the determined gap ratio of riblet, the size of riblet region was changed locally in Group III, and it was observed that this change adversely affect aerodynamics performance of airfoil. Increase in the size of riblet region leads to early stall. In the next group, Group IV, the effect of riblet height was investigated. It is observed that riblet surfaces with small riblet height (M10 model) increases C_L/C_D ratio. The maximum decrease in the laminar separation bubble length is thereabout 32,5% for M10 model in comparison with M0 at α=13°.Higher riblet length delays stall angle, however, it increases the drag coefficient. At Group V, low height (h/c=0.0025 and 0.05) rectangular riblets are effective on the control of LSB and TES. The maximum decrease in the laminar separation bubble length is roundly 48-50% for the M12 and M13 models in comparison with M0 model at α=13°. Also stall angle is delayed for rectangular riblet. It is concluded that the triangular riblets is more effective than rectangular riblet. The optimum case is determined as M7 model in order to control LSB and lift performance.

RECOMMENDATIONS

In the light of the aforementioned results, following suggestion is listed for future studies:

- The effect of riblets on vortex induced vibration should be investigated.
- Riblet surface should be examined for different parameters such as airfoil profiles, Reynolds numbers and riblet shapes.
- Three dimensional unsteady numerical analysis should be performed to reveal the mechanism of flow control.

REFERENCES

Abdollahzadeh, M., Pascoa, J. C., & Oliveira, P. J. (2018). Comparison of DBD plasma actuators flow control authority in different modes of actuation. *Aerospace Science and Technology*, *78*, 183-196.

Açıkel, H. H., & Genc, M. S. (2018). Control of laminar separation bubble over wind turbine airfoil using partial flexibility on suction surface. *Energy*, *165*, 176-190.

Aftab, S. M. A., Mohd Rafie, A. S., Razak, N. A., & Ahmad, K. A. (2016). Turbulence model selection for low Reynolds number flows. *PloS one*, *11*(4), e0153755.

Airplane Aerodynamics, 2021. http://www.free-online-private-pilot-ground-school.com/aerodynamics.html

Akbıyık, H., Yavuz, H., & Akansu, Y. E. (2017). Comparison of the linear and spanwise-segmented DBD plasma actuators on flow control around a NACA0015 airfoil. *IEEE Transactions on Plasma Science*, *45*(11), 2913-2921.

Amitay, M., Smith, D. R., Kibens, V., Parekh, D. E., & Glezer, A. (2001). Aerodynamic flow control over an unconventional airfoil using synthetic jet actuators. *AIAA journal*, *39*(3), 361-370.

Andan, A. D., & Lee, D. J. (2018). Effect of external acoustic excitation on NACA0015 discrete tonal noise. *Applied Acoustics*, *141*, 374-381.

Attar, P. J., Morris, B. J., Romberg, W. A., Johnston, J. W., & Parthasarathy, R. N. (2012). Experimental characterization of aerodynamic behavior of membrane wings in low-Reynolds-number flow. *AIAA journal*, *50*(7), 1525-1537.

Bangalore, A., & Sankar, L. N. (1996). Numerical analysis of aerodynamic performance of rotors with leading edge slats. *Computational mechanics*, *17*(5), 335-342.

Bangalore, A., & Sankar, L. N. (1997). Forward-flight analysis of slatted rotors using Navier-Stokes methods. *Journal of aircraft*, *34*(1), 80-86.

Baragona, M., Boermans, L. M. M., van Tooren, M. J. L., Bijl, H., & Beukers, A. (2003). Bubble bursting and stall hysteresis on single-slotted flap high-lift configuration. *AIAA journal*, *41*(7), 1230-1237.

Barata, J. M., Neves, F. M. S. P., & Manquinho, P. A. (2015, January). Comparative study of wing's motion patterns on various types of insects on resemblant flight stages. In *Proceedings of the AIAA Atmospheric Flight Mechanics Conference, SciTech* (pp. 828-848).

Belamadi, R., Djemili, A., Ilinca, A., & Mdouki, R. (2016). Aerodynamic performance analysis of slotted airfoils for application to wind turbine blades. *Journal of wind engineering and industrial aerodynamics*, *151*, 79-99.

Biedermann, T. M., Chong, T. P., Kameier, F., & Paschereit, C. O. (2017). Statistical–empirical modeling of airfoil noise subjected to leading-edge serrations. *AIAA Journal*, *55(9)*, 3128-3142.

Bohnker, J. R., & Breuer, K. S. (2019). Control of separated flow using actuated compliant membrane wings. *AIAA Journal, 57(9)*, 3801-3811.

Bragg, M. B., & Gregorek, G. M. (1987). Experimental study of airfoil performance with vortex generators. *Journal of aircraft*, *24*(5), 305-309.

Cleaver, D. J., Gursul, I., Calderon, D. E., & Wang, Z. (2014). Thrust enhancement due to flexible trailing-edge of plunging foils. *Journal of Fluids and Structures*, *51*, 401-412.

Combes, T. P., Malik, A. S., Bramesfeld, G., & McQuilling, M. W. (2015). Efficient fluid-structure interaction method for conceptual design of flexible, fixed-wing micro-air-vehicle wings. *AIAA Journal*, *53*(6), 1442-1454.

Daniel, L., & Traub, L. W. (2013). Effect of aspect ratio on gurney-flap performance. *Journal of aircraft, 50*(4), 1217-1225.

Demir, H., & Genç, M. S. (2017). An experimental investigation of laminar separation bubble formation on flexible membrane wing. *European Journal of Mechanics-B/Fluids, 65*, 326-338.

Fatehi, M., Nili-Ahmadabadi, M., Nematollahi, O., Minaiean, A., & Kim, K. C. (2019). Aerodynamic performance improvement of wind turbine blade by cavity shape optimization. *Renewable Energy, 132*, 773-785.

Fluent, A.N.S.Y.S. (2013). ANSYS fluent theory guide 15.0. ANSYS, *Canonsbur*g, *PA, 33*.

Gaster, M. (1967). *The structure and behaviour of laminar separation bubbles*. NPL.

Genç, M. S., Özden, M., Açikel, H. H., Demir, H., & Isabekov, I. (2016). Unsteady flow over flexible wings at different low Reynolds numbers. In EPJ *Web of Conferences* (Vol. 114, p. 02030). EDP Sciences.

Gopalarathnam, A., Broughton, B. A., McGranahan, B. D., & Selig, M. S. (2003). Design of low Reynolds number airfoils with trips. *Journal of aircraft, 40*(4), 768-775.

Haolin, Z. H. I., Zhenhao, Z. H. U., Yujin, L. U., Shuanghou, D. E. N. G., & Tianhang, X. I. A. O. (2021). Aerodynamic performance enhancement of co-flow jet airfoil with simple high-lift device. *Chinese Journal of Aeronautics.*

He, C., Corke, T. C., & Patel, M. P. (2009). Plasma flaps and slats: an application of weakly ionized plasma actuators. *Journal of aircraft, 46*(3), 864-873.

Huber, A. F., & Mueller, T. J. (1987). The effect of trip wire roughness on the performance of the Wortmann FX 63-137 airfoil at low Reynolds numbers. *Experiments in fluids, 5*(4), 263-272.

Istvan, M. S., Kurelek, J. W., & Yarusevych, S. (2018). Turbulence intensity effects on laminar separation bubbles formed over an airfoil. *AIAA Journal*, *56*(4), 1335-1347.
ITO, S. (2009). Aerodynamic influence of leading-edge serrations on an airfoil in a low Reynolds number-A study of an owl wing with leading edge serrations. *Journal of Biomechanical Science and Engineering*, *4*(1), 117-123.

Jahanmiri, M. (2010). Active flow control: a review.

James, S. E., Suryan, A., Sebastian, J. J., Mohan, A., & Kim, H. D. (2018). Comparative study of boundary layer control around an ordinary airfoil and a high lift airfoil with secondary blowing. *Computers & Fluids, 164*, 50-63

Jang, C. S., Ross, J. C., & Cummings, R. M. (1998). Numerical investigation of an airfoil with a Gurney flap. *Aircraft Design*, *1*(2), 75-88.

Jolibois, J., Forte, M., & Moreau, É. (2008). Application of an AC barrier discharge actuator to control airflow separation above a NACA 0015 airfoil: Optimization of the actuation location along the chord. *Journal of Electrostatics, 66*(9-10), 496-503.

Junxuan, C., & Xun, G. Z. (2015). Numerical study on drag reduction by micro-blowing/suction compounding flow control on supercritical airfoil. *Procedia Engineering*, *99*, 613-617.

Kamari, D., Tadjfar, M., & Madadi, A. (2018). Optimization of SD7003 airfoil performance using TBL and CBL at low Reynolds numbers. *Aerospace Science and Technology*, *79*, 199-211.
Karasu, I., Genç, M. S., & Açikel, H. H. (2013). Numerical study on low Reynolds number flows over an Aerofoil. *J. Appl. Mech. Eng*, *2*(5), 1000131.

Katz, J., Plotkin, A., 1991, *Low-Speed Aerodynamics from Wing Theory to Panel Methods,* McGraw-Hill*, Inc*, 632 pp.

Kerho, M., Hutcherson, S., Blackwelder, R. F., & Liebeck, R. H. (1993). Vortex generators used to control laminar separation bubbles. *Journal of aircraft*, *30*(3), 315-319.

Kral, L. D. (2000). Active flow control technology. *ASME Fluids Engineering Technical Brief*.

Lam, G. C., & Leung, R. C. (2018). Aeroacoustics of NACA 0018 Airfoil with a Cavity. *AIAA Journal*, *56*(12), 4775-4786.

Lee, S. J., & Jang, Y. G. (2005). Control of flow around a NACA 0012 airfoil with a micro-riblet film. *Journal of Fluids and Structures*, *20*(5), 659-672.

Lee, S. J., Lim, H. C., Han, M., & Lee, S. S. (2005). Flow control of circular cylinder with a V-grooved micro-riblet film. *Fluid dynamics research*, *37*(4), 246.

Li, Y. C., Wang, J. J., & Hua, J. (2007). Experimental investigations on the effects of divergent trailing edge and Gurney flaps on a supercritical airfoil. *Aerospace Science and Technology*, *11*(2-3), 91-99.

Li, Y., Wang, X. N., Chen, Z. W., & Li, Z. C. (2014). Experimental study of vortex–structure interaction noise radiated from rod–airfoil configurations. *Journal of Fluids and Structures*, *51*, 313-325.

Lian, Y., & Shyy, W. (2007). Laminar-turbulent transition of a low Reynolds number rigid or flexible airfoil. *AIAA journal*, *45*(7), 1501-1513.
Lift Theory, 2021. https://en.wikipedia.org/wiki/Lift_ (force)

Lin, J. C., Robinson, S. K., McGhee, R. J., & Valarezo, W. O. (1994). Separation control on high-lift airfoils via micro-vortex generators. *Journal of aircraft*, *31*(6), 1317-1323.

Luo, D., Huang, D., & Sun, X. (2017). Passive flow control of a stalled airfoil using a microcylinder. *Journal of Wind Engineering and Industrial Aerodynamics*, *170*, 256-273.

Manolesos, M., & Voutsinas, S. G. (2016). Experimental study of drag-reduction devices on a flatback airfoil. *AIAA Journal*, *54*(11), 3382-3396.

Meena, M., Taira, K., & Asai, K. (2017). Airfoil-wake modification with gurney flap at low reynolds number. *AIAA journal*, *56*(4), 1348-1359.

Metzinger, C. N., Chow, R., Baker, J. P., Cooperman, A. M., & Van Dam, C. P. (2018). Experimental and Computational Investigation of Blunt Trailing-Edge Airfoils with Splitter Plates. *AIAA Journal, 56*(8), 3229-3239.

Mishra, A., & Baeder, J. D. (2016). Coupled aeroelastic prediction of the effects of leading-edge slat on rotor performance. *Journal of Aircraft, 53*(1), 141-157.

Moghaddam, T., & Neishabouri, N. B. (2017, October). On the active and passive flow separation control techniques over airfoils. I*n IOP Conference Series: Materials Science and Engineering* (Vol. 248, No. 1, p. 012009). IOP Publishing.

Mohamed, M. A. R., Guven, U., & Yadav, R. (2019). Flow separation control of NACA-2412 airfoil with bio-inspired nose. *Aircraft Engineering and Aerospace Technology*.

Mohamed, O. S., Ibrahim, A. A., Etman, A. K., Abdelfatah, A. A., & Elbaz, A. M. (2020). Numerical investigation of Darrieus wind turbine with slotted airfoil blades. *Energy Conversion and Management: X*, 5, 100026.

Moreau, E., Debien, A., Breux, J. M., & Benard, N. (2016). Control of a turbulent flow separated at mid-chord along an airfoil with DBD plasma actuators. *Journal of Electrostatics, 83*, 78-87.

Muddada, S., & Patnaik, B. S. V. (2010). An active flow control strategy for the suppression of vortex structures behind a circular cylinder. *European Journal of Mechanics-B/Fluids, 29*(2), 93-104.

Nakagawa, T. (1992). Effects of a small airfoil-shaped splitter plate on vortex shedding from a square prism at subsonic Mach numbers. *Acta mechanica*, *91*(1), 11-25.

Narayanan, S., Chaitanya, P., Haeri, S., Joseph, P., Kim, J. W., & Polacsek, C. (2015). Airfoil noise reductions through leading edge serrations. *Physics of Fluids*, *27*(2), 025109.

Ni, Z., Dhanak, M., & Su, T. C. (2019). Improved performance of a slotted blade using a novel slot design. *Journal of Wind Engineering and Industrial Aerodynamics*, *189*, 34-44.

Olsman, W. F. J., & Colonius, T. (2011). Numerical simulation of flow over an airfoil with a cavity. *AIAA journal*, *49*(1), 143-149.

Ozkan, G. M. (2021). Control of the flow in the near wake of an airfoil at full stall using fixed trailing-edge plates. *Experimental Thermal and Fluid Science*, *122*, 110296.

Rousoulis, L., Lacor, C., & Ghorbaniasl, G. (2017). A flow control technique for noise reduction of a rod-airfoil configuration. *Journal of Fluids and Structures*, *69*, 293-307.

Sareen, A., Deters, R. W., Henry, S. P., & Selig, M. S. (2014). Drag reduction using riblet film applied to airfoils for wind turbines. *Journal of Solar Energy Engineering*, *136*(2).

Schumacher, K. L., Doolan, C. J., & Kelso, R. M. (2014). The effect of a cavity on airfoil tones. *Journal of Sound and Vibration*, *333*(7), 1913-1931.

Separation Bubble, 2021. http://www-mdp.eng.cam.ac.uk /web/library/enginfo/ aerothermal _dvd_only/aero/fprops/introvisc/node9.html

Seshagiri, A., Cooper, E., & Traub, L. W. (2009). Effects of vortex generators on an airfoil at low Reynolds numbers. *Journal of Aircraft*, *46*(1), 116-122.

Singh, M. K., Dhanalakshmi, K., & Chakrabartty, S. K. (2007). Navier-Stokes analysis of airfoils with Gurney flap. *Journal of Aircraft*, *44*(5), 1487-1493.

Smith, R., & Shyy, W. (1995). Computational model of flexible membrane wings in steady laminar flow. *AIAA journal, 33*(10), 1769-1777.

Song, K. (2020, April). Numerical Investigation of Flatback Airfoils Drag and Noise Reduction by a Splitter Plate. In *IOP Conference Series: Earth and Environmental Science* (Vol. 495, No. 1, p. 012081). IOP Publishing.

Storms, B. L., & Jang, C. S. (1994). Lift enhancement of an airfoil using a Gurney flap and vortex generators. *Journal of Aircraft, 31*(3), 542-547.

Taherian, G., Nili-Ahmadabadi, M., Karimi, M. H., & Tavakoli, M. R. (2017). Flow visualization over a thick blunt trailing-edge airfoil with base cavity at low Reynolds numbers using PIV technique. *Journal of visualization, 20*(4), 695-710.

Tani, I. (1964). Low-speed flows involving bubble separations. *Progress in Aerospace Sciences, 5*, 70-103.

Tao, W. U., Bifeng, S. O. N. G., Wenping, S. O. N. G., Wenqing, Y. A. N. G., & Zhonghua, H. A. N. (2020). Aerodynamic performance enhancement for flapping airfoils by co-flow jet. *Chinese Journal of Aeronautics, 33*(10), 2535-2554.

Tiainen, J., Grönman, A., Jaatinen-Värri, A., & Pyy, L. (2020). Effect of non-ideally manufactured riblets on airfoil and wind turbine performance. *Renewable Energy, 155*, 79-89.

Timpe, A., Zhang, Z., Hubner, J., & Ukeiley, L. (2013). Passive flow control by membrane wings for aerodynamic benefit. *Experiments in fluids, 54*(3), 1-23.

Traub, L. W., & Chandrashekar, S. M. (2016). Experimental study on the effects of wing sweep on Gurney flap performance. *Aerospace Science and Technology, 55*, 57-63.

U.S. Centennial of flight commission, 2021. https://www.centennialofflight.net/.

Viieru, D., Tang, J., Lian, Y., Liu, H., & Shyy, W. (2006, January). Flapping and flexible wing aerodynamics of low Reynolds number flight vehicles. *In 44th AIAA Aerospace Sciences Meeting and Exhibit* (p. 503).

Walters, D. K., & Leylek, J. H. (2004). A new model for boundary layer transition using a single-point RANS approach. *J. Turbomach., 126*(1), 193-202.

Wang, J. J., Lan, S. L., & Chen, G. (2000). Experimental study on the turbulent boundary layer flow over riblets surface. *Fluid dynamics research*, *27*(4), 217.

Wang, J., & Feng, L. (2019). *Flow control techniques and applications*. Cambridge University Press.

Wikipedia, 2021. https://en.wikipedia.org/wiki/Airfoil

Winzen, A., Roidl, B., Klän, S., Klaas, M., & Schröder, W. (2014). Particle-image velocimetry and force measurements of leading-edge serrations on owl-based wing models. *Journal of Bionic Engineering*, *11*(3), 423-438.

Wong, K. W. L., Zhao, J., Jacono, D. L., Thompson, M. C., & Sheridan, J. (2017). Experimental investigation of flow-induced vibration of a rotating circular cylinder. *Journal of Fluid Mechanics*, *829*, 486-511.

Wu, Z., Li, S., Liu, M., Wang, S., Yang, H., & Liang, X. (2019). Numerical research on the turbulent drag reduction mechanism of a transverse groove structure on an airfoil blade. *Engineering Applications of Computational Fluid Mechanics*, *13*(1), 1024-1035.

Xu, H., Xing, S., & Ye, Z. (2015). Numerical simulation of the effect of a co-flow jet on the wind turbine airfoil aerodynamic characteristics. *Procedia Engineering*, *126*, 706-710.

Yang, S. L., & Spedding, G. R. (2013). Separation control by external acoustic excitation at low Reynolds numbers. *AIAA journal*, *51*(6), 1506-1515.

Yarusevych, S., Sullivan, P. E., & Kawall, J. G. (2007). Effect of acoustic excitation amplitude on airfoil boundary layer and wake development. *AIAA journal*, *45*(4), 760-771.

Yarusevych, S., Sullivan, P. E., & Kawall, J. G. (2009). On vortex shedding from an airfoil in low-Reynolds-number flows. *Journal of Fluid Mechanics*, *632*, 245-271.

Yee, K., Joo, W., & Lee, D. H. (2007). Aerodynamic performance analysis of a Gurney flap for rotorcraft application. *Journal of Aircraft*, *44*(3), 1003-1014.

Yu, T., Wang, J. J., & Zhang, P. F. (2011). Numerical simulation of Gurney flap on RAE-2822 supercritical airfoil. *Journal of Aircraft*, *48*(5), 1565-1575.

Zha, G. C., Carroll, B. F., Paxton, C. D., Conley, C. A., & Wells, A. (2007). High-performance airfoil using coflow jet flow control. *AIAA journal*, *45*(8), 2087-2090.

Zhang, Y., Chen, H., Fu, S., & Dong, W. (2018). Numerical study of an airfoil with riblets installed based on large eddy simulation. *Aerospace Science and Technology*, *78*, 661-670.